Politecnico di Torino

Master's Degree in Aerospace Engineering

Master Thesis

Topology Optimization of Hybrid Rocket Fuels for Additive Manufacturing

Mirko Melis

Supervisors: Prof. Frederico José Prata Rente Reis Afonso
Prof. Alain de Souza
Prof. Alfonso Pagani
Prof. Alberto Racionero Sanchez-Majano

April 2024

To those who never give up

Declaration

I declare that this document is an original work of my own authorship and that it fulfills all the requirements of the Code of Conduct and Good Practices of the Universidade de Lisboa.

This work was supported by Fundação para a Ciência e a Tecnologia (FCT), through IDMEC, under LAETA, project UIDB/50022/2020.

Acknowledgments

I would like to extend my sincere gratitude to Professors Frederico Afonso and Alain De Souza for their warm welcome and availability, as well as their continuous support and assistance throughout the development of this thesis at the Instituto Superior Técnico in Lisbon.

I would also like to express my gratitude to Professors Afzal Suleman and Fernando Lau from IST for the opportunities provided, their steadfast guidance, and valuable suggestions.

Additionally, I would like to thank Professors Alfonso Pagani and Alberto Racionero Sanchez-Majano for contribution on behalf of Politecnico di Torino.

Desidero esprimere la mia sincera gratitudine a Sara e Alessandra. Con voi, ho condiviso intensamente questa straordinaria esperienza a Lisbona e all'Istituto Superior Tecnico; il vostro sostegno è stato fondamentale per me. Sono stato fortunato ad avere entrambe al mio fianco. Ringrazio inoltre tutte le altre persone e amici che ho incontrato e con cui ho condiviso momenti significativi durante l'intero anno a Lisbona. Questo periodo è stato uno dei più cruciali della mia vita, e ogni istante e ricordo rimarranno tesori preziosi.

Desidero dedicare un ringraziamento speciale a Gianluca; specialmente nell'ultimo anno, la nostra amicizia si è trasformata. Le profonde discussioni che abbiamo avuto in luoghi e momenti diversi sono state costantemente fonte di grande ispirazione e stimolo in ogni aspetto della vita. Sono felice del legame che si è creato tra di noi.

Un sentito ringraziamento va a Sebastiano, Andrea, Vincenzo, Vito, Ippolito, Pio, Gabriele, e a tutti gli amici e compagni del Collegio Einaudi. Con voi, ho trascorso momenti indimenticabili negli ultimi anni universitari, un periodo di notevole crescita e cambiamento. Sono grato di aver vissuto questa fase con voi, che per me siete stati come una grande famiglia.

La mia famiglia merita un ringraziamento speciale. Ai miei nonni, nonostante le difficoltà, avete sempre fatto il massimo per farmi sentire il vostro amore. Sono stato fortunato ad avervi avuto con me. A Tonino e Pia, molto più di semplici zii, siete stati una fonte costante di aiuto ed esempio per tutti gli aspetti della vita. A voi devo parte di ciò che sono diventato. Ai miei genitori, fin dall'inizio siete stati al mio fianco, facendo ogni sforzo per fornirmi tutto ciò di cui avessi mai avuto bisogno. Mi avete cresciuto trasmettendomi valori che mi accompagneranno per tutta la vita, contribuendo in modo determinante a plasmare la persona che sono oggi.

Infine, desidero rivolgere un ringraziamento a me stesso. Per la crescita costante negli ultimi anni, per essermi sempre rialzato dopo ogni caduta, per aver imparato dagli errori, affrontato le sfide e colto le opportunità presentatesi. Grazie per non aver mai smesso di sognare.

Abstract

Hybrid rockets are promising propulsion systems with wide margins for yet unexplored development. In order to fully exploit the potential of these systems, the consideration of a hybrid fuel combining a solid grain and a liquid oxidizer is being examined. To achieve a fuel with low environmental impact and maximized performance, a Multidisciplinary Design Optimization (MDO) problem needs to be formulated. This involves the development of a MDO framework specifically for optimizing the solid grain, taking into consideration additive manufacturing constraints and utilizing a propulsion model to predict the specific impulse generated. Ultimately, a multi-objective function is established, combining both structural and performance goals.

Keywords: Topology optimization, Hybrid propulsion, Multidisciplinary design optimization, Rocket launcher.

Sommario

I razzi a propellenti ibridi rappresentano sistemi di propulsione promettenti con ampi margini per uno sviluppo ancora inesplorato. Al fine di sfruttare appieno il potenziale di questi sistemi, si sta esaminando la considerazione di un carburante ibrido che combini un grano solido e un ossidante liquido. Per ottenere un carburante con basso impatto ambientale e prestazioni massimizzate, è necessario formulare un problema di Multidisciplinary Design Optimization (MDO). Ciò comporta lo sviluppo di un framework MDO specifico per ottimizzare il grano solido, tenendo conto dei vincoli della stampa 3D e utilizzando un modello di propulsione per prevedere l'impulso specifico generato. In definitiva, viene stabilita una funzione multi-obiettivo che combina obiettivi strutturali e prestazionali.

Parole chiave: Ottimizzazione topologica, Propulsione ibrida, Multidisciplinary Design Optimization, Lanciatori.

Contents

List of Tables

List of Figures

Nomenclature

Greek symbols

ρ	Density	[kg/m^3]
ρ_c	Combustion chamber density	[kg/m^3]
ρ_f	Fuel density	[kg/m^3]
γ	Heat capacity ratio	
ν	Poisson's ratio	
ζ_d	Discharge correlation factor	

Roman symbols

a	Regression coefficient	
A	Area	[m^2]
A_b	Burnt area	[m^2]
A_c	Chamber area	[m^2]
A_e	Exit area	[m^2]
A_p	Port area	[m^2]
A_t	Nozzle throat area	[m^2]
c_p	Specific heat	[J/kg K]
c^*	Characteristic velocity	[m/s]
C_F	Thrust coefficient	
d	Internal diameter	[m]
D	External diameter	[m]
E	Young modulus	[Pa]
T	Thrust	[N]

g	Gravitational acceleration	[kg m/s^2]
g_c	Conversion factor	
G	Mass flux	[kg/m^2 s]
G_{ox}	Oxidizer mass flux	[kg/m^2 s]
h	Specific enthalpy	[J/kg]
I_{sp}	Specific impulse	[m/s] [s]
I_{vac}	Vacuum specific impulse	[m/s] [s]
L	Length port	[m]
$\dot{m}$	Mass flow	[kg/s]
$\dot{m}_{cc}$	Combustion chamber mass flow	[kg/s]
$\dot{m}_f$	Fuel mass flow	[kg/s]
$\dot{m}_{ox}$	Oxidizer mass flow	[kg/s]
n	Regression coefficient	
O/F	Oxidizer to fuel ratio	
p	Pressure	[Pa]
p_0	Chamber pressure assuming an ideal nozzle	[Pa]
p_c	Combustion chamber pressure	[Pa]
p_e	External pressure	[Pa]
P	Perimeter	[m]
P_c	Chamber perimeter	[m]
r	Internal radius	[m]
$\dot{r}$	Regression rate	[m/s]
R	External radius	[m]
R	Specific gas constant	[J/Kg K]
R_i	Inner radius	[m]
T	Temperature	[K]
T_0	Ambient temperature	[K]
T_c	Combustion chamber temperature	[K]

u	Flow velocity	[m/s]
u_e	Exit flow velocity	[m/s]
V	Volume fraction	

Subscripts

a	Ambient condition
c	Combustion chamber condition
e	Exit or downstream condition
inf	Free-upstream condition
t	Throat condition

Acronyms

ABS	Acrylonitrile Butadiene Styrene
Al	Alluminium
AM	Additive Manufacturing
AP	Ammonium Perchlorate
ASA	Acrylonitrile Styrene Acrylate
ASTM	American Society for Testing and Materials
BESO	Bi-directional Evolutionary Structural Optimization
C	Carbon
C_2H_2	Acetylene
CAD	Computer Aided Design
CEA	Chemical Equilibrium Applications
CFD	Computational Fluid Dynamics
CH_4	Methane
CO	Carbon Monoxide
CO_2	Carbon Dioxide
CO_2eq	Carbon Dioxide Equivalent
CONLIN	Convex Linearization
CVT	Centroid Voronoi Tessellation
ESO	Evolutionary Structural Optimization
FAC	Finite-Area Combustor
FDM	Fusion Deposition Modelling
FEM	Finite Element Method
GA	Genetic Algorithm
GOx	Gaseous Oxygen
GWP	Global Warming Potential
H	Hydrogen
H_2	Dihydrogen
H_2O	Water
H_2O_2	Hydrogen Peroxide

HAN	Hydroxyl-Ammonium-Nitrate
HCN	Hydrogen Cyanide
HDPE	High-Density Polyethylene
HIPS	High Impact Polystyrene
HNC	Hydrogen Isocyanide
HRE	Hybrid Rocket Engine
HTP	High-Test Peroxide
HTPB	Hydroxyl-Terminated PolyButadiene
IAC	Infinite-Area Combustion chamber
LCA	Life Cycle Assessment
LDPE	Low-Density Polyethylene
LH_2	Liquid Hydrogen
LOx	Liquid Oxygen
LRE	Liquid Rocket Engines
MDO	Multidisciplinary Design Optimization
ME	Material Extrusion
MMA	Methyl Methacrylate
MMA	Method of Moving Asymptotes
MMH	Monomethylhydrazine
MON	Mixed Oxides Nitrogen
N_2	Nitrogen Gas
N_2O	Nitrous Oxide
N_2O_4	Dinitrogen Tetroxide
NO	Nitric oxide
NTO	Dinitrogen Tetroxide
NYTROX	Nitrous Oxide and Gaseous Oxygen Mixtures
O	Oxygen
O/F	Oxidizer to Fuel ratio
O_2	Dioxygen
OC	Optimality Criteria Algorithm
OF_2	Oxygen Difluoride
OH	Hydroxide
PBF	Power Bed Fusion
PE	Polyethylene
PETG	Polyethylene Terephthalate Glycol
PLA	Polylactic Acid
PMMA	Poly(methyl Methacrylate)
PP	Polypropylene
PSPP	Process-Structure-Property-Performance

RFNA	Red Fuming Nitric Acid
RP1	Rocket Propellant-1 or Refined Petroleum-1
SIMP	Solid Isotropic Material with Penalization
SLA	Stereolithography
SLP	Successive Linear Programming
SLS	Selective Laser Sintering
SQP	Sequential Quadratic Programming
SRE	Solid Rocket Engines
STL	Standard Triangle Language
TO	Topology Optimization
xFEM	Extended Finite Element Method

Chapter 1

Introduction

This chapter serves the purpose of introducing the work conducted towards the completion of this master's thesis. An overview is provided on the chosen topic, the motivations is outlined, the objectives are defined, and ultimately, the structure of this document is described, with a brief explanation of the content covered in each chapter.

1.1 Topic Overview

Hybrid Rocket Engines (HREs) represent chemical propulsion systems where propellants are present in two distinct phases. They possess unique characteristics differing from other rocket typologies, namely solids and liquids.

In this master's thesis, the author presents an optimization process for the design of a hybrid rocket fuel grain. Specifically, the optimization targets a hollow cylinder made of printable Acrylonitrile Butadiene Styrene (ABS) material using Additive Manufacturing (AM) technology. This choice is grounded in promising research and capitalizes on the full potential and favorable attributes offered by AM. The Multidisciplinary Design Optimization (MDO) undertaken aims to simultaneously enhance both the structural and propulsion aspects of the grain.

1.2 Motivation

HREs represent a promising propulsion system, characterized by significant advantageous features, although their development has not paralleled that of other rocket types. The primary positive aspects are primarily rooted in enhanced safety, the potential for reduced costs, and lower environmental impact [1]. The latter, in particular, serves as a focal point increasingly converging in various industrial domains. To attain these potential benefits, a great research effort is thus essential, directed towards the optimization of hybrid rocket propulsion systems.

The optimization process of HREs can benefit from the combination of various cutting-edge technologies, enabling a thorough exploration of design possibilities.

In this context, from a production perspective, the utilization of AM is considered. This choice enables the creation of complex and innovative geometries, with less restrictive constraints compared to traditional manufacturing techniques. Additionally, it reduces material wastage during production, leading to cost savings and a reduced environmental impact. From the optimization process standpoint, the application of additive manufacturing facilitates the integration of optimization analyses, largely due to the increased design flexibility it offers [2]. Ongoing research in this field contributes to the development and enhancement of codes and software that play an increasingly central role in the design domain.

Furthermore, all aspects related to sustainability and environmental impact are taken into account, in a historical period in which they are more central than ever before. For this reason, it is imperative to continue researching materials that increase their sustainability through improved recycling processes and reduce their environmental impact by using or creating less polluting materials.

1.3 Objectives

The primary objective of this work involves developing a multidisciplinary optimization strategy for designing solid grain geometries to be used in hybrid rocket propulsion systems. This optimization is pursued from both structural and propulsion perspectives, aiming to achieve structural stability, to prevent potential failures, and maximize propulsion performance.

The main challenge in this endeavor lies in the interplay between the two distinct optimization domains: structural and propulsion. Regarding structural optimization, the goal was to minimize the compliance of the grain, while from the propulsion perspective, the optimization aimed at maximizing performance by maximizing specific impulse. Therefore, separate analyses were initially performed to outline potential optimization patterns for the two different domains. Subsequently, various MDO processes were executed to achieve the final optimized design.

Considering this, various subsequent investigations can be delineated, such as conducting experimental tests, exploring propellant combinations for reduced environmental impact, and integrating additional analyses within the optimization process.

1.4 Thesis Outline

This master's thesis comprises five chapters.

Chapter 1 introduces the work, providing an overview of the topic and describing the motivation, objectives, and the structure of the thesis.

Chapter 2 constitutes the primary phase of the literature review. It outlines the major topics that constitute this work. Firstly, it covers HREs, describing their functioning, delving into relevant studies, and analyzing propellants and geometries. Secondly, it explores AM, offering an overview of key printing methods and printable fuels. Lastly, it discusses topology optimization, briefly introducing its potential integration with 3D printing, and delves into Genetic Algorithms (GAs) to enable MDO implementation.

Chapter 3 presents the methodology employed, encompassing model definition, meshing process, structural analysis, regression analysis, performance evaluation, topology optimization, and MDO.

Chapter 4 provides an account of the outcomes derived from the various analyses conducted. It commences by elucidating the results of the regression analysis, serving to validate and compare the efficacy of the developed methodology. Subsequently, it delineates the optimization results, separately delving into both structural and propulsion aspects. Following this, the chapter elucidates the findings from the Multidisciplinary Design Optimization (MDO) analyses, classified into two categories: the first employs the original starting domain, while the second introduces double symmetry into the optimization process. Finally, the chapter culminates with a comparison, revisiting the latter double symmetry configuration but employing a different fuel with the aim of increasing sustainability. For this reason, the best-optimized designs obtained are considered and analyzed from an environmental impact perspective. By calculating their respective emissions, it is possible to make a comparison between the obtained designs and, in general, between the considered fuels.

Chapter 5 offers conclusions derived from the analysis results and the entire work in general and concludes by outlining potential future work and developments that can extend from the groundwork laid in this study.

Chapter 2

Literature Review

This chapter aims to present, in an extensive literature review phase, the main macro-topics concerning topology optimization of hybrid rocket fuels for additive manufacturing, with some preliminary analysis.

2.1 Hybrid Rocket Engines

Hybrid rocket engines (HREs) are chemical rocket propulsion systems with fuels and oxidizers in different phases of matter, mainly a solid fuel that has a liquid or gas oxidizer. Traditional HREs have a liquid oxidizer that flow across a solid fuel grain [3]. Figure 2.1 presents a schematization of a general HRE.

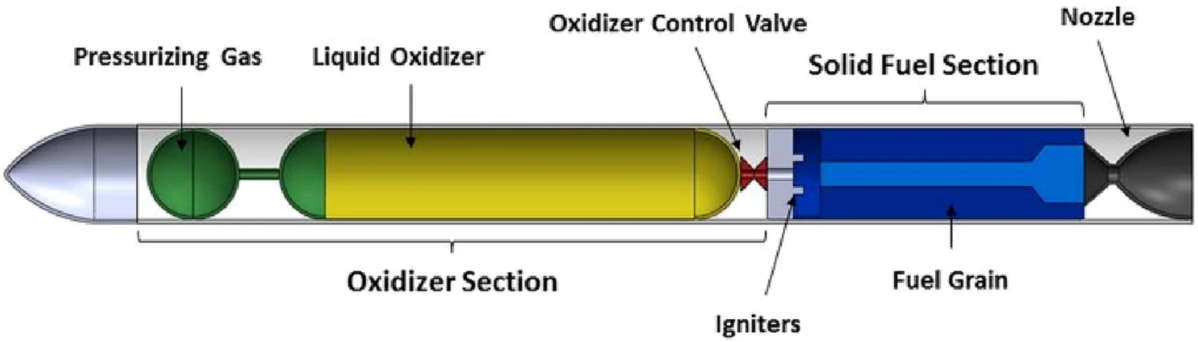

Figure 2.1: Hybrid Rocket Engine [4]

Interest in HREs emerged in the 1930s, culminating in the launch of the first hybrid rocket in 1933. It was called the Russian GIRD- 09, using gelled gasoline/colophony (solid resin/sap from pine trees) suspended on a metal mesh and Liquid Oxygen (LOx). Subsequently, significant advancements in hybrid rocket technology took place in the United States during World War II [5]. Unfortunately, HREs have not gained popularity of use like Solid Rocket Enginess (SREs) or Liquid Rocket Enginess (LREs) since they also suffer from several disadvantages of both. Nowadays HREs are still the object of university, industry and government research and development all over the world. They are used since 2018 on the SpaceShipTwo, an air-launched suborbital spaceplane manufactured by Virgin Galactic, and since

2015, remarkable growth has been seen in the research and development of small launchers vehicles, with a growing interest in hybrid propulsion vehicles [6, 7].

2.1.1 Overview

The idea of a HREs is to have the two propellants in different phases and to store the oxidizer in a tank separate from the inert fuel. This renders them less susceptible to chemical explosion than conventional LRE or SRE designs. The heat of the flame and blowing conditions cause the solid fuel to change its phase to vapor where it is then released from the fuel wall and contributes to further reactions. Fuel vaporizing or pyrolyzing at the face of the solid fuel grain causes the surface to regress. HREs are an attractive choice as an alternative to LREs and SREs, because they combine ideas from both LREs and SREs and try to benefit from the advantages of these more established engines [8].

Features unique to HREs are higher safety during operation and performance parameters that are intrinsically associated with the geometry. The performance of HREs is frequently challenged by the low fuel mass addition, which is a function of fuel geometry, and the flow rate of oxidizer. Often HREs have varying performance conditions that shift over the run duration. The primary changes that affect performance are the oxidizer and fuel ratio [9].

The main and unique properties of HREs are summarized below:

- Higher safety and manufacturing conditions;
- Performance parameters coupled with geometry;
- Less mechanical complexity than LREs;
- Less inert mass than LREs;
- Less toxic exhaust products than SREs;
- Simpler control mechanism like LREs.

A comparison of the proprieties with LREs and SREs is reported in Table 2.1, as it is clearly possible to see how the HREs represent a combination of them.

HREs enjoy several safety and environmental advantages over the other two systems, but it has never been commercially widespread. The main limiting factors of HREs are the low regression rate, due to the nature of the combustion process, and the low combustion efficiency [9].

The main factors influencing the regression rate are propellant composition, geometry of the grains, injector configuration and scale. Regarding the geometry issues, in the last years, new research trends have been developed that promote additive manufacturing and rapid prototyping as possible solutions and a beginning point for further studies [9]. For this reason, AM processes and printable fuels are later presented in this Chapter.

Table 2.1: Comparison between LRE, SRE and HRE [10]

	Liquid	Solid	Hybrid
Performance (*Isp*)	250-450 sec	200-280 sec	230-300 sec
Cost	High	Low	Moderate
Complexity	High	Low	Moderate
Throttle-ability	Yes	No	Yes
Restart	Yes	No	Yes
Explosive Hazard	Moderate	High	None
Handling & Transport Risk	Moderate	High	Very Low
Storability	Low	High	Moderate to High
Operational Risk	High	High	Very Low
Environmental Impact	Low to High	Moderate to High	Very Low

2.1.2 Internal ballistic and Combustion process

To explain the basic function of the HRE internal ballistic, it is necessary to begin with the geometric definition of the following parameters, considered for a cylindrical fuel grain as illustrated in Figure 2.2.

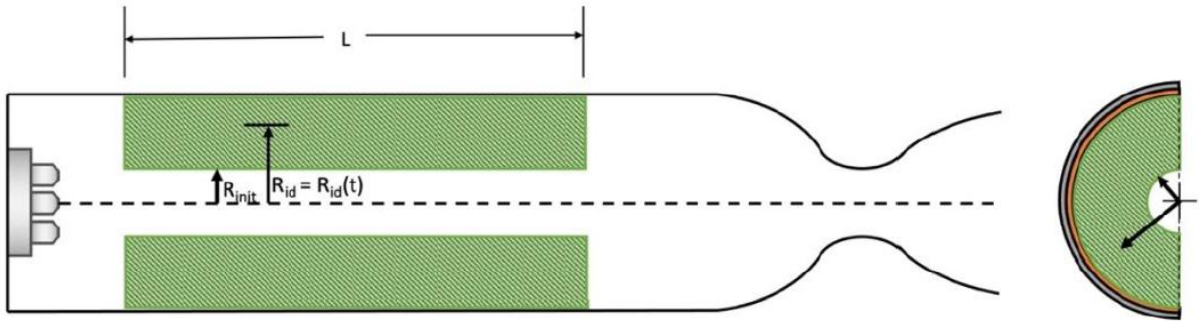

Figure 2.2: Schematic geometric representation of an HRE [9]

$$A_p = \pi \, R_i^2 \tag{2.1}$$

$$\dot{m}_{cc} = \dot{m}_{ox} + A_p \, \dot{r} \, \rho_f \tag{2.2}$$

$$A_b = 2\pi \, R_i \, L \tag{2.3}$$

Equation 2.1 describes the port area A_p as a function of the inner radius R_i. Equation 2.2 determines the combustion chamber mass flow $\dot{m}$ by two factors, the oxidizer mass flow $\dot{m}_{ox}$ and the fuel mass flow

due to the regression as a function of A_p, regression rate $\dot{r}$ and fuel density ρ_f. Equation 2.3 describes the burnt area A_b as a function of R_i and length port L.

The main parameter in internal ballistic analysis is the regression rate $\dot{r}$, which indicates the rate of fuel consumption or burning from the burning surface. A more detailed relationship to express this parameter is derived from the mathematical modeling of Marxman's analysis [11], as shown in Equation 2.4, where G represents the mass flux, x is the axial combustion port location, μ is the combustion gas viscosity, and β is the blowing coefficient. This last equation can only be used with English units [9].

$$\dot{r} = 0.036 \, \frac{G^{0.8}}{\rho_f} \, \left(\frac{\mu}{x}\right)^{0.2} \, \beta^{0.23} \tag{2.4}$$

However, the expression for the regression rate is typically simplified as shown in Equation 2.5, where the coefficients a and n are experimentally determined, specific to fuel and oxidizer combinations and dependent on many factors such as combustor design, facility effects, measurement approach, etc [12]. On the other hand, the mass flux G relation is obtained analytically as presented in Equation 2.6. This latter parameter is the driving one for the rocket performance, because it drives the regression of the port section.

$$\dot{r} = a \, G^n \tag{2.5}$$

$$G = \frac{\dot{m}}{A_p} \tag{2.6}$$

This simplification assumes a constant regression rate along the grain, independent of pressure. It's worth noting that in place of the mass flux G, the oxidizer mass flux G_{ox} is also used, with the coefficients adjusted accordingly. In this work, the latter case will be implemented, as described in the following chapter.

The regression rate's behavior as a function of mass flux is not uniform. However, it can be divided into three main regimes, as illustrated in Figure 2.3. The first regime is characterized by thermal radiation effects, the second by turbulent heat transfer, and the third by chemical kinetic effects. Typically, HREs operate within the second regime, which exhibits dependencies on scale effects, geometry, and additives.

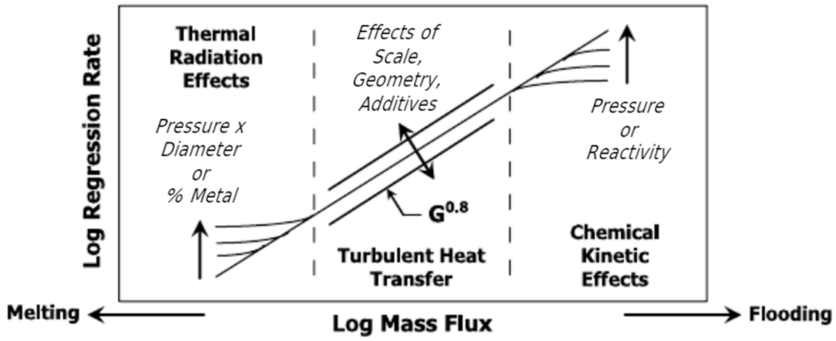

Figure 2.3: Regression rates regimes and their corresponding parameter dependencies in HREs [8].

The correlation of the regression rate with mass flux is typical of HREs, unlike the SREs that have relationship with the pressure, as described by the Saint/Robert law [13]. So, HREs have a weak correlation with pressure and the dependency on mass flux makes their analysis more difficult. By combining the previous two equations one obtains Equation 2.7. Considering the mass flux as constant and simple geometries, it shows an inverse proportionality to the port radius.

$$\dot{r} = a \left(\frac{\dot{m}}{\pi R_i^2} \right)^n \tag{2.7}$$

Finally, comparing Equations 2.1 and 2.3, it is possible to notice two of the main HRE problems. The burned surface is always less than the cross-section area and this leads to an inconsistent burn rate with time and an inability to easily scale for larger performances. Regarding the combustion process, it is clear that HREs rely on the boundary layer combustion to generate hot gas. The most used HRE propellants are polymer fuels, which evaporate slowly, making it difficult to reach a high thrust level. For this reason, the burning surface area needs to be increased, however, this leads also to an increase of required ports and so to a wagon wheel geometry of the fuel grain [9]. Some types of fuel present several problems during the combustion process, mainly due to a phenomenon called sloughing. It happens when a significant portion of the solid wall transforms into liquid droplets before forming a vapor, instead of vaporizing in preparation for combustion. These fuel droplets are entrained into the combustion mass flow and this can also produce some fuel grain disfiguration. Fuel can flow toward the nozzle outlet and this results in a significant amount of un-combusted fuel, fuel slivers/globs, and obstruction of the outlet. Of course, this issue leads to a different regression rate behaviour [9]. Figure 2.4 depicts the typical HRE flame boundary layer, with and without the sloughing problem.

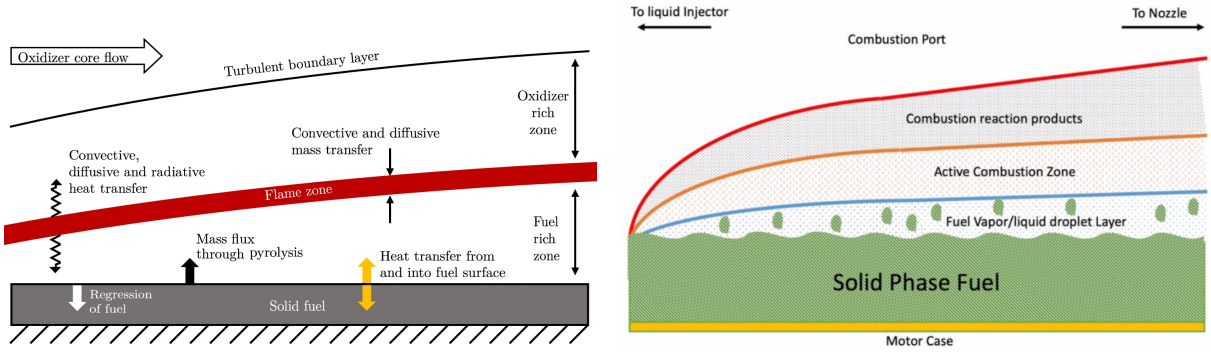

(a) Generic flame boundary [14]

(b) Flame boundary with sloughing [9]

Figure 2.4: Flame boundary layer

2.1.3 Propellants

The evaluation and determination process of the propellant is one of the main starting points for the propulsion analysis. The fuel and oxidizer combination affects the regression rate and also certain Oxidizer to Fuel ratio (O/F) ratio values are needed to produce efficient combustion. The most common fuels and oxidizers are listed in Table 2.2 and are described in the next paragraphs [9].

Table 2.2: List of most common HREs propellants [9]

Fuels	Oxidizers
HTPB (Hydroxyl-Terminated PolyButadiene)	LOx cryogenic (Liquid oxygen)
HTPB + Aluminium additives	N_2O (Nitrous Oxide) cryogenic
PE (Polyethylene)	N_2O_4 (Dinitrogen Tetroxide)
HDPE (High-Density Polyethylene)	H_2O_2 (Hydrogen Peroxide)
MMA (Methyl Methacrylate)	HAN (Hydroxyl-Ammonium-Nitrate)
Paraffin wax	RFNA (Red Fuming Nitric Acid)
ABS (Acrylonitrile Butadiene Styrene)	OF_2 (Oxygen Difluoride)

- Hydroxyl-Terminated PolyButadiene (HTPB)

HTPB is one of the most commonly used fuels in HREs and is also a common binder agent used for solid propellants. Its classical use is paired with Liquid Oxygen (LOx) [15]. Figure 2.5 portrays the performance of HTPB with the increase of the O/F ratio, for various different oxidizers. The highest values of specific impulse are obtained for the fluoride oxidizers, and generally the optimum O/F ratio values are between 2 and 7. The higher performance obtained for the HTPB justifies its widespread use is shown how much the specific impulse can change using different oxidizers.

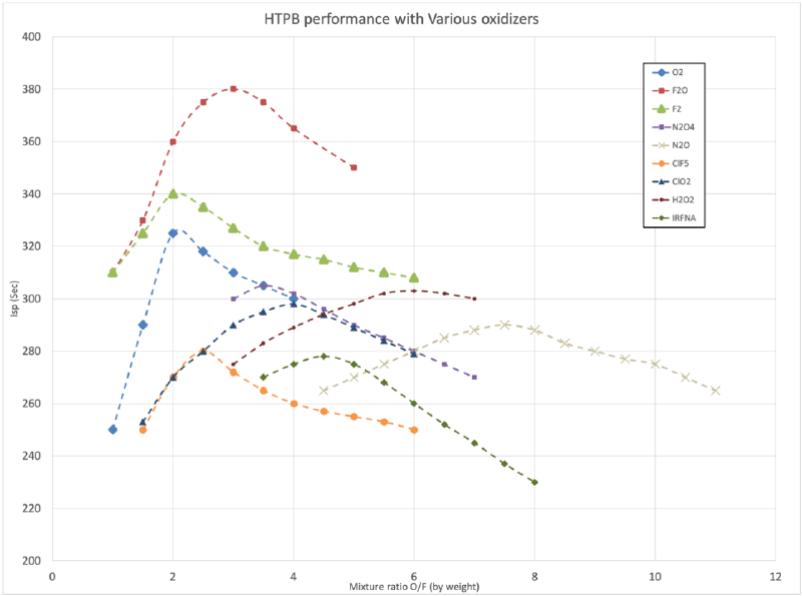

Figure 2.5: Specific Impulse of HTPB versus various O/F ratios, considering various oxidizers [9]

- Polyethylene (PE) and High-Density Polyethylene (HDPE)

PE and HDPE are easy to shape form and manufacture into fuel grain. These fuels are often used for full-scale rocket applications. Studies conducted on them demonstrated easy throttling via a valve and stable combustion, although their regression rates had limited capability to improve [10]. The high-

density variant is more efficient when considering thrust efficiency and flight conditions. HDPE is commonly used with Nitrous Oxide (N_2O), Dinitrogen Tetroxide (N_2O_4), Liquid Oxygen (LOx), Gaseous Oxygen (GOx) and High-Test Peroxide (HTP), that is a highly concentrated solution (85 to 98%) of Hydrogen Peroxide (H_2O_2) [9].

- Methyl Methacrylate (MMA)

MMA is another popular fuel belonging to the family of clear rigid plastics. It is used with Nitrous Oxide (N_2O), Mixed Oxides Nitrogen (MON) of various concentrations, Dinitrogen Tetroxide (N_2O_4), Red Fuming Nitric Acid (RFNA), or Liquid Oxygen (LOx) [9].

- Paraffin

Paraffin wax is a commonly used fuel for smaller engines and test applications. It is easy to manufacture and shape, and it has shown regression rates up to 3 to 4 times higher than that of other polymer fuels. This wax has a higher heat of vaporization than that common wax. This fuel has several problems when burning, mainly due to sloughing. It is classically used with High-Test Peroxide (HTP), Liquid Oxygen (LOx), and Nitrous Oxide (N_2O) [9].

Properties and performance metrics of various combinations of propellants previously presented are reported in Table 2.3, where it is possible to see the compliance of the performances with Table 2.1.

Table 2.3: Performances capability for several hybrid propellants [8]

Fuel	Oxidizer	Optimum O/F	$\mathbf{I_{sp}}$, s	$\mathbf{c^*}$, m/s
HTPB	LOx	1.9	280	1820
PMMA	LOx	1.5	259	1661
HTPB	N_2O	7.1	247	1604
HTPB	N_2O_4	3.5	258	1663
HTPB	RFNA	4.3	247	1591
HTPB	OF_2	3.3	314	2042
HTPB	OF_2	2.8	326	2118
PE	LOx	2.5	279	1791
PE	N_2O	8	247	1600
Paraffin	LOx	2.5	281	1804
Paraffin	N_2O	4	248	1667
HTPB/Al (40%)	LOx	1.1	274	1757
HTPB/Al (40%)	N_2O	3.5	252	1637
HTPB/Al (40%)	N_2O_4	1.7	261	1679
HTPB/Al (40%)	OF_2	2.5	312	2006
Cellulose ($C_6H_{10}O_5$)	GOx	1	247	1572
Carbon	Air	11.3	184	1224
Carbon	LOx	1.9	249	1599
Carbon	N_2O	6.3	236	1522

Another comparison between different combinations of propellant is shown in Figure 2.6. These graphs are obtained considering a pressure at the combustion chamber of $p_c = 20$ bar and $p_c/p_e = 20$, in a condition of equilibrium flow. Specific impulse and density specific impulse are plotted for different oxidizer-to-fuel ratios. The density specific impulse can be calculated to compare the effectiveness of the potential use of different propellants in rocket vehicles, taking into account not only their specific impulse but also their density. The results of this calculation were done using NASA Chemical Equilibrium Applications (CEA) Software [5, 16]. It is possible to see the better performances of HTPB and paraffin fuels with Liquid Oxygen (LOx) oxidizer, similar to Table 2.3. The following comments can be made regarding the specific impulse of the different fuels by comparing the two graphs: the PE and HTPB fuels, with HTP oxidizer, present higher values due to the higher density of the propellant combination; HTPB and paraffin, with LOx, present similar trends due to the almost unitary density of the propellant mix; while HTPB and paraffin, with Nitrous Oxide (N_2O) and NYTROX (mixtures of nitrous oxide and gaseous oxygen), present lower values due to the reduced density of the propellant. It is clear that it is possible to load more propellant with less density specific impulse considering a fixed volume, so also this aspect has to be evaluated.

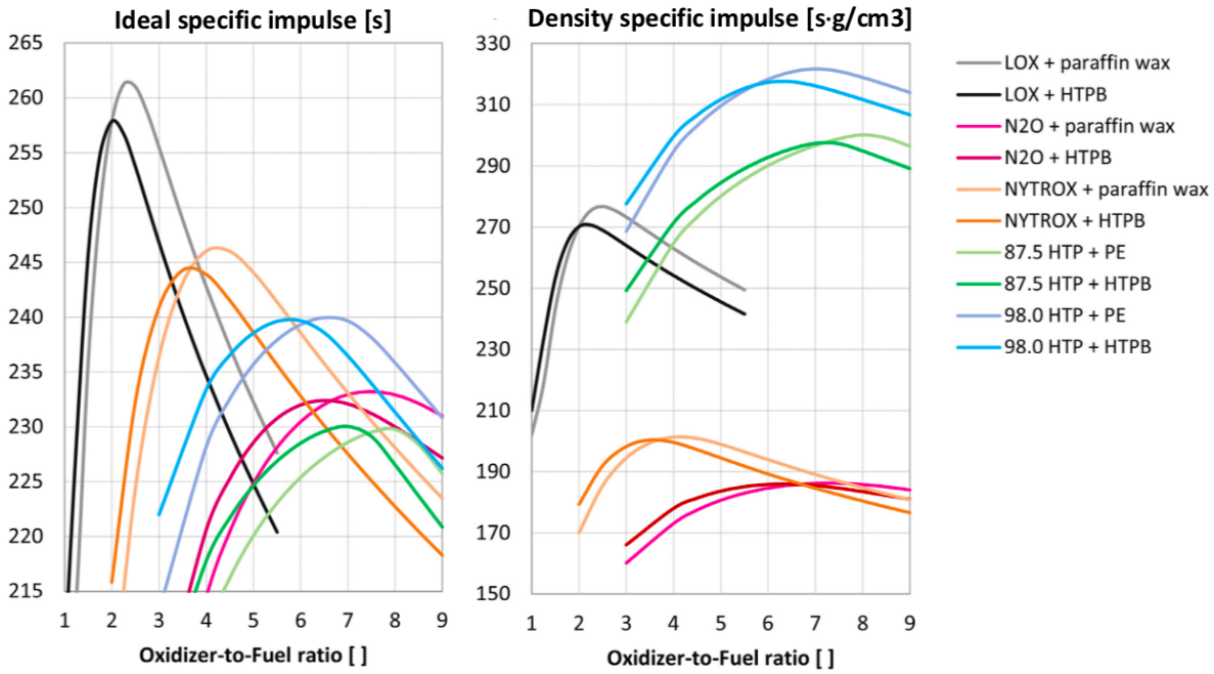

Figure 2.6: Comparison of ideal specific impulse and density specific impulse of various propellant combinations [5]

The improvement of the specific impulse of chemical propulsion systems can be reached increasing the combustion temperature and the hydrogen content in the propellants [17]. Unlike the SREs, using metal additives does not significantly contribute to the increase of the specific impulse, as it is also possible to see from Table 2.3 [18]. Another innovative approach considers including reinforcement structures within the solid fuel grain, which allows for modifying grain mechanical properties, heat transfer and thus grain regression. Increasing the grain thermal conductivity is the most direct way to enhance the regression rate. Moreover, the addition of up to a few percent of carbon black to the grain can be considered

a low-cost solution [5]. Finally, Table 2.4 reports a performance comparison between an HRE and a typical SRE and LRE. The HRE is equipped with HTPB and LOx, one of the most studied couples of hybrid propellants. It is possible to see that the hybrid system is potentially better than the solid solution and also competitive with the liquid solution (both liquid and bipropellants) [15].

Table 2.4: Performance comparison of solid, hybrid and liquid LOx/HTPB fuel type [15]

Propellant		**Mixture ratio**	**Equivalent density** $\mathbf{kg/m^3}$	$\mathbf{I_{SV\ th}}$ $(\mathbf{Pe = 7MPa}, \sum \mathbf{= 40})$
Solid	AP/HTPB/Al	68/18/14	1750	315
Hybrid	LOx/HTPB	72/28	1060	354
Liquid	NTO/MMH	2.37	1200	341
Bipropellants	H_2O_2/RP1	7.0	1320	314
	LOx/RP1	2.77	1030	358
	LOx/CH_4	3.45	830	369
	LOx/LH_2	4.8	320	455

2.1.4 Geometries

The regression rate increase, as mentioned in Section 2.1.1, is the main focus of research and development of HREs. In this chapter, some different approaches have been described, each with some disadvantages, and the discussion is now focused on how the geometry affects the regression rate. Some typical different fuel port designs are shown in Figure 2.7.

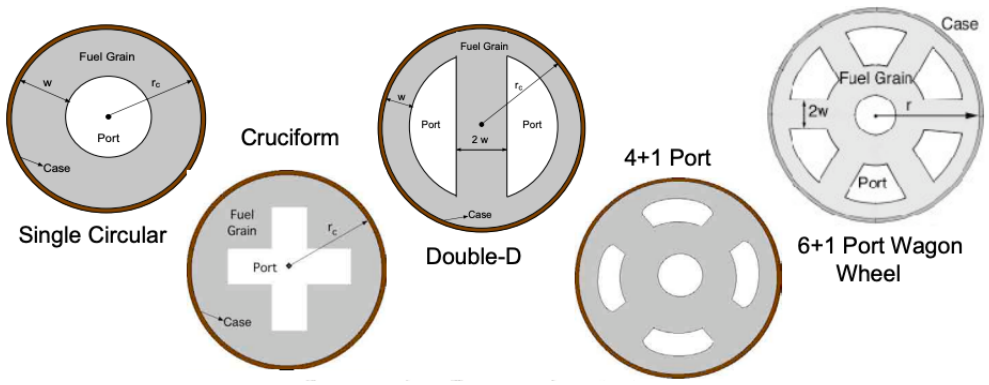

Figure 2.7: Various typical fuel port designs and their dependence with regression rate [19]

The first and simplest fuel port geometry is the single circular one. This is the introductory geometry used to define and describe basic HREs, as done in Section 2.1.2. Moreover, researches on paraffin show the effectiveness of a single port, due to the faster regression rate led by this fuel [8].

A possible method to increase the fuel grain surface burn area is the casting of multiple fuel ports, with a large pre-combustion chamber or multiple injectors. This is done to reach highly efficient and stable combustion, by improving the fuel mass flows for oxidizer mass flux levels. However, this multiple port approach presents several disadvantages:

- Fuel regression rate reduction with the increase in the number of ports, due to the drop in oxidizer mass flux and the engine diameter size growth, as shown in Figure 2.7;
- Uneven port burning that produces an excessive un-burned mass fraction. Un-burned fuel slivers can break off the fuel grain and throw chunks out the back of the rocket;
- Increased risk of motor instability related to dynamic flow interactions between ports and/or the presence of a large pre-combustion chamber.;
- Requirement for a substantial pre-combustion chamber or individual port injectors and embedded support structure often needed for multi-port design regression [19, 20].

In the last years, rapid prototyping by means of additive manufacturing has been identified to be a technique to produce geometrically complex grain shapes, that may solve the HREs performance problems. New concepts like helix ports, coaxial ports, swirls, spiral-star patterns with central ports have been tested [9, 20]. In comparison to simple port geometry, the star-swirl or helix shapes showed improvements in regression rate. These are shown in Figure 2.8.

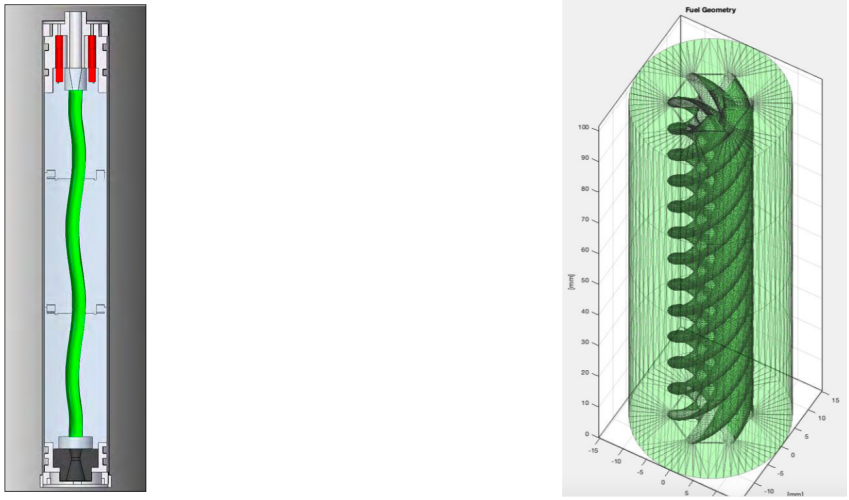

(a) Helical geometry (b) Star-swirl geometry

Figure 2.8: Representation of complex fuel port geometries [9, 20]

Helical fuel port studies showed regression rate increases, from up to 50% to a factor greater than 3 in some instances, and also volumetric efficiency improvement. Many researchers considered Acrylonitrile Butadiene Styrene (ABS) with Gas Oxygen as propellant, due to the easy shape building of this material using Fusion Deposition Modelling (FDM) processes (see Section 2.2). Presented analysis has demonstrated that the rotational flow velocity within the fuel port is a primary driver for the regression rate amplification. Centrifugal flow patterns introduced by the embedded fuel port structures dramatically increase fuel regression rates, by enhancing surface skin friction, and reduce the effect of radial boundary layer “blowing” outflow. These two mechanisms work together to enhance the convective heat transfer to the fuel surface [9, 20].

Star-swirl geometries studies indicate an increase of the burn surface area at the start of burn to about 3 times that of a tube grain. Most regression rates of the profile are higher and also combustion efficiency is better, since the spiral induces a swirl in the aft mixing chamber [21, 22].

Lastly, it is important to underline the strong dependence between the grain geometry and the thrust profile. Figure 2.9 shows various fuel solid designs with their respective thrust-time programs. So, it is clear that the geometry evaluation process has to be considered also in the specific rocket mission profile.

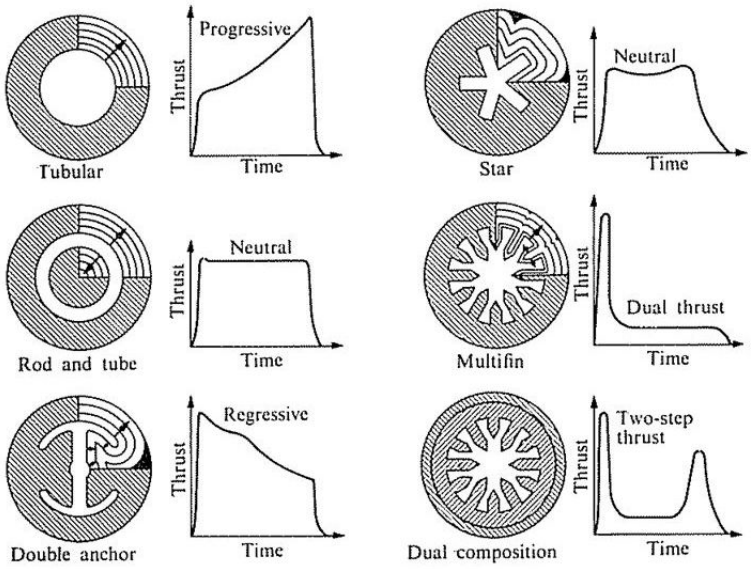

Figure 2.9: Internal burning change designs with their thrust-time programs [23]

2.2 Additive Manufacturing

Additive Manufacturing (AM), also called 3D printing, consists of the construction of a three-dimensional object from a digital 3D model. It can be done in a variety of processes in which material is deposited, joined or solidified under computer control, typically layer by layer [24].

The birth of 3D printing can be attributed to Charles Hull, who filed a patent for stereolithography in 1986 [25]. The primary idea was to use this technology to create a 3D model from a drawing and allow users to test a design before investing in a larger manufacturing program. He also invented the Standard Triangle Language (STL) file format, which describes a raw, unstructured triangulated surface, through the unit normal and the triangles vertices, using a three-dimensional cartesian coordinate system [26].

STL files describe only the surface geometry of a three-dimensional object without any representation of colour, texture or other common Computer Aided Design (CAD) model attributes. This file format is supported by many software packages, it is widely used for rapid prototyping, 3D printing and computer-aided manufacturing [27].

2.2.1 Printing Methods

The American Society for Testing and Materials (ASTM) group “ASTM F42 - Additive Manufacturing”, formulated a set of standards that classify the range of Additive Manufacturing processes into 7 categories, reported in Table 2.5 [28]. Figures 2.10, 2.11 and 2.12 show three different types of printing methods that are presented in this section.

Table 2.5: Additive Manufacturing processes categories [28]

VAT Photopolymerization	Powder Bed Fusion	Material Jetting	Sheet Lamination
Binder Jetting	Direct Energy Deposition	Material Extrusion	

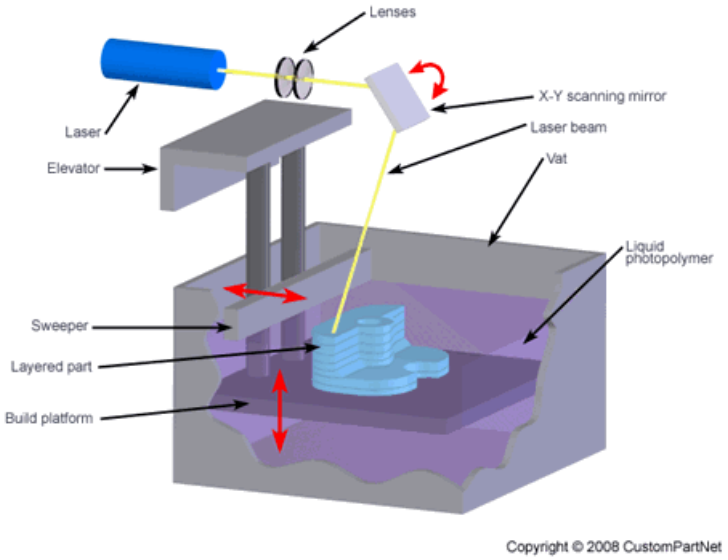

Figure 2.10: Stereolithography (SLA) [29]

- Stereolithography (SLA)

SLA, developed and patented by Chuck Hull in 1986, is the best-known technique that uses the principle of photopolymerization to create new models. The SLA process is carried out by means of Digital Light Processing, i.e. a photochemical transformation of a polymer. SLA printers are made up of a beam of ultraviolet light, a system of mirrors, a tank designed to contain the liquid polymer, a lift platform that will support the object to be made and move it progressively downwards after the completion of each individual layer, an ultraviolet light oven and possible supports to withstand the parts of the object during construction. After virtually subdividing the CAD into horizontal two-dimensional planes, the software transmits the information to a laser source. The laser strikes the liquid photopolymer contained in the mirror system, causing it to harden. Once solid, the thin layer formed is lowered thanks to the platform-lift: new liquid resin is exposed and ready to be hardened. The new layer formed will overlap the previous one. It is the joining of these layers that will determine the construction of the object. At the end of manufacture, the solid extracted from the liquid resin is placed in an ultraviolet light oven to complete polymerization [29].

- Fused Deposition Modelling (FDM)

FDM is a Material Extrusion (ME) process that consists of a heated plastic material ejected from a nozzle that builds the two-dimensional planes of the object layer by layer. The material used is in the form of a filament, that is led to the extruder, which uses torque and a pinch system to feed and retract the precise filament amounts. Then a heater block melts the filament to a usable temperature and forces it out of a heated nozzle at a smaller diameter, so the extruded material is laid down on the model where it is intended. The temperature of the extrusion head and working surface is very important for the success of the object. The platform has a lower temperature so that the plastic hardens as soon as it is deposited. Once each layer is completed, the platform lowers and the extrusion head deposits another layer of material. This method has restrictions on the shapes, structures with hollow parts must be avoided or supports must be used, which will be removed once the process is complete [30].

The main parameters of this method are:

- Material properties;
- Distance between the nozzle and the print bed;
- Thickness of the layer;
- Temperature of the printed model during the printing;
- Printing speed, which depends on the nozzle diameter, the printing temperature and the material pressure inside the liquefier chamber.

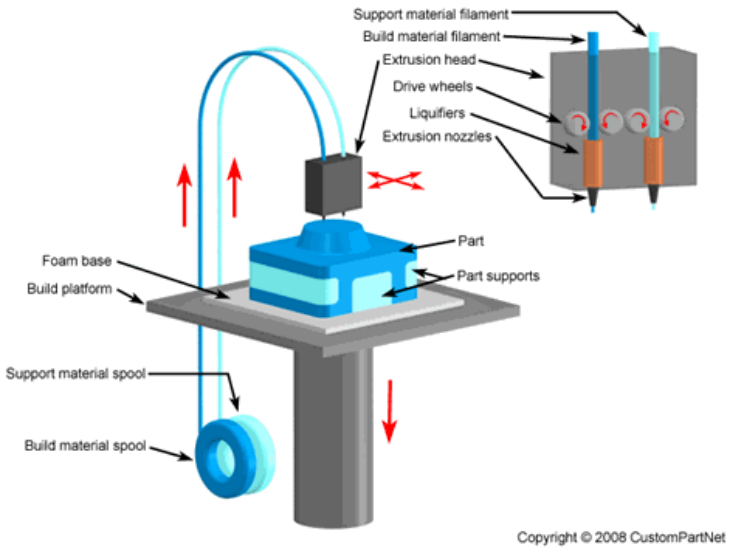

Figure 2.11: Fused Deposition Modelling (FDM) [30]

- Selective Laser Sintering (SLS)

SLS is the first commercialized Power Bed Fusion (PBF) process and its working is similar to the SLA process. It is made by a moving laser beam to selectively sinter powder into successive cross-sections of a three-dimensional part. As in all rapid prototyping processes, the parts are built upon a platform that adjusts in height equal to the thickness of the layer being built. Additional powder is deposited on top of each solidified layer and sintered. This powder is rolled onto the platform from a bin before building the layer. The powder is maintained at an elevated temperature so that it fuses easily upon exposure to the laser. Unlike SLA, special support structures are not required because the excess powder in each layer acts as a support to the part being built. SLS was originally developed for plastic materials but then it was subsequently extended to metal and ceramic powders. After the printing process, the part is placed in a furnace and the polymer binder is burned off and bronze infiltration is made to improve density [31].

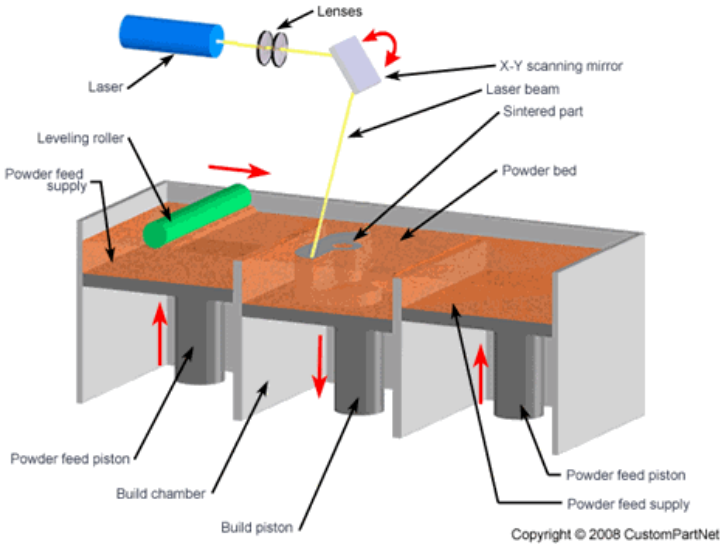

Figure 2.12: Selective Laser Sintering (SLS) [31]

2.2.2 Printable Fuels

As aforementioned in Section 2.1, the most significant limitation of HREs is the low regression rate. In order to reach sufficient levels of regression rates, it is necessary to implement certain structural and chemical modifications to the fuel grains. A possible solution is the use of paraffin-based fuels, which inherently exhibit superior regression rates compared to other polymeric fuels due to the lower viscosity that promotes droplet entrapment within the lame zone [32]. Despite these advantages, paraffin-based fuels suffer from poor mechanical strength compared to polymeric fuels, which led to the utilization of additives such as elastomers and thermoplastics at the expense of regression rate [33].

About the possibility of using printable fuels to improve performance, researches have been made about ME processes to print thermoplastic hybrid rocket fuel grains as ABS, High Impact Polystyrene (HIPS), HDPE and Poly(methyl Methacrylate) (PMMA). In particular, ABS presents good properties to replace the HTPB, as it is reported in the studies conducted by Stephen Whitmore at Utah State

University [34, 35].

Whitmore studies led to the development of a model to evaluate the effects of helical fuel ports on regression rates decomposing it into two components, the skin friction enhancement and the radial wall blowing suppression. A comparison between helical geometries of ME-printed ABS burned using Gaseous Oxygen (GOx) reported an increase of 75% in regression rate, attributed to the rising of skin friction levels due to the helical rotation [36].

It was also concluded that ME printed ABS samples were also found toexhibit higher consistency in burn performance, due to the automatednature of the additive manufacturing process [37].

Additionally, ME printing has been highlighted for its efficient use of volume in HREs. Despite its affordability and simplicity, one of the main limitations of thermoplastic material extrusion is the immiscibility of the polymers into efficient, novel, composite hybrid rocket fuels [34].

A comparison between seven different printed fuel grains, through a small-scale static fire test, is reported in a research conducted by McFarland and Antunes at James Cook University [38]. The materials evaluated are shown in Figure 2.13 (before and after the burning test), with the respective properties and results presented in Tables 2.6 and 2.7. In this study, the Acrylonitrile Styrene Acrylate (ASA) and Nylon fuel grains showed the highest regression rates $\dot{r}$, while Polyethylene Terephthalate Glycol (PETG) regression rates were relatively poor. Instead Polylactic Acid (PLA), PLA with aluminum particles, and Polypropylene (PP) exhibited values similar to each other and within the average range. The experiment design of this study was very simple, as the main objective was to select the FDM materials for a large-scale test [38].

Table 2.6: The selection of seven different fuel grains tested, with their properties [38]

Material	**Structure**	ρ **(g·m^{-3})**	**Tensile Yield Strength (MPa)**	**Printing Temperature (°C)**
ABS	Non-crystalline, amorphous	1010	55	220-260
ASA	Non-crystalline, amorphous	1000	40	220-250
PLA	Moderate degree of crystallinity	1225	63	190-220
PLA-Al	Moderate degree of crystallinity	1330	70	200-220
PETG	Moderate degree of crystallinity	1230	50	230-250
Nylon	Moderate degree of crystallinity	1150	55	220-260
PP	High degree of crystallinity	980	40	230-260

(a) Before test, in order: ABS, PLA, PETG, PP, ASA, Nylon, PLA-Al

(b) After test, in order: ABS, PLA, PP, ASA, PETG, PLA-Al

Figure 2.13: Fuel grain specimens, before and after combustion test [38]

As mentioned at the beginning of this section, the use of composite fuels can be necessary to improve the performance of HREs, and especially for this reason the ME methods have high importance. Through this process it is possible to build structural frameworks of composite fuel, where a second material can be casted or pulverized in printed molds, obtaining intricate shapes and superior ballistic performances. The additives of the polymeric matrix are usually pulverized coal, petroleum coke, graphite, and paraffin, as mentioned at the beginning of this section. ME printed Acrylonitrile Butadiene Styrene (ABS) with casted paraffin composite solid fuel grains are a very new and attractive type of fuel, because the melting point of the paraffin is lower than the glass transition temperature of the ABS, making the choice of this process perfect for this combination of materials [34].

In literature, there are several studies about increasing the performance of ABS-Paraffin fuel and here are reported some examples. Firstly, a research about a fabricated fuel grain with helical and straight ports with minimal post-processing, facing the incomplete combustion of ABS and marginal regression rate enhancement of hybrid rockets. Ballistic tests conducted using GOx resulted in an amplification of the regression rate of about 6 to 7 times under a low O/F ratio of 0.6 [39]. Secondly, another study on printed ABS substrates with swirl patterns as a framework for casted paraffin, tested using methane and GOx, reported an increase of 20% in regression rate [40]. Thirdly, another research conducted by McCulley, about composite fuel grains with varying amounts of ME-printed ABS and paraffin burned with N_2O, showed a maximum regression rate of 3 mm/s under an O/F ratio of 3.9 [41]. Finally, McKnight made a comparison between star-swirl port samples in ME-printed ABS and different configurations of diaphragm samples in paraffin and acrylic. The first ones reported an average regression rate between 0.58 and 1.00 mm/s, whereas the second ones marked between 0.48 and 4.79 mm/s, clearly proving a higher regression rate than paraffin [42]. Figure 2.14 shows ME printed composite fuel grains of ABS and paraffin.

Table 2.7: Result of the small-scale test fire of the selected 3D printed fuel grains [38]

Material	ρ **(kg m^{-3})**	$\dot{m}_{ox}$ **(kg s^{-1})**	$\dot{m}_{fuel}$ **(kg s^{-1})**	**O/F Ratio**	$\dot{m}_{total}$ **(kg s^{-1})**	$\dot{r}$ **(mm s^{-1})**
ABS	1010	0.0100	0.0023	4.35	0.0123	1.05
ASA	1000	0.0125	0.0030	4.17	0.0155	1.05
Al	1330	0.0108	0.0025	4.32	0.0133	1.20
PLA	1225	0.0100	0.0025	4.00	0.0125	1.23
PETG	1230	0.0108	0.0035	3.09	0.0143	0.94
Nylon	1150	0.0100	0.0027	3.70	0.0127	1.51
PP	890	0.0100	0.0023	4.35	0.0123	1.23

Over the already mentioned low mechanical strength of the paraffin, there are other negative aspects. The most significant drawback of pristine paraffin is the liquefaction behaviour, opposite to the softening phenomenon in thermoplastics, that makes hard the ME-printing. Therefore, the utilization of 3D-printed thermoplastic base structure becomes essential for integrating paraffin-based fuels, resulting in a marked reduction in regression rates [34].

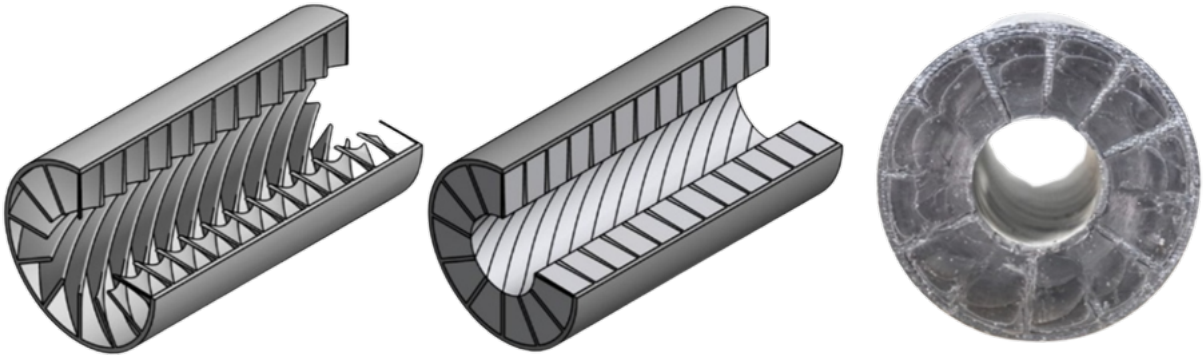

Figure 2.14: Structure of composite fuel grain: a) Acrylonitrile Butadiene Styrene (ABS) matrix, b) Grain filled with paraffin, c) Real image of the grain [40]

In conclusion, it is possible to affirm that the ME printed composite fuel grains made of ABS and paraffin, mostly with helical port, represent one of the best-studied solutions in the field of HRE fuels printable with additive manufacturing. So, it could be considered a good beginning point for future research and optimization.

2.3 Topology Optimization

Topology Optimization (TO) involves determining whether there is material present at every point within a given space. When applied using a Finite Element Method (FEM) discretization, each element can potentially be treated as either a void or a structural component. As the structure's topology is not predetermined, a generalized formulation should enable the prediction of the structure's layout [43].

Illustrated in Figure 2.15, topology optimization can be conceptualized as a mathematical technique that optimizes the distribution of structural material within a designated design space, considering a defined set of loads, boundary conditions, and constraints, all with the aim of maximizing system performance. This approach has been under development since the 1990s. The initial standard methodology involves introducing boundary variations to a given structural topology.

In the conventional approach to topology optimization, the finite element method is used to assess structural performance. The design is then optimized using various methods. Notable among these methods are Solid Isotropic Material with Penalization (SIMP) and Evolutionary Structural Optimization (ESO), along with Bi-directional Evolutionary Structural Optimization (BESO) [44]. A succinct description of these three methods is provided in Table 2.8. Similarly, several algorithms have been devised, and a summary of these can be found in Table 2.9 [45, 46].

Table 2.8: Description of some topology optimization approaches [44]

Topology Optimization Approaches	
Element-based approaches	
Solid Isotropic Microstructures with Penalization (SIMP)	Density-based approach that involves the discretization of the problem domain in a number of finite elements whose solution is known or can be approximated [43].
Discrete approaches	
Evolutionary Structural Optimization (ESO)	Iterative process with discrete variables that remove material deleting elements with the lowest criterion function value [47]
Combined approaches	
Extended Finite Element Method (xFEM)	The purpose is the introduction of a generalized and adaptive finite element scheme that could allow us to work with meshes that can represent smooth and accurate boundaries [48].

Table 2.9: Description of some topology optimization methodologies [45, 46]

Topology Optimization Methodologies	
Optimality Criteria Algorithm (OC)	Fundamental gradient-based mathematical method with proportional dependency between the design variables and the values of the objective function [49].
Convex Linearization (CONLIN)	Linear mathematical programming method with mixed variables and respect to the problem's characteristics [50].
Method of Moving Asymptotes (MMA)	More aggressive version of CONLIN that is expanded by moving limits. It creates an enormous sequence of improved feasible solutions of the examined problem and it can handle general non-linear problems and simultaneously take into account both constraints, design variables and characteristics of the structural optimization problem [51].
Successive Linear Programming (SLP)	Technique for approximately solving nonlinear optimization problems by a sequence of model linearizations [52].
Sequential Quadratic Programming (SQP)	Iterative method for constrained nonlinear optimization. It solves a sequence of optimization subproblems, each of which optimizes a quadratic model of the objective subject to a linearization of the constraints [52].

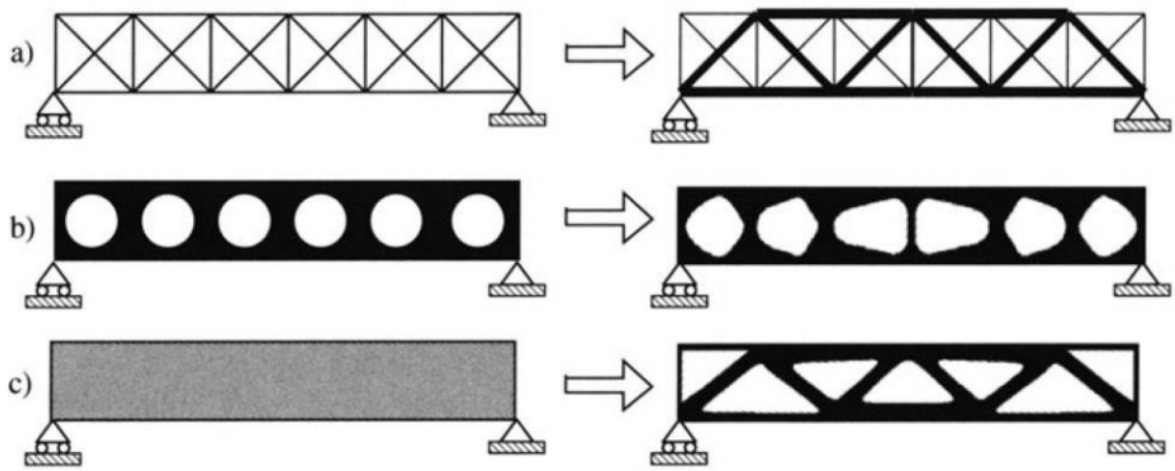

Figure 2.15: Illustration of different categories of structural optimization by: a) size, b) shape, c) topology [45]

2.3.1 Topology Optimization for Additive Manufacturing

The emergence of topology optimization was closely intertwined with the advent of AM processes, as it naturally aligns with this method, enabling the comprehensive utilization of topology optimization benefits [53]. Applying topology optimization to additive manufacturing introduces an unparalleled avenue for design and manufacturing freedom, constituting an effective lightweight methodology. Leveraging the unique advantages of additive manufacturing, such as the realization of intricate spatial arrangements and voxel-by-voxel digitized printing, requires a profound comprehension of the intricate Process-Structure-Property-Performance (PSPP) relationship, as elucidated in the study by Li et al. to which reference will be made [54]. This understanding is pivotal in establishing a quantitative correlation between part properties and various process variables, encompassing laser parameters, processing conditions, and material attributes.

By harnessing data-driven methodologies to explore the PSPP relationships, it becomes feasible to optimize multiple process parameters alongside structural topology. This optimization process can be achieved through employing one of the topology optimization algorithms outlined in Table 2.9. Three scenario-specific optimizations exemplify the effectiveness of this approach, yielding advancements in lightweight performance when contrasted with conventional optimization methods [54].

Figure 2.16, taken from Li et al. work's, provides a schematic overview of the entire topology optimization process tailored for additive manufacturing. Following the delineation of manufacturing process parameters and the establishment of PSPP relationships, the subsequent step involves characterizing the material properties of the structure. Subsequently, topology optimization techniques and algorithms are applied to assess a plethora of potential structural configurations, as elaborated in the preceding section, ultimately culminating in the attainment of the optimal structural design.

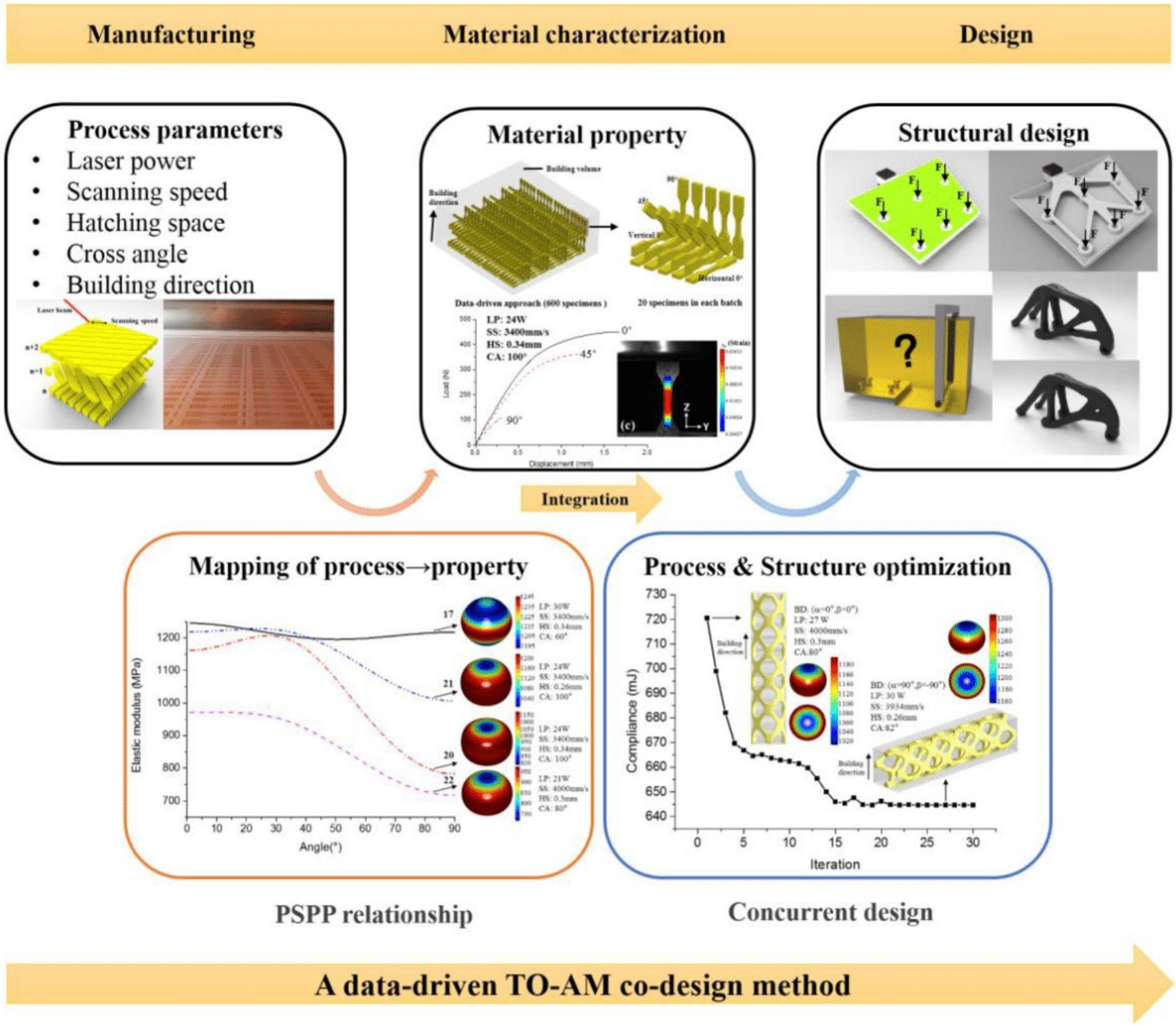

Figure 2.16: Overview of multidisciplinary topology optimization for additive manufacturing [54]

2.4 Genetic Algorithms

A Genetic Algorithm (GA) draws its inspiration from Darwin's theory of natural evolution and serves as a heuristic search approach. This algorithm mirrors the process of natural selection, where the most adept individuals are chosen for reproduction in order to generate the next generation's offspring [55].

The process of natural selection commences by selecting the most adept individuals from a population. These individuals generate progeny that inherit their parents' traits and become part of the subsequent generation. If the parents possess higher fitness, their progeny might outperform them and have an enhanced chance of survival. The population remains of fixed size: as new generations emerge, individuals with lower fitness are removed, creating space for new progeny. The genetic process is recurrently executed to try to produce individuals in each successive generation that surpass the proficiency of the preceding generation. This iterative process continues, ultimately yielding a generation characterized by the most adept individuals [56].

This concept can be extended to address search problems. It involves identifying a subset of the best solutions from a pool of potential solutions.

Usually, genetic algorithms consist of five distinct main phases. Figure 2.17 presents a general flowchart depicting these phases [57].

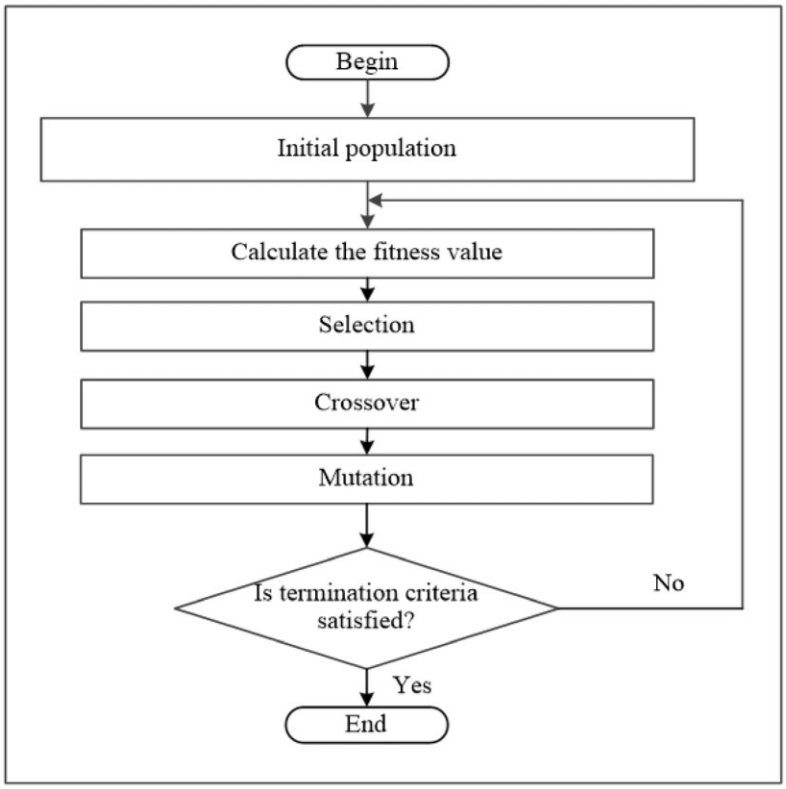

Figure 2.17: Flowchart of a typical genetic algorithm [58]

1. **Initial Population**

   The process commences with a group of individuals, termed a population. Each individual represents a solution to the given problem. An individual is defined by a set of parameters known as genes. These genes are combined into a string to form a chromosome, which represents a solution. In a genetic algorithm, an individual's set of genes is expressed as a string using an alphabet, often employing binary values (a sequence of 1s and 0s). This process is referred to as encoding the genes into a chromosome.

2. **Fitness Function**

   The fitness function gauges an individual's aptness, which reflects its capacity to compete with other individuals. This function assigns a fitness score to each individual, influencing the probability of an individual being selected for reproduction.

3. **Selection**

   During the selection phase, the emphasis lies in choosing the most adept individuals and enabling them to pass on their genes to the subsequent generation. Two pairs of individuals (parents) are selected based on their fitness scores. Individuals with higher fitness scores possess an increased likelihood of being chosen for reproduction.

4. **Crossover**

   Crossover constitutes a pivotal phase within a genetic algorithm. For every pair of parents intended for mating, a random crossover point is chosen from within their respective genes. Offspring are produced through the exchange of genes between parents until the crossover point is reached. These new offspring are introduced into the population. As illustrated in Figure 2.18, it is possible to have either a single or a double crossover point.

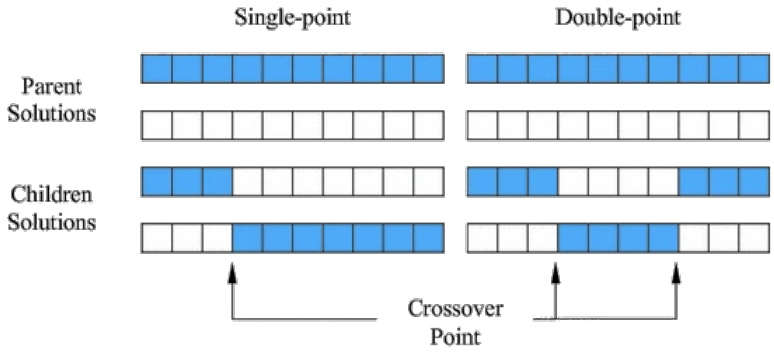

Figure 2.18: Crossover process [57]

5. **Mutation**

   In the formation of new offspring, some of their genes can potentially undergo mutation with a low, random probability. This implies that certain bits within the bit string may be flipped. Mutation is introduced to maintain diversity within the population and thwart premature convergence. This step is depicted in Figure 2.19.

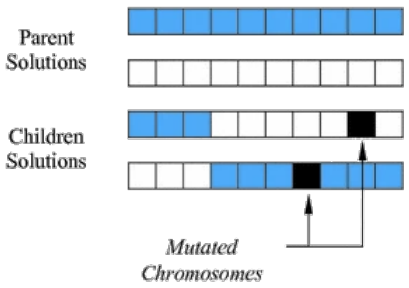

Figure 2.19: Mutation process [57]

The algorithm concludes when the population converges, signifying that it no longer generates offspring that significantly deviate from the previous generation. At this point, the genetic algorithm has provided a set of solutions to the problem.

Chapter 3

Methodology

This chapter presents the heart of this thesis work. All the MATLAB ® codes used for the various types of analysis performed are dealt with and discussed in detail. Starting with the geometry creation and the meshing process, carried out using `PolyMesher`, followed by the structural analysis and an initial topological optimisation phase, implemented using `PolyTop`. Next, the propulsive part is presented, consisting of the regression analysis code, developed from scratch, and the performance analysis, performed using NASA CEA Software. Everything, with the exception of the geometry definition, is implemented within an optimization environement, namely using the `NSGA-II` genetic algorithm, in order to obtain a combined structural and propulsive optimisation. Figure 3.1 portrays the workflow of the MDO methodology developed in this work. It illustrates all the key functions, along with their respective input and output parameters, as well as the data structures used, highlighting their main parameters. Throughout this chapter, the principal data structures utilized by the key functions discussed are presented.

3.1 Model Definition

This first part consists of propellants selection, creation and definition of the geometry, and all the material and propulsive parameters that will form the model under analysis.

The optimization was performed on a two-dimensional domain due to the greater simplicity of modeling and computation, which significantly reduces the computational cost compared to a similar three-dimensional study and allows to the test the developed methodology. However, this approach limits the ability to obtain more complex geometries, as discussed in Section 2.1.4, necessitating additional analyses at another level, such as Computational Fluid Dynamics (CFD) to model the combustion process. To obtain a 3D model, the two-dimensional domain obtained is then extruded, greatly simplifying the printing process in terms of production techniques, support usage, and study.

After the research phase conducted in Chapter 2, especially the reported results [38], the increased availability and ease of printing, the numerous studies conducted by Whitmore et al. [35, 37], and the data available in the work of Yu et al. [59], it was decided to use ABS as the fuel and gaseous oxygen

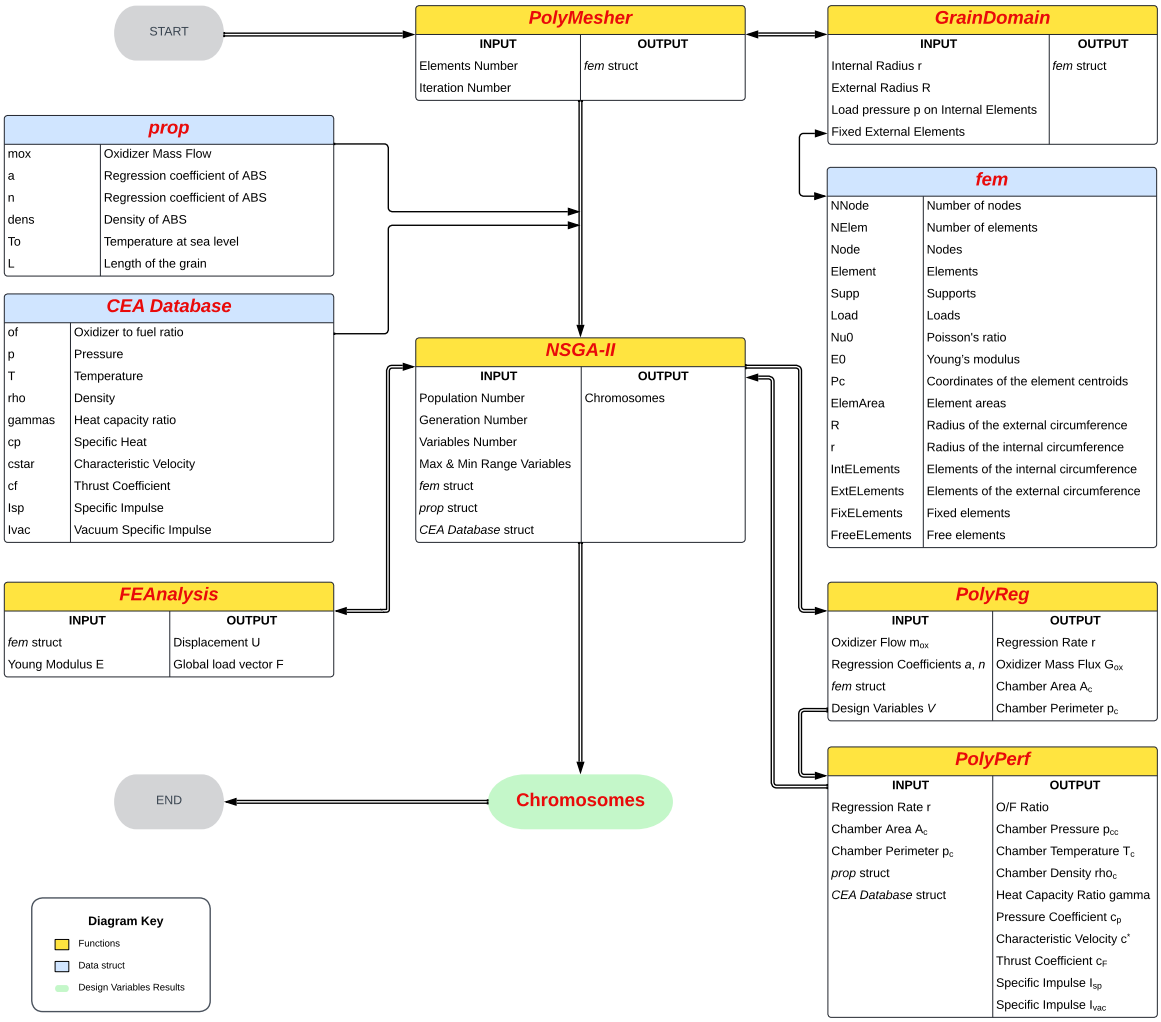

Figure 3.1: Workflow overview highlighting the main functions and data structures utilized

as the oxidizer.

The grain size and propulsive values were chosen taking into account the state of the art and the possibility of combustion tests to evaluate the results obtained. Specifically, the works of Yu et al. [59], Mahjub et al. [60] and McFarland et al. [38] were considered most. Particularly, the regression parameters, introduced in Eq. 2.5, were taken from the work of Yu et al. [59], considering 3D-printed ABS itself. On the other hand, the value of the oxidizer flow was established as a function of the previously established geometrical parameters to obtain results comparable with those present in the state of the art.

Figure 3.2 presents a schematization of the considered domain and Table 3.1 reports all the model parameters, considering the propellants and the geometry, material and propulsion specifications. The propulsion parameters of the model, used by the `PolyReg` and `PolyPerf` functions, are stored within the `prop` data structure as outlined in Table 3.2.

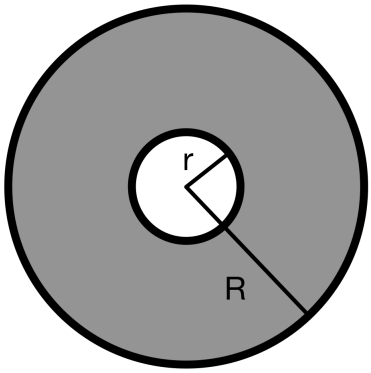

Figure 3.2: Representation of the domain

Table 3.1: Model parameters [59, 61]

Fuel	ABS (Acrylonitrile Butadiene Styrene)	
Oxidizer	O2 Gaseous	
Geometry	**Material**	**Propulsion**
External Radius / Diameter	Young Modulus	Oxidizer Mass Flow
$R = 2.5$ cm / $D = 5$ cm	$E = 2.5$ GPa	$\dot{m}_{ox} = 5$ g/s
Internal Radius / Diameter	Poisson's ratio	Regression coefficient
$r = 0.75$ cm / $d = 1.5$ cm	$\nu = 0.36$	$a = 0.07$
Length	Density	Regression coefficient
$L = 10$ cm	$\rho = 1070$ kg/m^3	$n = 0.442$

Table 3.2: Fields list of the `prop` data structure

`prop` struct	
`prop.mox`	Oxidizer Mass Flow [kg/s]
`prop.a`	Regression coefficient of ABS
`prop.n`	Regression coefficient of ABS
`prop.dens`	Density of ABS [kg/m^3]
`prop.To`	Temperature at sea level [K]
`prop.L`	Length of the grain [m]

3.2 Meshing Process

After selecting and defining the parameters, the next step involved creating the mesh of the model. The MATLAB ® codes `PolyMesher` and `PolyTop` were used for model creation and optimization, respec-

tively [62, 63]. These codes are implemented within the main code, `PolyScript`. The decision to use these codes as a starting point was made for several reasons. Firstly, their versatility in creating meshes for domains with specific geometries makes them particularly suitable, especially when a polygonal mesh is preferred. Additionally, the availability of all the codes and well-drafted documentation made them easily accessible, thanks to the work of Professor Paulino on topology optimization at Princeton University [64, 65]. Furthermore, the codes exhibit simple, efficient, and robust characteristics, further supporting their selection as the starting point for the mesh creation and optimization process.

The Voronoi tessellation implemented within the meshing process allows the use of polygons for domain creation and requires a brief introduction. The Voronoi tessellation starts with a set of *n* distinct points or seeds `P` and creates, for each of these points, sets of other domain points that have a smaller distance to the seed than any other seed. These sets are called Voronoi cells. A notable property in two dimensions is that a bounded Voronoi cell is always a convex polygon. This is because it is formed by the finite intersection of half-planes, each of which is a convex set. To achieve a higher level of regularity, the algorithm focuses on a specific category of Voronoi tessellations known as Centroid Voronoi Tessellation (CVT). In a CVT, each point y coincides with the centroid y_c of its corresponding region. For a variational characterization of a CVT, it is possible to compute an energy functional based on the deviation of each region from its reference seed. By minimizing this energy functional, it is possible to converge to an optimal tessellation. `PolyMesher` implements Lloyd's algorithm to compute CVTs and built more uniform polygonal meshes. This algorithm iteratively replaces the given generating seeds with the centroids of their corresponding Voronoi regions. It can be seen as a descent method for the energy functional [62]. A visualization of the Voronoi tessellation with Lloyd's iteration method is showed in Fig.3.3. For detailed information on Voronoi tessellation, CVT, and Lloyd's algorithm, it is recommended to refer to the sources cited at the beginning of this section and the work by Aurenhammer [62, 66].

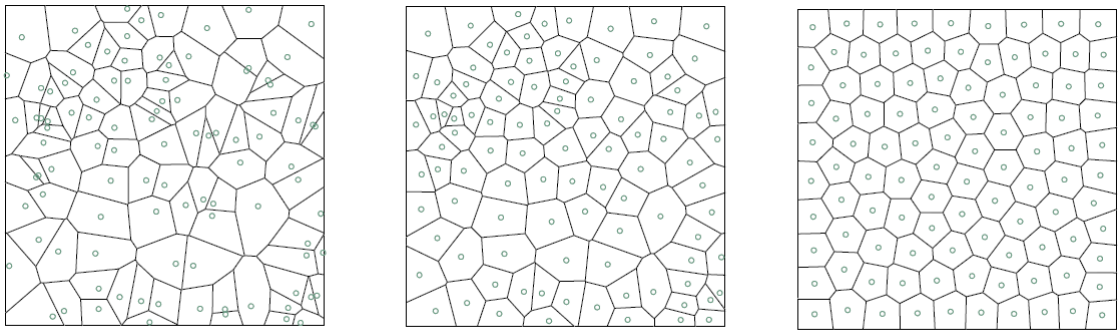

Figure 3.3: Voronoi tessellation with Lloyd's iteration method

The domain is created within the `GrainDomain` function, which is called within the `PolyMesher` function responsible for generating the mesh for the selected domain. The input data for `GrainDomain` includes the inner radius `r` and outer radius `R` of the cylindrical domain, as well as the applied pressure `pc` as a load condition. As for the load and constraint conditions, highlighted in Fig.3.4c, the structure is constrained at the nodes along the outer circumference of the domain, while a radial pressure `pc` of 1 bar is applied at the nodes along the inner circumference of the domain. Regarding the choice of load,

it is important to clarify that this is considered more as an exploratory load rather than an actual load. For this reason, the value used is far from the pressures typically present in combustion chambers. The rationale behind the exploratory load lies in the type of structural optimization being performed. Minimizing compliance leads to the attainment of a design that is superior in terms of structural response and robustness, rather than, for instance, the configuration with the absolute lowest stress levels. Hence, regarding our configuration of geometry and load condition, the optimized design is nearly independent of the imposed load value. Variations in load may result in minor adjustments, such as thickness changes, but the overall design remains unchanged.

The input data for `PolyMesher` are the function containing the domain (`Domain`), the desired number of elements (`NElem`), the maximum number of Lloyd's iterations (`MaxIter`), and optionally, an initial set of seeds (`P`). A double symmetry of the mesh was enforced, as described in Section 6 of "*PolyMesher: a general-purpose mesh generator for polygonal elements written in MATLAB*" [62]. A number of 500 elements were chosen to ensure that each element's area is larger than the average resolution of FDM printing. This precautionary measure helps avoid printing issues or the requirement for subsequent AM filters. Additionally, a higher number of elements was chosen to maximize the number of iterations in the regression analysis. This choice is linked to the nature of the regression code, as described in Section 3.4, where the number of elements is directly proportional to the number of iterations required to complete combustion, thereby yielding more output data. The obtained mesh is reported in Fig.3.4c.

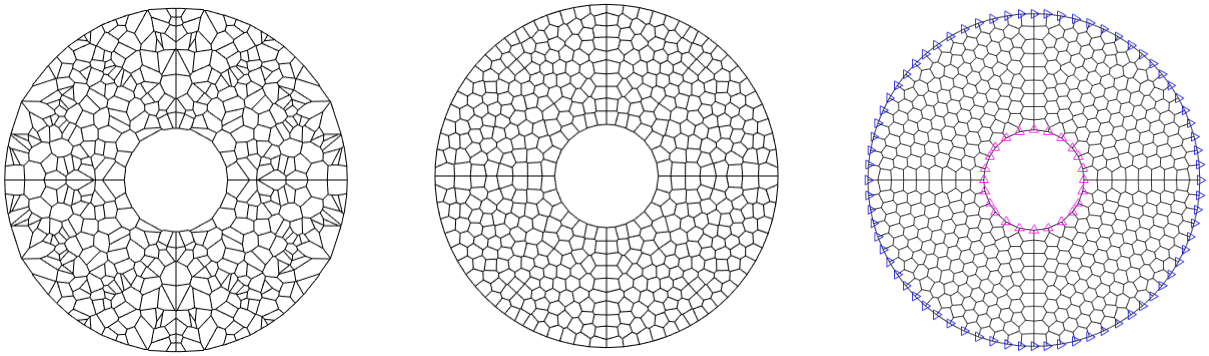

(a) Initial Random Points (b) After 10 Iterations (c) Final Mesh

Figure 3.4: Meshing process with Voronoi tessellation and Lloyd's iteration method

Within `PolyMesher`, several functions are invoked. The `DistFnc` function utilizes the implemented functions `dCircle` and `dDiff` to compose the desired domain. The `BndryCnds` function identifies the nodes belonging to the inner and outer circumferences to apply respective loads and constraints. The `PolyMshr_RndPtSet` function generates a pool of points, equal to the desired number of elements, which will serve as the centers of the polygons tessellating the domain. Table 3.3 provides a comprehensive list of all the functions used by `PolyMesher`.

The data generated during the meshing process as described earlier, along with the results derived from the structural analysis, discussed in the next section, are stored within the `fem` data structure. Table 3.4 presents the data obtained from the meshing process, which is complemented by the information provided in Table 3.6.

Table 3.3: List of functions used by `PolyMesher` [62]

Domain Functions	**Meshing Functions**	
`GrainDomain`	`PolyMshr_RndPtSet`	`PolyMshr_CllpsEdgs`
`DistFnc`	`PolyMshr_Rflct`	`PolyMshr_RsqsNds`
`dCircle`	`PolyMshr_CntrdPly`	`PolyMshr_RbldLists`
`dDiff`	`PolyMshr_ExtrNds`	`PolyMshr_PlotMsh`

Table 3.4: Fields list of the `fem` data obtained by `PolyMesher` [63]

`fem` struct (data from `PolyMesher`)	
`fem.NNode`	Number of nodes
`fem.NElem`	Number of elements
`fem.Node`	[NNode $\times$ 2] array of nodes
`fem.Element`	[NElem $\times$ Var] cell array of elements
`fem.Supp`	[NSupp $\times$ 3] support array
`fem.Load`	[NLoad $\times$ 3] load array
`fem.Nu0`	Poisson's ratio of solid material
`fem.E0`	Young's modulus of solid material
`fem.Pc`*	Coordinates of the centroid of each element
`fem.R`*	Radius of the external circumference [m]
`fem.r`*	Radius of the internal circumference [m]
`fem.IntElements`*	Elements of the internal circumference
`fem.ExtElements`*	Elements of the external circumference
`fem.FixElements`*	Fixed elements (IntElements + ExtElements)
`fem.FreeElements`*	Free elements
`fem.nV`*	Number of variable elements
`fem.Reg`	Tag for regular meshes

* Added fields, not presented in `PolyScript`

3.3 Structural Analysis

The structural analysis is done applying the Finite Element Method (FEM) to calculate the compliance of the entire structure, which is computed as the dot product of forces and displacements of individual nodes [63]. The subsequent goal of the structural optimization is to minimize this parameter, corresponding to the minimization of structural deformations. This objective is pursued to ensure greater structural integrity of the 3D-printed grain, avoiding excessive deformations during combustion and unexpected variations in rocket propulsion parameters and performance.

To perform this analysis, the `FEAnalysis` function within the `PolyTop` code is utilized, and its documentation is referred to for a deeper understanding of the implemented code [63]. `FEAnalysis` enables

FEM analysis of meshes composed by bidimensional polygonal elements. It assembles the stiffness matrix of the entire structure, starting from the stiffness matrix of each polygonal element, and calculates the displacement of each individual node, considering the forces acting on the nodes resulting from the boundary conditions. `FEAnalysis` has been used as an objective function both within `PolyTop` and as a standalone implementation in `NSGA-II`, as showed in Fig.3.1 and will be clearer in the subsequent sections. Therefore, the function takes into account the design variables, namely the volume fraction of each element, in the evaluation of the stiffness value for each element. Table 3.5, depicting the conceptualization of Talischi et al.'s work [63], lists all the functions utilized within `FEAnalysis`, accompanied by a brief description of their main purpose. Table 3.6 presents the data obtained from the structural analysis, which complements the `fem` data structure.

Table 3.5: List of functions used by `FEAnalysis` [63]

Function	Purpose
`TabShapeFnc`	Tabulation of shape functions values and their gradients at the integration points of the reference element with the related quadrature weights.
`PolyShapeFnc`	Computation of the linear shape functions for a reference polygon at an interior point.
`LocalK`	Computation of the local stiffness matrix of the isoparametric polygonal elements.
`PolyTrnglt`	Generation of a directed triangulation of the reference poligon by connecting its vertices to the interior point.
`PolyQuad`	Polygonal quadrature of the reference polygon divided into triangles.
`TryQuad`	Provision of the usual quadrature rule for the reference triangle.
`TryShape`	Provision of the linear shape functions of the reference triangle.

Table 3.6: Fields list of the `fem` data obtained by `FEAnalysis` [63]

`fem` struct (data from `FEAnalysis`)	
`fem.ElemNDof`	Array showing number of DOFs of elements
`fem.ShapeFnc`	Cell array with tabulated shape functions and weights
`fem.k`	Array of local stiffness matrix entries
`fem.i`	Index array for sparse assembly of `fem.k`
`fem.j`	Index array for sparse assembly of `fem.k`
`fem.e`	Array of element IDs corresponding to `fem.k`
`fem.ElemArea`	Array of element areas
`fem.F`	Global load vector
`fem.FreeDofs`	Array of free degrees of freedom

3.4 Regression Analysis

The grain regression analysis has been implemented through the `PolyReg` function, which has been developed from scratch. `PolyReg` simulates the grain regression based on the geometry of the structure (`fem` struct), the design variables V, and the propulsion parameters (`prop` struct), which have been described in Section 3.1 and are listed in Table 3.1. Table 3.7 presents the input and output parameters of the `PolyReg` function and Figure 3.5 illustrates the respective flowchart.

The `PolyReg` function incorporates a while loop that iterates until all the fuel elements in the domain are combusted, that is, when the sum of volume fractions of all domain elements becomes zero. In each iteration, the `Fuel Elements` (solid elements with $V = 1$) and `Chamber Elements` (empty elements with $V = 0$) are initially identified. At this point, calculating the combustion chamber's area A_c becomes straightforward by summing up the areas of the individual elements previously identified. It's important to specify that the area enclosed by the inner circumference of the domain is consistently treated as a component of the combustion chamber, with its area being added to the total.

Consequently, the values for regression rates $\dot{r}$ and oxidizer mass flux G_{ox} are calculated as follows:

$$\dot{r} = a \cdot {G_{ox}}^n \tag{3.1}$$

$$G_{ox} = \frac{\dot{m}_{ox}}{A_c} \tag{3.2}$$

Where a, n are the regression coefficient and $\dot{m}_{ox}$ is the oxidizer mass flow, all reported in Table 3.1.

Table 3.7: Input and output parameters of the `PolyReg` function

INPUT Parameters	**OUTPUT Parameters**
Oxidizer Mass Flow $\dot{m}_{ox}$	Regression Rate $\dot{r}$
Regression Coefficients a, n	Oxidizer Mass Flux G_{ox}
`fem` struct	Chamber Area A_c
Design Variables V	Chamber Perimeter P_c

Subsequently, starting from the identified `Fuel Elements`, those adjoining the combustion chamber are selected, referred to as `Fuel Border Elements`. Taking into consideration the sides of these elements that border the combustion chamber, the perimeter of the chamber is calculated. Finally, all the `Fuel Border Elements` are combusted by setting $V = 0$, allowing progression to the next iteration until the domain's combustion is completed. Each iteration essentially concludes with the combustion of the `Fuel Border Elements`. Therefore, the number of iterations is heavily dependent solely on the quantity of `Fuel Elements` and their positioning relative to the `Chamber Elements`. In this context, temporal dependence during the regression process is not considered. This choice is supported by specific reasons and considerations.

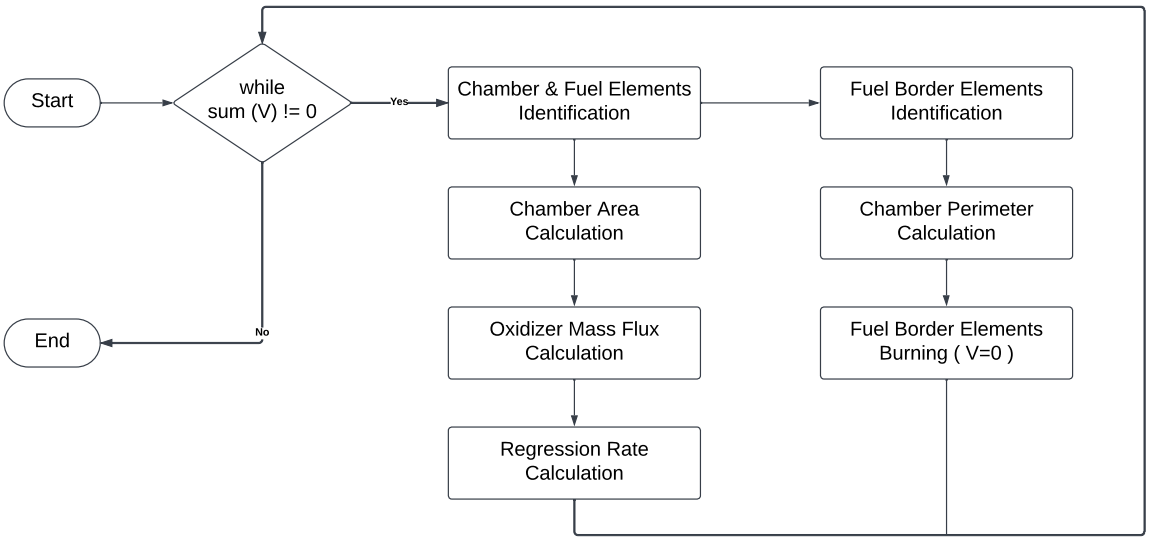

Figure 3.5: PolyReg Flowchart

Initially, an attempt was made to implement temporal dependence by defining a time resolution and considering the regression rate to ascertain whether regression covered the distance between the centers of `Fuel Border Elements` and adjacent `Chamber Elements`, thereby allowing for combustion. However, this approach posed challenges in cases where some `Fuel Elements` failed to combust, leaving them unburned even after numerous iterations, with no correspondence to real-world behavior. Furthermore, this implementation increased the analysis time. The decision to assume uniform and simultaneous combustion of all `Fuel Border Elements` was made by approximating the distance between `Fuel Border Elements` and adjacent `Chamber Elements` as equal across the board, owing to the large number of elements and their small dimensions. This assumption can be considered acceptable and simplified the analysis due to the absence of temporal dependence.

Figure 3.6 illustrates the regression process of the fully solid domain under consideration. The fuel elements are depicted in black, while the voids are represented in white. The gradual combustion of the grain can be observed, commencing from the inner circumference. In this instance, the process is completed within 10 iterations.

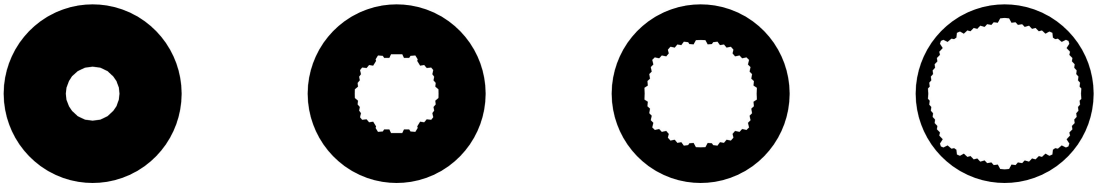

(a) Iteration 0 (b) Iteration 2 (c) Iteration 4 (d) Iteration 7

Figure 3.6: Regression process completed within 10 iterations

3.5 Performance Analysis

The calculation of performance is carried out using the `PolyPerf` function, which is also developed from scratch. `PolyPerf` utilizes a database created using NASA CEA Software [16], relying on chemical equilibrium to conduct a performance analysis. The inputs of this function are the `prop` struct and the `PolyReg` output, i.e. regression rate $\dot{r}$, chamber area A_c and chamber perimeter P_c.

NASA CEA Software is based on the principle that by knowing the chemical equilibrium compositions of a chemical system, it is possible to calculate the theoretical thermodynamic properties of the system. The respective software documentation is referred to [16, 67, 68] for a deeper understanding.

The `PolyPerf` function includes a `for` loop that calculates the propulsion performance for each iteration required for the complete combustion of the grain, performed within the `PolyReg` function. Initially, various propulsive parameters are calculated, including fuel mass flow $\dot{m}_f$, combustion chamber mass flow $\dot{m}_c$, oxidizer to fuel ratio O/F, and combustion chamber pressure p_c, as described by Equations 3.3, 3.4, 3.5 and 3.7 [69], respectively.

$$\dot{m}_f = \dot{r}\ \rho_f\ P_c\ L \tag{3.3}$$

$$\dot{m}_c = \dot{m}_{ox} + \dot{m}_f \tag{3.4}$$

$$O/F = \frac{\dot{m}_{ox}}{\dot{m}_f} \tag{3.5}$$

$$p_0 = \frac{\dot{m}_c}{\zeta_d\ A_t} \sqrt{\frac{T_0\ R}{\gamma} \left(\frac{\gamma+1}{2}\right)^{\frac{\gamma+1}{\gamma-1}}} \tag{3.6}$$

$$p_c = p_0 \left(\frac{T_c}{T_0}\right)^{\frac{\gamma}{\gamma-1}} \tag{3.7}$$

Regarding these presented equations, some specifications need to be made. In Equation 3.3, L represents the length of the grain. Equation 3.6 represents the chamber pressure p_0 assuming an ideal nozzle, where ζ_d denotes the discharge correlation factor (due to cooling, changes in specific heat ratios and incomplete combustion) that is considered to be unity. A_t represents the throat area of the nozzle and is considered equal to the chamber area A_c. Equation 3.7 corrects the previous chamber pressure p_0 calculation using the combustion gas burning rate, obtaining the correct chamber pressure p_c. This assumes an adiabatic expansion with a constant specific heat ratio, which is valid only for small pressure changes [69]. In this equation, T_c represents the chamber temperature, a value provided iteratively by the `CEA Database`. Furthermore, it should be noted that other parameters used as input for the initial iteration include the temperature value $T_0 = 298$ K, the air heat capacity ratio value of $\gamma = 1.4$ (whose values are iteratively updated) and the specific gas constant value of $R = 287$ J/(KgK).

The combustion chamber pressure p_c and the oxidizer to fuel ratio O/F are used as input for the `CEA Database` data structure, from which the corresponding performance values are extracted.

The `CEA Database` was generated utilizing the NASA CEA Software, following the criteria summarized in Table 3.8. `Problem type` settings were configured as "`rocket`", with `Option` defined as "`eq`", implying the assumption of equilibrium composition during expansion. Output data was extracted from the NASA CEA Software, considering a comprehensive array of input pressures p_c ranging from 0.1 (considered instead of 0) to 50 bar, with increments of 1 bar except for the first one. Simultaneously, oxidizer to fuel ratios O/F were varied from 0.5 to 54, in intervals of 0.5, leading to a comprehensive collection comprising 5508 individual cases. It's important to note that due to the discrete nature of the database, the input values were pre-rounded. The intervals were determined following an evaluation of various test analyses, taking into account potential limit values and variations in the results obtained. Furthermore, the aim of these studies is to discover the best designs, so the primary purpose of performance calculations is the comparison between different geometries rather than the calculation itself.

Table 3.8: Settings of the NASA CEA Software for the creation of the `CEA Database` [68]

Problem Type	`rocket`	**Pressure Range**	0.1 - 50 bar	**O/F Range**	0.5 - 54
Option	`eq`	**Pressure Step**	1 bar	**O/F Step**	0.5

The NASA CEA Software enables the calculation of theoretical rocket performance considering either an Infinite-Area Combustion chamber (IAC) [70] or a Finite-Area Combustor (FAC) [71].

This calculation requires the imposition of several assumptions, most of which are similar for both models and are summarized in Table 3.9. In this case, the IAC model has been considered as it is based on reproducing a practical combustion test of the fuel only, without the interference of the nozzle.

Table 3.9: Assumptions of the NASA CEA Software for the rocket performance calculation [67]

One-dimensional form of the continuity, energy and momentum equations
Zero velocity at the combustion chamber inlet
Complete combustion
Adiabatic combustion
Isentropic expansion in the nozzle
Homogeneous mixing
Ideal-gas law
Zero temperature and velocity lags between condensed and gaseous species

The calculation of performance begins with the conservation equations of continuity, momentum, and energy. These are given respectively by Eq. 3.8, 3.9, and 3.10, where they involve the mass flow $\dot{m}$, density ρ, cross-sectional area A, flow velocity u, pressure p, and specific enthalpy h.

$$\dot{m} = \rho \; A \; u = const \tag{3.8}$$

$$p + \rho \; u^2 = const \tag{3.9}$$

$$h + \frac{u^2}{2} = const \tag{3.10}$$

Subsequently, it is possible to calculate the exit flow velocity u_e, as shown in Eq. 3.11, which is valid for the IAC model. Here, the subscripts "inf" and "e" refer to conditions upstream and downstream, respectively. It is noted that velocity is expressed in m/s and enthalpy in J/kg.

$$u_e = \sqrt{2 \; (h_{inf} - h_e)} \tag{3.11}$$

Moving forward, it is possible to compute the thrust F (Eq.3.12), the specific impulse I_{sp} (Eq.3.13), the vacuum specific impulse I_{vac} (Eq.3.14), the characteristic velocity c^* (Eq.3.15), and the thrust coefficient C_F (Eq.3.16).

$$F = \frac{\dot{m} \; u_e}{g_c} + (p_e - p_a) \; A_t = \frac{\dot{m} \; u_e}{g_c} \tag{3.12}$$

$$I_{sp} = \frac{F}{\dot{m}} = \frac{u_e}{g_c} \tag{3.13}$$

$$I_{vac} = I_{sp} + \frac{p_e \; A_e}{\dot{m}} \tag{3.14}$$

$$c^* = \frac{p_{inf} \; A_t \; g_c}{\dot{m}} \tag{3.15}$$

$$C_F = \frac{u}{c^*} \tag{3.16}$$

Clarifications are now provided for the aforementioned equations. g_c is a conversion factor and for the International System assumes a unitary value. The subscript "a" refers to ambient conditions and in this case is assumed to be equal to the exit conditions. The subscript "t" pertains to throat conditions, implying that $A_t = A_e$ since the cross-sectional area remains constant. Equation 3.13 expresses the specific impulse I_{sp} in m/s, although it is more commonly represented in seconds. This conversion is accomplished by utilizing the gravitational acceleration g instead of the conversion factor g_c. Furthermore, it is specified that thrust F is not treated as a direct output from the `CEA Database`. Instead, it is calculated subsequently using Equation 3.12.

For the purpose of schematization, Table 3.10 presents the input and output parameters associated with the `PolyPerf` function. Figure 3.7 depicts the respective flowchart, which also includes all fields of

the `CEA Database` data structure. The outputs obtained from the `PolyPerf` function can be divided into two groups. The first group consists of the characteristics and properties of the combustion chamber, including the oxidizer to fuel ratio O/F, chamber parameters such as pressure p_c, temperature T_c, and density ρ_c, the heat capacity ratio γ, and the specific heat c_p. The second group comprises the propulsion performance parameters, namely characteristic velocity c^*, thrust coefficient C_F, specific impulse I_{sp}, and vacuum specific impulse I_{vac}.

Table 3.10: Input and output parameters of the `PolyPerf` function

INPUT Parameters	**OUTPUT Parameters**	
Regression Rate $\dot{r}$	Oxidizer to Fuel Ratio O/F	Characteristic Velocity c^*
Chamber Area A_c	Chamber Pressure p_c	Thrust F
Chamber Perimeter P_c	Chamber Temperature T_c	Thrust Coefficient C_F
`prop` struct	Chamber Density ρ_c	Specific Impulse I_{sp}
`CEA Database` struct	Heat Capacity Ratio γ	Vacuum Specific Impulse I_{vac}
	Specific Heat c_p	

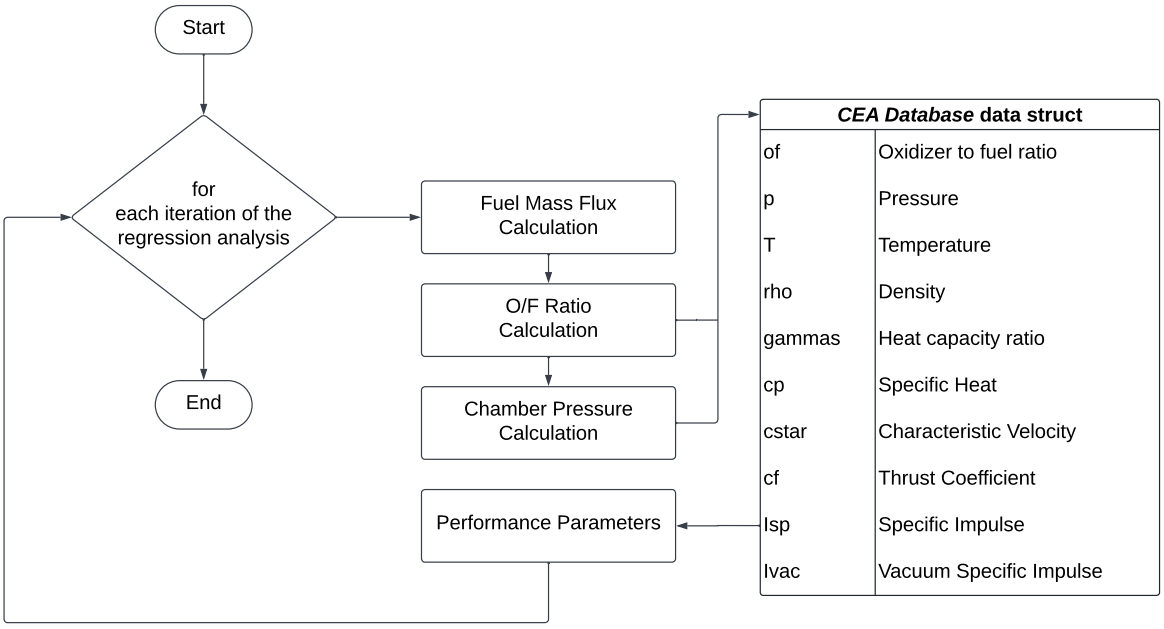

Figure 3.7: `PolyPerf` Flowchart

Finally, the results obtained from the analysis of the full domain carried out with the `PolyPerf` function are presented. The oxidizer to fuel ratio O/F, chamber pressure p_c, chamber temperature T_c, thrust F, thrust coefficient C_F, characteristic velocity c^*, specific impulse I_{sp}, and vacuum specific impulse I_{vac} are reported respectively from Figure 3.8 to 3.15. Each graph displays the iterations performed for the combustion, equal for all cases, on the abscissa. On the ordinate, the output value is plotted along with its respective unit of measurement, expressed in the graph's title.

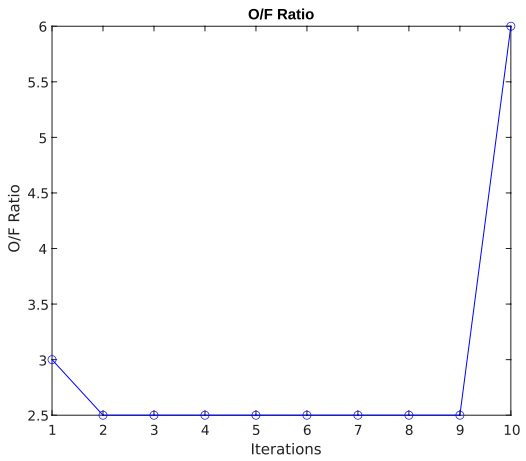

Figure 3.8: Oxidizer to fuel ratio O/F

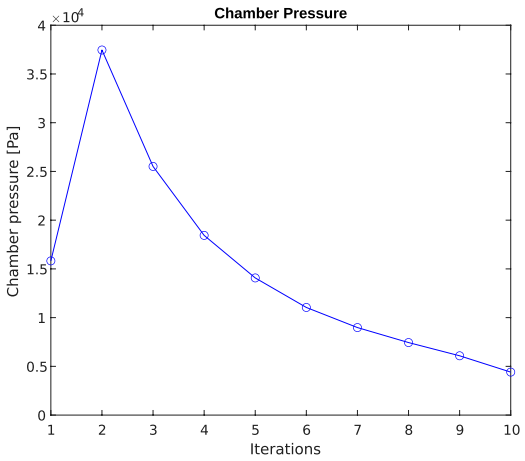

Figure 3.9: Chamber pressure p_c

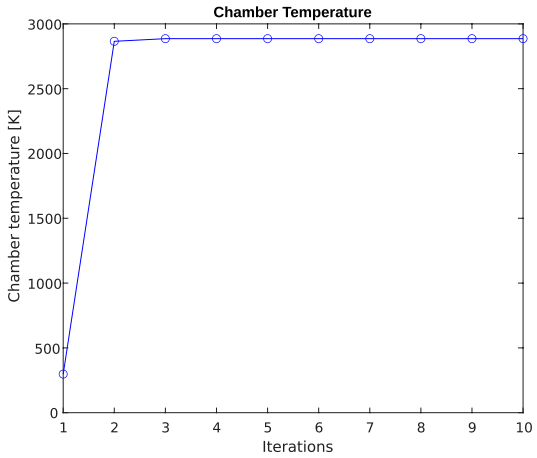

Figure 3.10: Chamber temperature T_c

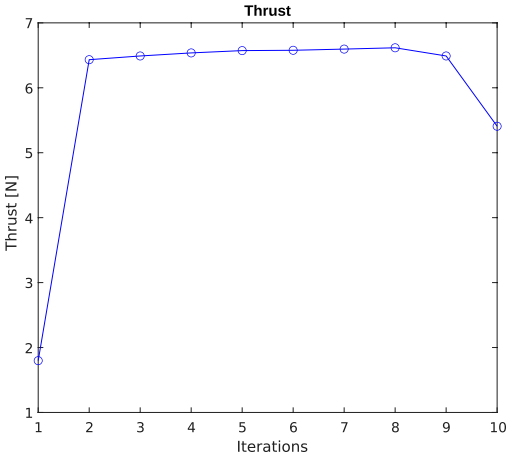

Figure 3.11: Thrust F

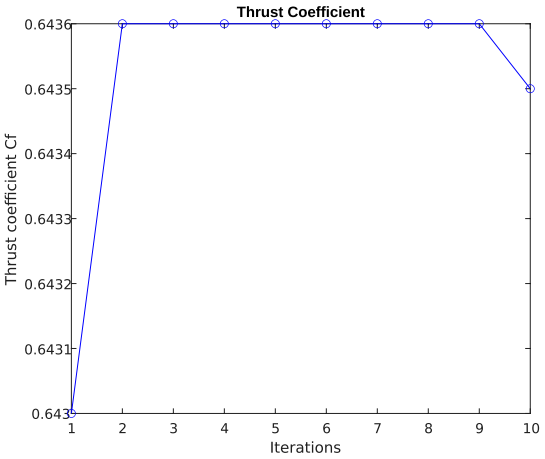

Figure 3.12: Thrust coefficient C_F

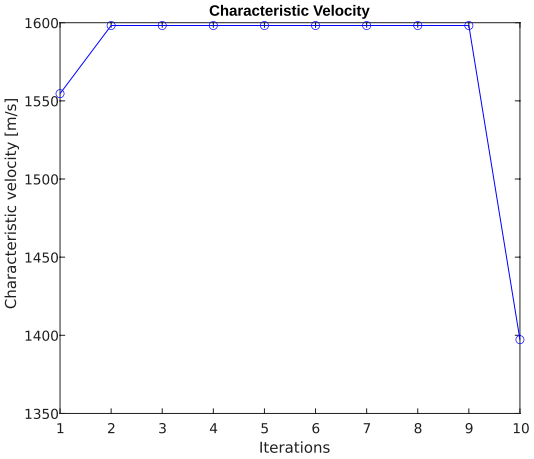

Figure 3.13: Characteristic velocity c^*

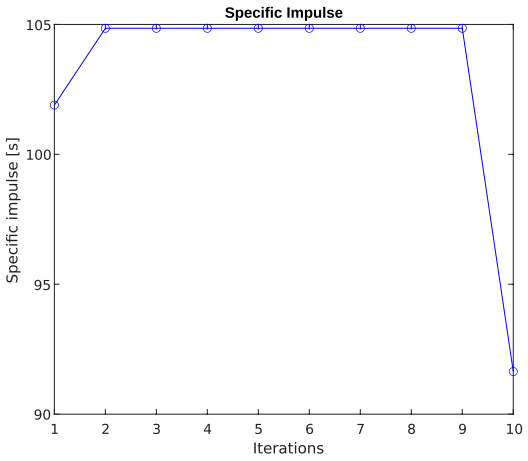

Figure 3.14: Specific impulse I_{sp}

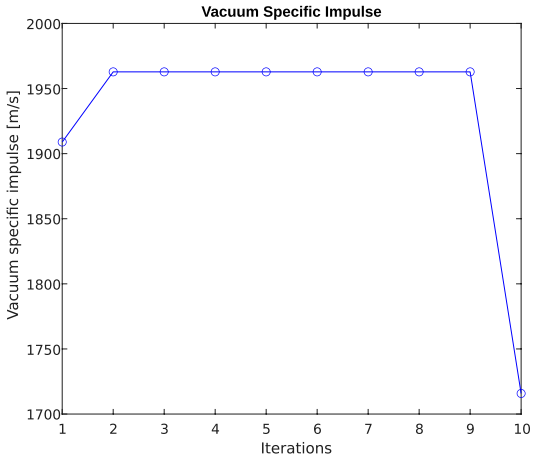

Figure 3.15: Vacuum specific impulse I_{vac}

It can be observed that practically all parameters exhibit a substantial increase following the initial iteration, attributed to the commencement of combustion, followed by a stable phase, and subsequently, a more or less pronounced decrease during the final iteration, marking the culmination of combustion. Only the oxidizer to fuel ratio O/F demonstrates an inverse behavior, owing to its fuel flow component in the denominator (Eq.3.5), which tends to approach zero at the conclusion of combustion. These parameter behaviors align with physical plausibility.

3.6 Topology Optimization

As mentioned in Section 3.2, in the early part of this work, the `PolyTop` function implemented in the `PolyScript` code, along with `PolyMesher`, was used. `PolyTop` performs the topological optimization of the domain generated by `PolyMesher` by implementing the Optimality-Criteria Algorithm (OC) using the SIMP Method [63]. In the later part of this work, it was replaced by `NSGA-II` to leverage the characteristics of genetic algorithms for multidisciplinary optimization of the structural and propulsion aspects, as explained in the next section. This could not be implemented in `PolyTop` due to the lack of sensitivities regarding the propulsion part, as there are no explicit connections with the geometry.

`PolyTop` internally uses numerous functions and, again, reference is made to the respective documentation for in-depth understanding [63]. Table 3.11, depicting the conceptualization of Talischi et al.'s work [63], lists all the functions utilized within `PolyTop`, accompanied by a brief description of their main purpose. Input and output parameters of the function are presented in Table 3.12. The inputs are the geometric and structural parameters, contained in the `fem` struct, and the optimization parameters, contained in the `opt` struct and described in Table 3.13.

Table 3.11: List of functions used by `PolyTop` [63]

Function	Purpose
`ObjectiveFnc`	Computation of the objective function of the optimization problem.
`FEAnalysis`	Structural analysis necessary for the objective function.
`ConstraintFnc`	Computation of the constraint function of the optimization problem.
`UpdateScheme`	Computation of the design variable changes through the implementation of the bisection method, by knowing the gradients of the objective and constraint function, the design variables values and the constraint function.

Table 3.12: Input and output parameters of the `PolyTop` function [62]

INPUT	OUTPUT
Design Variables Bounders	Optimized Design Variables
Volume Fraction Constraint	
Maximum Iteration Number	
Initial Design Variables	

Table 3.13: Fields list of the `opt` data structures [63]

`opt` struct	
`opt.zMin`	Lower bound for design variables
`opt.zMax`	Upper bound for design variables
`opt.zIni`	Initial array of design variables
`opt.MatIntFnc`	Handle to material interpolation function
`opt.P`	Matrix that maps design to element variables
`opt.VolFrac`	Specified volume fraction constraint
`opt.Tol`	Convergence tolerance on design variables
`opt.MaxIter`	Max. number of optimization iterations
`opt.OCMove`	Allowable move step in the OC update scheme
`opt.OCEta`	Exponent used in the OC update scheme

The design variables considered are the volume fractions of each `Free Elements` of the domain. The `Free Elements` are defined as all elements within the domain to which no loads or constraints are applied, i.e., all elements except those forming the boundary of the inner and outer circumferences (`Int Elements` and `Out Elements`). The constraint function is formed by the volume fraction, which represents the percentage of final domain area compared to the initial area. The default objective function

is compliance, addressed in Section 3.3, which is minimized until convergence is reached. As already explained in Section 3.2 regarding the load condition, the minimization of compliance is pursued with the aim of achieving the best possible design in terms of robustness and structural response. For example, structural integrity is not guaranteed as stress analysis is not conducted. This latter analysis could be easily implemented later but was not deemed of primary importance in this initial phase, especially considering the grain's purpose, which is to be combusted.

The output of `PolyTop` consists of the optimal values of the design variables, considering the imposed parameters. Figure 3.16 shows an example of a general topology optimization, performed with an 80% volume fraction constraint.

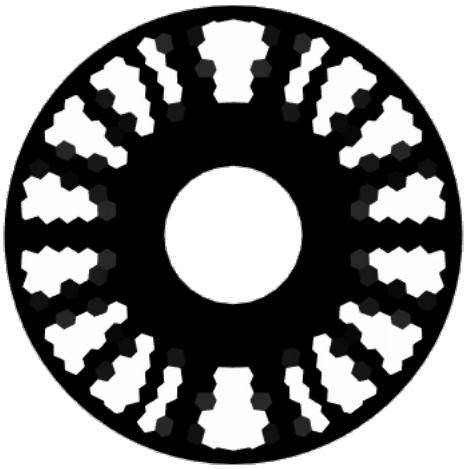

Figure 3.16: Optimized domain with 80% Volume Fraction constraint

3.7 Multidisciplinary Design Optimization

MDO was implemented using the `NSGA-II` algorithm [72]. The choice of the optimizer fell on genetic algorithms due to the difficulty in computing sensitivities. Genetic algorithms, with their strong numerical nature, can be helpful in cases where the gradient of the objective function is unknown. The only obstacle in this case is the large number of variables, specifically the 404 free elements in the considered mesh, which led to high computational costs and long execution times.

`NSGA-II` is a non-domination based genetic algorithm for multi-objective optimization, and its documentation is referred to [72] for a complete understanding of the code. Table 3.14, depicting the conceptualization of Seshadri's work [72], enumerates and provides basic descriptions for all the primary steps comprising the `NSGA-II` algorithm.

In the algorithm, two objective functions are set, namely compliance and specific impulse I_{sp}. There are 404 design variables with lower and upper limits set to 0 and 1, respectively. In order to perform the structural analysis, zeros are considered as very small values (1e-4) within `FEAnalysis`.

Table 3.14: Main steps of the `NSGA-II` genetic algorithm [72]

NSGA-II Steps	
Population Initialization	Generating an initial population while taking into account the limits and constraints of the analyzed problem.
Non-Dominated Sort	The population is sorted using the non-domination sort algorithm, which ranks the population based on the best values of objective solutions.
Crowding Distance	Each element in the population is assigned a crowding distance to encourage diversity. The crowding distance represents the density of solutions around a particular solution type. This occurs because subsets of solutions of the same type are formed, resulting in significant similarities.
Selection	Individuals are selected based on their rank and crowding distance. This selection is specifically carried out through a binary tournament with a crowd-comparison operator.
Genetic Operators	Genetic operators are applied to generate new individuals. Specifically, the Simulated Binary Crossover [73, 74] and Polynomial Mutation [74, 75] operators are employed.
Recombination and Selection	The offspring population is merged with the existing population of the current generation. A selection process is executed to determine the individuals for the subsequent generation. This approach guarantees elitism by incorporating the best individuals from both the current and previous generations.

Input and output parameters of the function are presented in Table 3.15. The main genetic parameters include the population size (`pop`) and the number of generations (`gen`), which determine the size of the initial pool of chromosomes and the number of crossbreeding iterations between chromosome families. Initially, analyses were conducted with $pop = 1000$, which is an order of magnitude larger than the number of design variables, and $gen = 100$, which is the same order of magnitude as the number of design variables. This principle is considered as a rule of thumb and was taken as a starting point, considering a substantial pool relative to the problem at hand. We were aware that further evaluations would be made depending on the results and the required analysis times of the initial tests [76].

Table 3.15: Input and output parameters of the `NSGA-II` function

INPUT	**OUTPUT**
Population number `pop`	Chromosomes
Generation number `gen`	
`fem` struct	
`prop` struct	
`CEA Database` struct	

Figure 3.1 in the beginning of this chapter depicts the complete workflow of the main multidisciplinary optimization performed. It includes all the functions used, along with their input and output parameters, as well as all the data structs utilized, highlighting their key parameters. It can be observed that the workflow begins with the model definition, involving the construction of the `fem` struct using the `GrainDomain` and `PolyMesher` functions. The core of the process is represented by the `NSGA-II` genetic algorithm, which takes all the data structures (`fem`, `prop`, `CEA Database`) as input. `NSGA-II` invokes the `FEAnalysis` function to compute the structural objective function and the `PolyReg` and `PolyPerf` functions in sequence to calculate the propulsion objective function. At the end of the analysis, the chromosomes are obtained, representing the set of design variables for each population family along with their respective objective function values. These chromosomes are then used to form the Pareto front of the obtained solutions, which represents their visualization on a graph with the two considered objective functions as the horizontal and vertical axes. These will be presented as outcomes in the following chapter.

Chapter 4

Results

This chapter presents the results obtained from the conducted analyses. Utilizing the methodology explained in the preceding chapter, a range of analytical investigations was carried out. The model under consideration is the one described in the previous chapter, with its parameters listed in Table 3.1 and its mesh visualized in Figure 3.4c. The initial investigation, focused on regression analysis, was undertaken to validate the effectiveness of the developed code concerning propulsion aspects. Subsequent sections reveal distinct analyses conducted to optimize the structural and propulsion characteristics of the examined grain. Concluding the presentation, the chapter introduces a comprehensive multidisciplinary design optimization that integrates both structural and propulsion objectives. Initially, the domain is considered as a whole, as previously presented, allowing for complete optimization freedom. Subsequently, a double symmetry was enforced by dividing the domain into quarters and mirroring them. Finally, this same double symmetry case is considered again, but a different fuel is used for comparison purposes, aimed at reducing environmental impact.

4.1 Regression Analysis Results

To validate the regression analysis performed using the `PolyReg` function, a combustion test simulation was conducted for which experimental results were known. The geometric and propulsive conditions reported by Yu et al. [59] were recreated, and the regression coefficients mentioned in Section 3.1 and Table 3.1 were used. The grain considered has a cylindrical type with $R = 8$ mm and $r = 2.3$ mm. Fuel and oxidizer were consistently considered as ABS and pure GOx, respectively. Specifically, the regression coefficients for printed ABS with 100% packing density were considered.

Figure 4.1 presents the data obtained using the `PolyReg` function alongside the experimental data reported in the work of Yu et al. [59], regarding the printed ABS with 100% packing density and solid ABS. Specifically, Figure 4.1a presents the results in a linear scale, while Figure 4.1b depicts them in a logarithmic scale. The latter is employed for a comparison with Figure 2.3, illustrating the theoretical regression rate trend. It is observed that a linear trend is obtained, as expected from theory, represented by a sample function in green, within the region of modeled turbulent heat transfer. Regarding

the comparison with experimental data, it is noticeable that the regression rate trends are completely overlapping with the experimentally obtained ones, indicating the effectiveness of the developed code. Furthermore, it is noticeable that the regression rate of printed ABS is higher than that of solid ABS, and for a detailed understanding of this phenomenon, reference is made to the aforementioned paper [59].

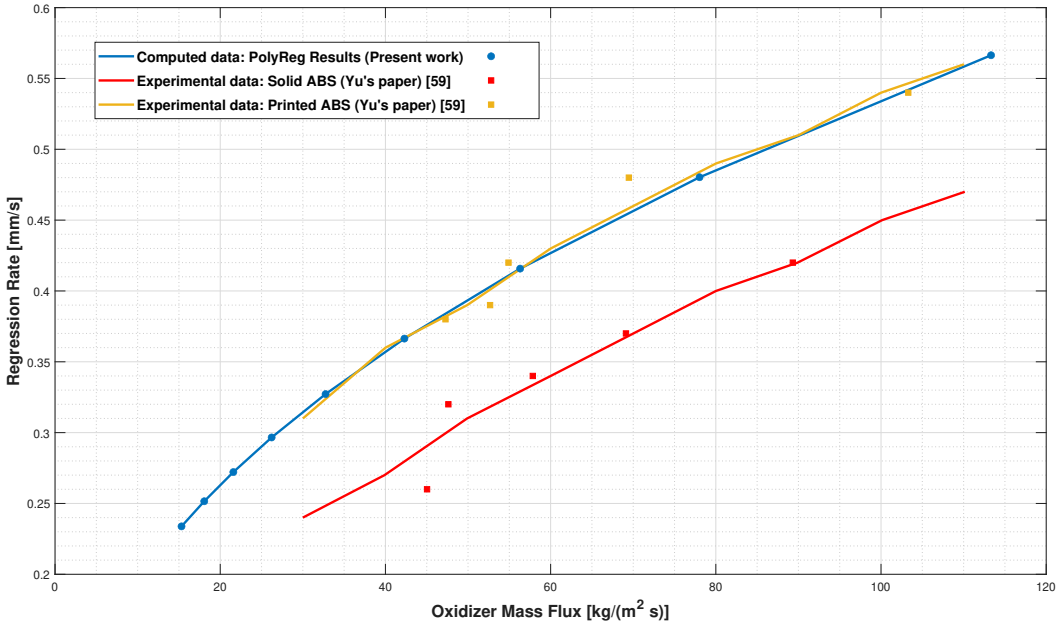

(a) Linear scale

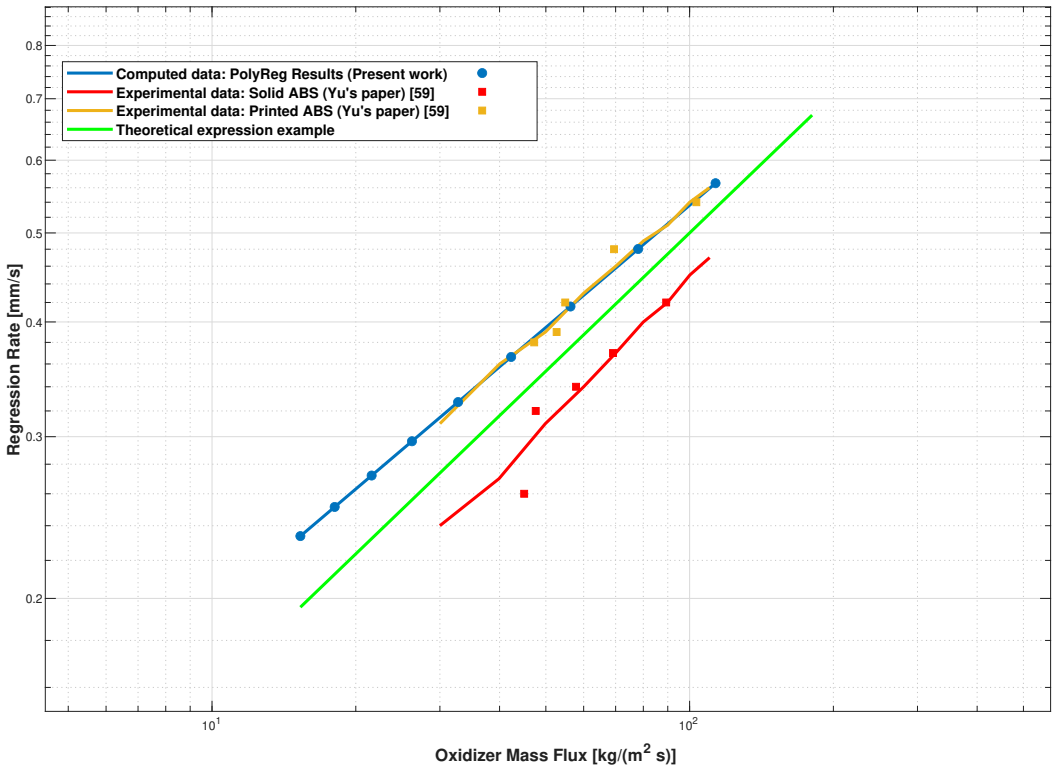

(b) Logarithmic scale

Figure 4.1: Comparison of regression rate values obtained experimentally [59] and by the `PolyReg` code

4.2 Structural Optimization Results

The structural topology optimization was conducted utilizing the `PolyTop` code. As expounded upon in Section 3.3, the structural analysis function extracted from this code was subsequently integrated into the `NSGA-II` framework to enable multidisciplinary optimization. Consequently, dedicated topological optimizations were performed solely at the structural level. The objective entailed minimizing compliance, employing the well-defined model, mesh, and parameters expounded upon earlier. Varied constraint parameters were considered, specifically the volume fraction of the desired structure in relation to the initially defined solid design, enabling the exploration of potential design configurations.

Figure 4.2 presents the designs obtained through topological optimization, wherein the volume fraction constraint parameters were systematically varied, spanning from 50% to 80%. Table 4.1 displays the compliance values corresponding to their respective analyses. Considering the boundary conditions encompassing constraints and loads, the achieved solutions align consistently with expected ones. The domain's volume is curtailed by selectively removing elements positioned within the limits delineated by the inner and outer circumferences, both of which are prescribed. The propagation of stresses is facilitated through radial arrays of elements, resulting in configurations reminiscent of the classical "wagon wheel" design, which finds notable applicability in the domain of rocket fuel grain design. Furthermore, a progressive thickening of the "rays" of the domain can be observed as the total volume fraction increases.

Table 4.1: Structural optimization results

Volume Fraction	**Compliance**	**Figure**
50%	$2.54 \cdot 10^{-3}$	Figure 4.2a
60%	$2.17 \cdot 10^{-3}$	Figure 4.2b
70%	$1.93 \cdot 10^{-3}$	Figure 4.2c
80%	$1.74 \cdot 10^{-3}$	Figure 4.2d

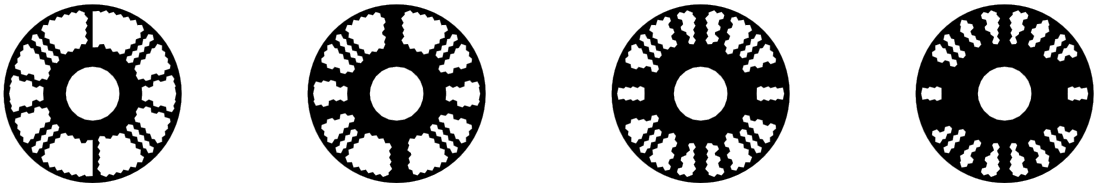

(a) 50% Volume Fraction (b) 60% Volume Fraction (c) 70% Volume Fraction (d) 80% Volume Fraction

Figure 4.2: Structural optimized designs with varying volume fraction constraint values

4.3 Propulsive Optimization Results

Propulsive optimization was carried out using genetic algorithms, employing the MATLAB ® ga algorithm [77]. This choise was needed, as previously indicated in Chapter 3, due to the challenges in sensitivity computation within the propulsive field. The ga software employs genetic algorithm techniques for the minimization of a single objective function. Consequently, in the context of multidisciplinary optimization, a transition was made to the NSGA-II algorithm. The decision was made not to introduce a dedicated section for this algorithm in the methodology chapter, as it follows the same foundations of the introduced NSGA-II. The significant distinctions from the latter lie in the exclusive consideration of variables with binary values and a single objective, thereby decreasing the required computational time.

Several optimization runs were conducted with the objective of maximizing the specific impulse I_{sp}. These analyses utilized predefined genetic parameters within the ga algorithm. Specifically, each analysis featured 100 populations and a maximum number of generations determined by the number of variables. However, it's important to note that this maximum generation limit might not always be reached, especially if the solutions obtained converge early. To ensure robustness, multiple analyses were performed, consistently yielding the same results, thus affirming their validity, which are reported herein.

The top-performing designs are depicted in Figure 4.3, and their corresponding outcomes are detailed in Table 4.2. Notably, the optimum I_{sp} value is attained by the hollow configuration, possibly due to the minimization of the grain mass and the maximization of the exposed grain surface area. The next five superior results consist of both solid-domain configurations and those featuring void elements, though without a clearly discernible geometric pattern.

Table 4.2: Propulsive optimization results

Design	$\mathbf{I_{sp}}$	**Figure**
1	$112.25\ s$	Figure 4.3a
2	$103.24\ s$	Figure 4.3b
3	$102.34\ s$	Figure 4.3c
4	$102.21\ s$	Figure 4.3d
5	$102.21\ s$	Figure 4.3e
6	$102.21\ s$	Figure 4.3f

All remaining designs exhibit specific impulse values oscillating between 90 and 100 s, translating to a maximum variation of 18% from the peak value. The overall findings from the various analyses suggest that the optimization algorithm did not discern a distinct correlation between specific impulse and grain geometry, i.e., no specific geometric form was identified to pursue.

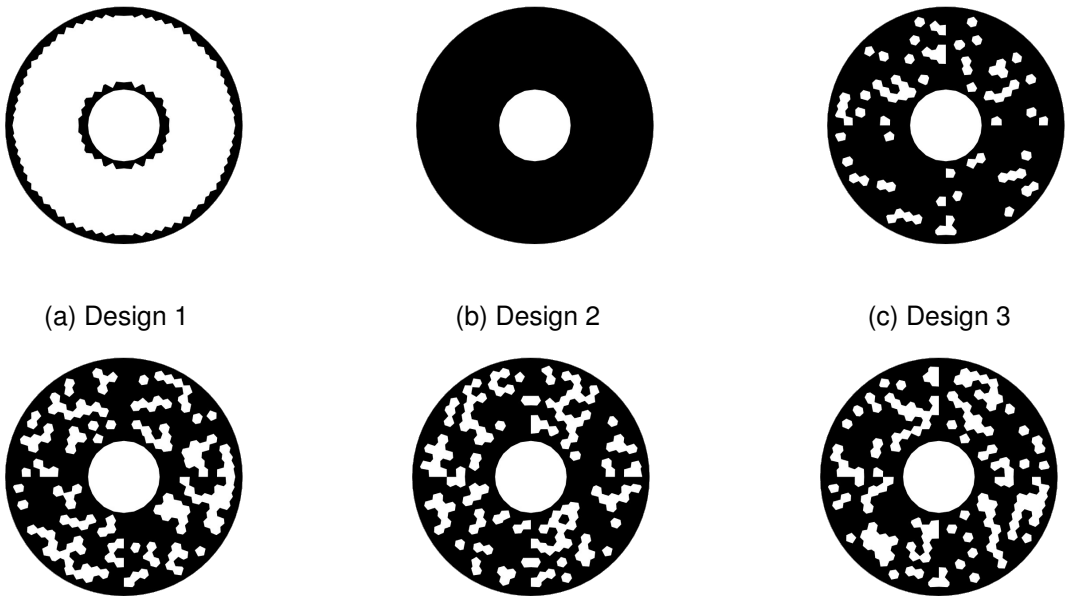

(a) Design 1 (b) Design 2 (c) Design 3

(d) Design 4 (e) Design 5 (f) Design 6

Figure 4.3: Propulsive optimized designs

Subsequently, the next step involved combining the two optimization approaches, structural and propulsive, thereby conducting multidisciplinary optimization. In this regard, the aim was to leverage the strong geometric correlation derived from the structural optimization, upon which to anchor the propulsive optimization characterized by a relatively weaker geometric connection.

4.4 Multidisciplinary Design Optimization Results

Several multidisciplinary design optimizations were conducted with the aim of optimizing both structural and propulsive objectives, achieving the simultaneous minimization of compliance and maximization of specific impulse I_{sp}. The same mesh, as previously shown, was used to allow for comparisons between different analyses. In this instance, two distinct cases were considered separately. The first case involves the original domain, as previously illustrated, wherein optimization enjoys maximal freedom. The second case entails the imposition of double symmetry even during the optimization phase. Various genetic parameters were tested to obtain the best possible analyses, balancing both the quality of the results and the predicted simulation times.

4.4.1 Simple Domain

Initially, the previously presented initial domain was taken into consideration, composed of 404 variables as explained in Section 3.7. Table 4.3 presents the key data of the three main performed analyses, which yielded the best results, including the initial genetic parameters, the values of the objective functions, and the corresponding figure for each analysis. The expected Pareto front line, considering the optimization type, is showed in Figure 4.4. Figures 4.5, 4.7 and 4.9 depict the Pareto front of the performed analyses. All the figures show the obtained solutions plotted in blue on a graph with compliance on the horizontal axis and specific impulse on the vertical axis. Figures 4.6, 4.8, and 4.10 portray the output designs of the top three solutions obtained from the conducted analyses.

Table 4.3: Multidisciplinary optimization results

Analysis	Population	Generation	$\mathbf{I_{sp_{max}}}$	$\mathbf{Compliance_{min}}$	Pareto Front	Designs
1	1000	100	$100.3\ s$	$3.8 \cdot 10^{-3}$	Figure 4.5	Figure 4.6
2	2000	50	$98.5\ s$	$4.2 \cdot 10^{-3}$	Figure 4.7	Figure 4.8
3	2000	90	$100.3\ s$	$3.2 \cdot 10^{-3}$	Figure 4.9	Figure 4.10

Upon analyzing the obtained Pareto fronts resulting from the multidisciplinary design optimizations, it becomes evident that the values of the objective functions are significantly influenced by the initial population. While the Pareto fronts generally exhibit the expected behaviour, it is important to underline that a considerable portion of the obtained chromosomes still hold a rank higher than 1, indicating that the solutions have not yet fully converged. This is expected due to the high-dimensionality of the problem, with numerous design variables and complex interactions. Regarding the obtained designs, it is evident that a discernible geometric pattern has not been achieved as for the propulsion optimization case. The results of all three analyses have yielded configurations marked by noticeable randomness, exhibiting similarities among them while lacking practical implementability due to the presence of disconnected fuel elements and highly fragmented patterns within the geometry.

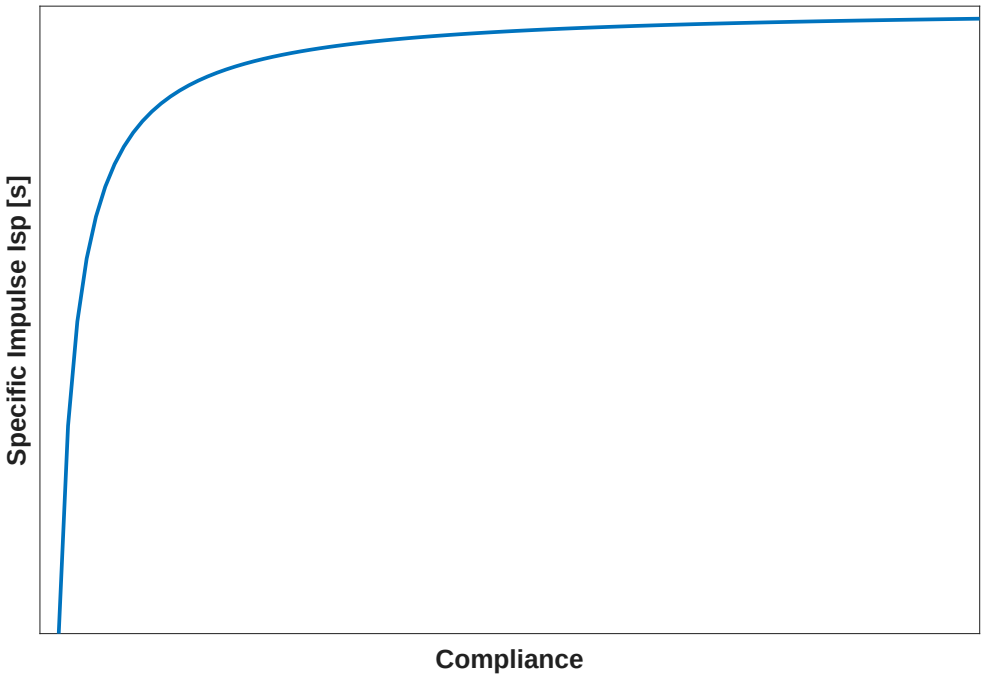

Figure 4.4: Expected trend line of the Pareto front for the conducted analyses

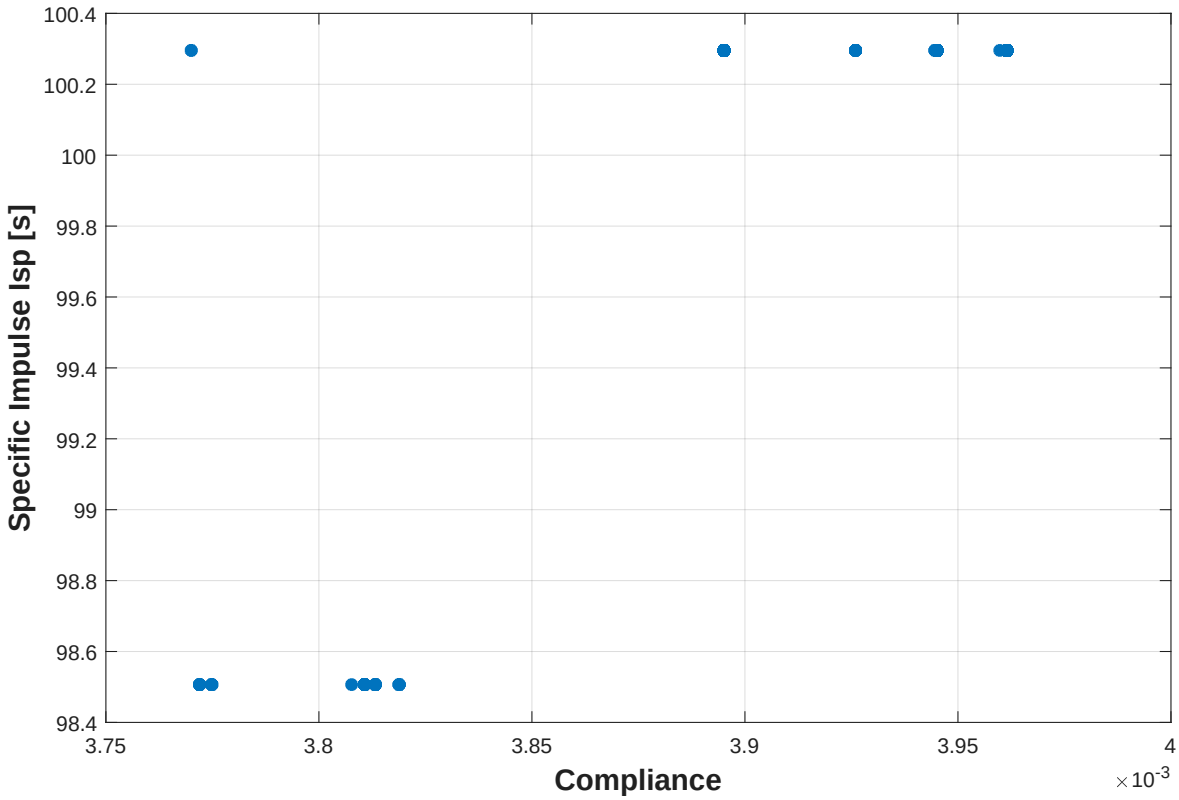

Figure 4.5: Pareto front of the MDO analysis 1

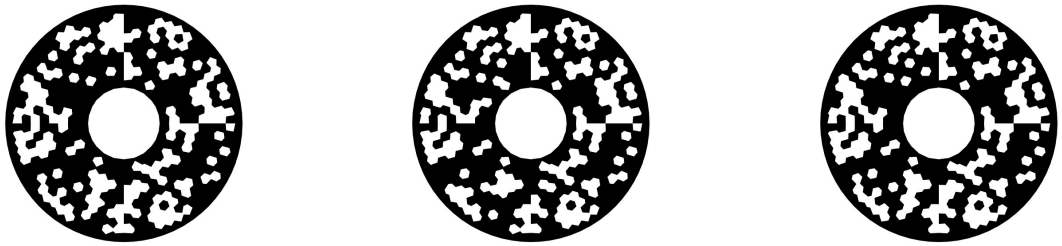

(a) Design 1 (b) Design 2 (c) Design 3

Figure 4.6: Multidisciplinary optimized designs of the analysis 1

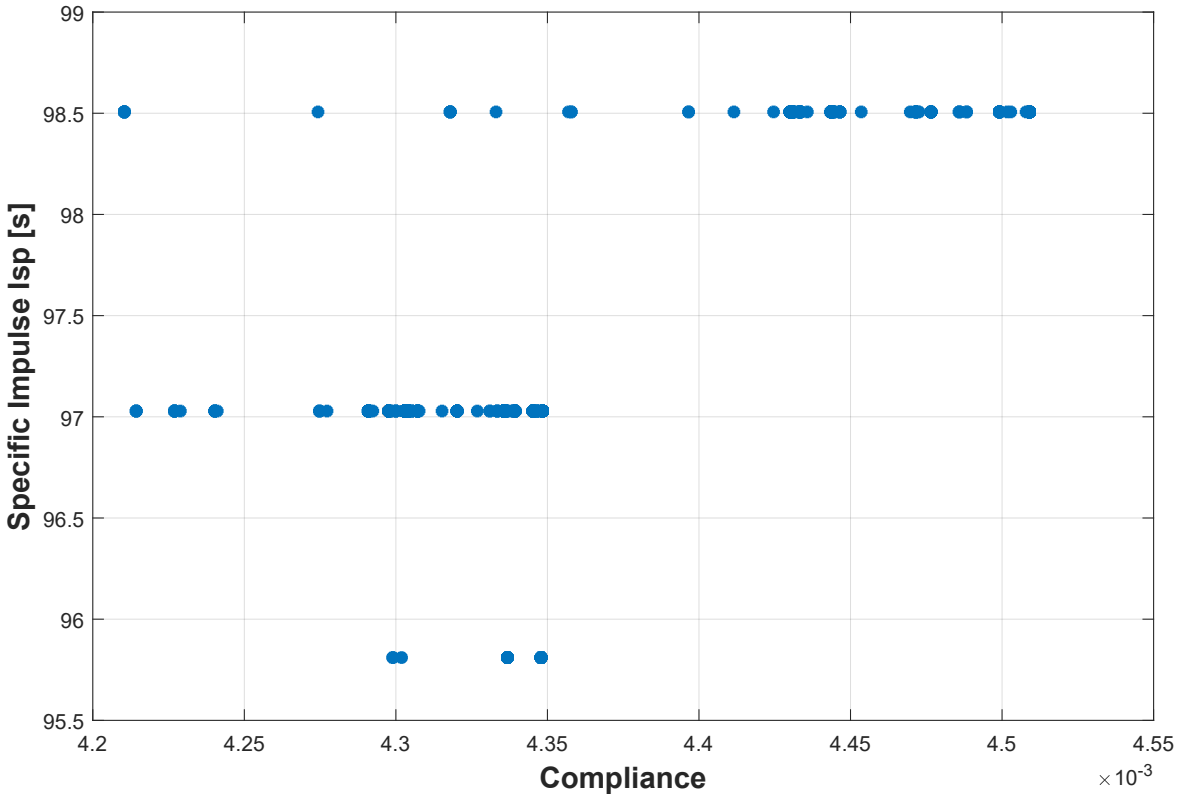

Figure 4.7: Pareto front of the MDO analysis 2

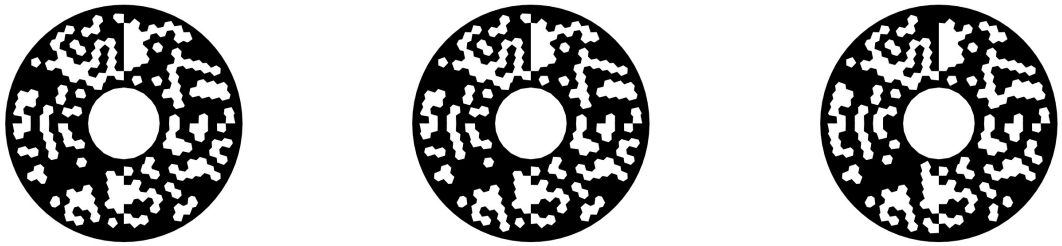

(a) Design 1 (b) Design 2 (c) Design 3

Figure 4.8: Multidisciplinary optimized designs of the analysis 2

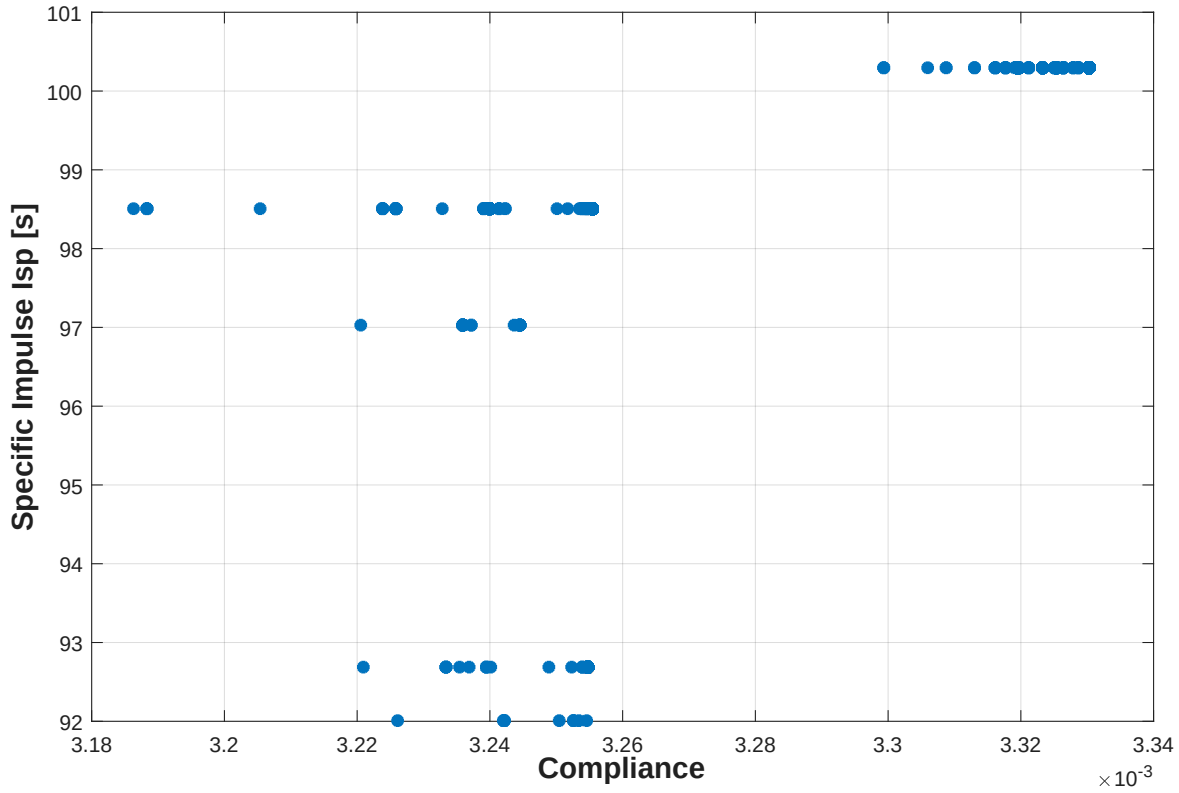

Figure 4.9: Pareto front of the MDO analysis 3

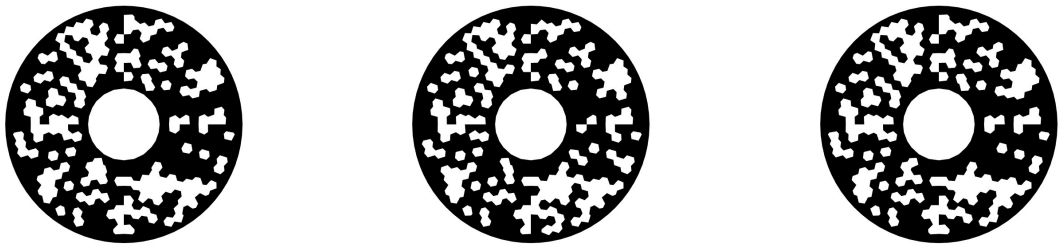

(a) Design 1 (b) Design 2 (c) Design 3

Figure 4.10: Multidisciplinary optimized designs of the analysis 3

4.4.2 Double Symmetry Domain

Subsequently, other analyses were conducted by imposing double symmetry within the optimization process. To achieve this, all the free elements in the first quadrant were initially identified, these are the ones with both center coordinates positive. The volume fractions corresponding to these selected elements became the new variables for the optimization problem. This transition reduced the number of variables from 404 to 101, representing a reduction of 75%. Subsequently, all the mirrored elements in the remaining three quadrants were paired with those in the first quadrant. Finally, to enforce the double symmetry, it was sufficient to replicate the values of the 101 variables (i.e., the elements in the first quadrant) for their corresponding mirrored elements in the other quadrants.

In this case, several analyses were conducted considering various genetic parameters. These parameters were initially selected based on those considered in the previous section and adjusted progressively in these new optimizations to expedite the process. Overall, populations of 1000 or 2000 elements were considered with the number of generations ranging from 20 to 100.

Table 4.4 presents the results of the main analyses with the imposition of double symmetry. Three analyses are reported, each of which includes three different designs. These designs are denoted starting with S1.1, where "S" indicates that these are the symmetric analyses, and the two numbers separated by a period refer to the analysis number and the design number within that analysis, respectively. The choice to present only the best analysis results together, unlike what was done previously, is due to the fact that this time, multiple analyses with different genetic parameters led to the same designs already present in these three analyses. This further underscores the quality of the solutions found.

Table 4.4: Multidisciplinary optimization results of the double symmetry domain

Designs	$\mathbf{I_{sp}}$	$\mathbf{Compliance}$	**Figure**
S1.1	102.2 s	$3.1 \cdot 10^{-3}$	Figure 4.12a
S1.2	100.3 s	$3.0 \cdot 10^{-3}$	Figure 4.12b
S1.3	95.8 s	$2.9 \cdot 10^{-3}$	Figure 4.12c
S2.1	102.3 s	$3.1 \cdot 10^{-3}$	Figure 4.12d
S2.2	100.3 s	$2.8 \cdot 10^{-3}$	Figure 4.12e
S2.3	97.3 s	$2.5 \cdot 10^{-3}$	Figure 4.12f
S3.1	102.2 s	$3.4 \cdot 10^{-3}$	Figure 4.12g
S3.2	100.3 s	$2.9 \cdot 10^{-3}$	Figure 4.12h
S3.3	98.5 s	$2.7 \cdot 10^{-3}$	Figure 4.12i

Figure 4.11 displays the Pareto front of all three presented analyses, differentiated by color. In this case, unlike the results shown earlier, it is evident that the trend of the Pareto front is much more as expected, that is, hyperbolic. This is because, for each analysis, there is a design that maximizes one of the two aspects and, conversely, minimizes the other aspect, as well as a design that has intermediate values of the two objective functions.

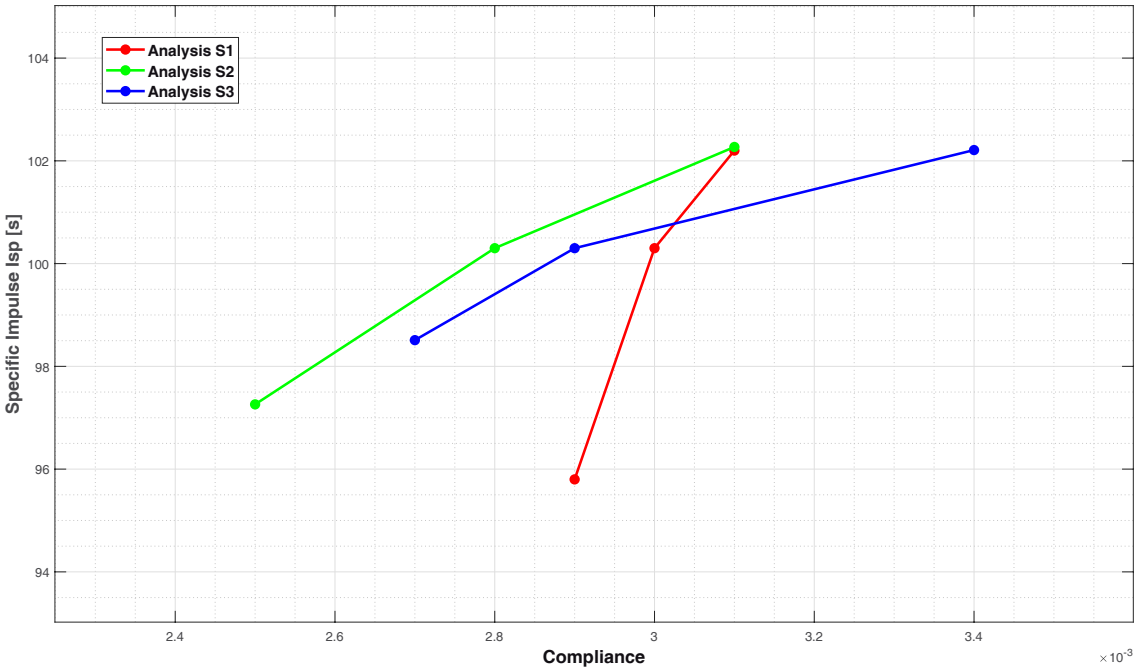

Figure 4.11: Pareto front of the double symmetry domain MDO

Figure 4.12 shows the designs obtained from the three presented analyses. It can be noted that there are four feasible designs out of the nine reported (i.e., S1.1, S2.1, S3.1, S3.3). As previously highlighted in Section 4.4.1, this is attributed to the lack of geometric, and hence physical, connection between some fuel elements and the main grain structure. With disconnected fuel elements, the fuel grain cannot be realized as a single piece and thus becomes unusable.

The first three designs among these have the highest specific impulse values, and design S2.1 specifically has the highest I_{sp} value, at 102.3 s, and a compliance value equal to that of design S1.1, i.e., $3.1 \cdot 10^{-}3$. Therefore, this design has a slightly lower specific impulse value compared to the full initial design, with a difference of approximately 1%, and represents the most promising geometry obtained.

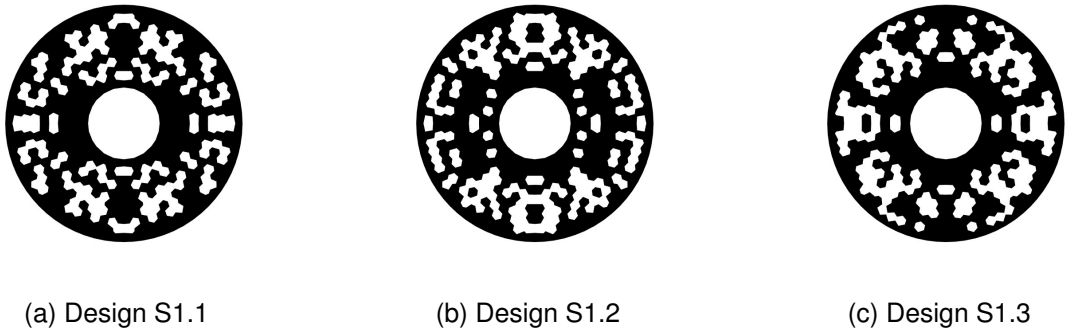

(a) Design S1.1 (b) Design S1.2 (c) Design S1.3

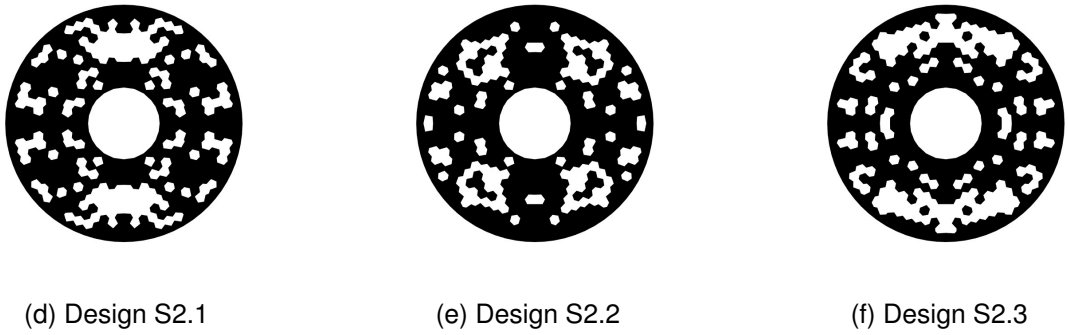

(d) Design S2.1 (e) Design S2.2 (f) Design S2.3

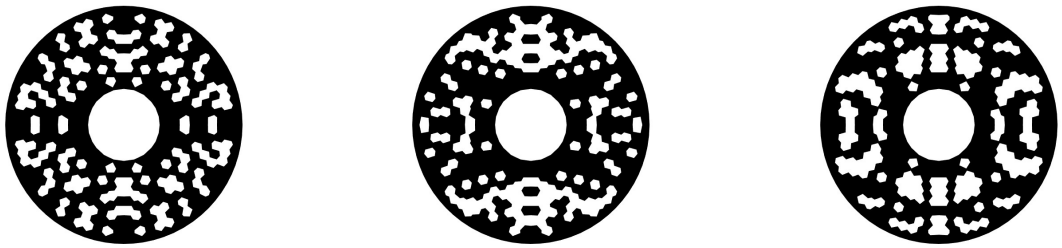

(g) Design S3.1 (h) Design S3.2 (i) Design S3.3

Figure 4.12: Optimized designs of the double symmetry domain

4.5 Multidisciplinary Design Optimization Green Fuel Comparison

In order to assess combinations of propellants with a lower environmental impact, the same methodology as described so far has been pursued to make comparisons with the results reported thus far.

Firstly, some clarification is needed regarding sustainable fuels for hybrid rockets. As previously mentioned, this type of propulsion can lead to improvements in terms of environmental impact. To enhance the sustainability of plastic-based fuels, three main approaches are identified. The first involves the use of recycled plastic, thereby reducing the environmental impact in the production cycle. The second and third focus on bio-derived fuels and synthetic fuels produced from renewable sources, respectively. These latter two approaches are sources of innovative research but are not yet fully developed [78].

For this reason, in this case, the choice was made to evaluate more sustainable fuels from the perspective of recycling. From this point of view, the ABS considered so far has a generic recycling code of 7, which applies to various types of plastics with more complex chemical compositions, leading to a more intricate recycling process [79].

Considering the state of the art and the various available research, it is observed that Polyethylene (PE) presents itself as a possible alternative. This material has a less complex chemical structure, and its recycling is facilitated by its more abundant use. It comes in different versions, including the basic one, depending on its density, namely High-Density Polyethylene (HDPE) with recycling code 2, and Low-Density Polyethylene (LDPE) with recycling code 4.

Thanks to research on PE as a potential fuel in hybrid propulsion [78, 80, 81] and the physical and chemical characterization of this material [82, 83], it has been possible to obtain and use the experimental data necessary to perform the same studies as reported earlier, for the case of ABS.

Therefore, the same model, with identical dimensions and the same oxidizer mass flow rate, was considered to facilitate a comparison between the two different fuels. The propellants considered are PE and, as before, GOx, with all their respective parameters listed in Table 4.5. It should be noted that despite the higher expected performance of HDPE, PE was chosen due to the greater availability of data for the latter. Furthermore, the PE considered, taken from the work of Kim et al. [81], already has densities intermediate between HDPE and Low-Density Polyethylene (LDPE), so it was chosen to use its more generic version.

Table 4.5: Model parameters with PE as fuel [81, 82]

Fuel	PE (Polyethylene)	
Oxidizer	O2 Gaseous	
Geometry	**Material**	**Propulsion**
External Radius / Diameter	Young Modulus	Oxidizer Mass Flow
$R = 2.5$ cm / $D = 5$ cm	$E = 2.0$ GPa	$\dot{m}_{ox} = 5$ g/s
Internal Radius / Diameter	Poisson's ratio	Regression coefficient
$r = 0.75$ cm / $d = 1.5$ cm	$\nu = 0.40$	$a = 0.026$
Length	Density	Regression coefficient
$L = 10$ cm	$\rho = 950$ kg/m^3	$n = 0.58$

Considering the recent results obtained in the preceding section, a similar study is conducted. Specifically, the double-symmetry configuration is reintroduced, and various optimizations are performed with different genetic parameters, ranging from 1000 to 2000 populations and 10 to 50 generations. In this case, the number of generations was further reduced because it was observed that even with a low number of generations, solutions were already converging.

Table 4.6 presents the outcomes of the primary analyses employing PE as the fuel. Three analyses are outlined, each encompassing four to five distinct designs, resulting in a total of 13 designs. These designs are denoted beginning with PE1.1, where "PE" signifies that these analyses employ PE as the fuel. The two numbers separated by a period denote the analysis number and the design number within that analysis, as before.

Table 4.6: Multidisciplinary optimization results of the double symmetry domain with PE as fuel

Designs	$\mathbf{I_{sp}}$	$\mathbf{Compliance}$	**Figure**
PE1.1	103.8 s	$6.6 \cdot 10^{-3}$	Figure 4.14a
PE1.2	103.1 s	$3.9 \cdot 10^{-3}$	Figure 4.14b
PE1.3	101.2 s	$3.8 \cdot 10^{-3}$	Figure 4.14c
PE1.4	98.0 s	$3.4 \cdot 10^{-3}$	Figure 4.14d
PE2.1	103.8 s	$6.1 \cdot 10^{-3}$	Figure 4.15a
PE2.2	103.1 s	$4.2 \cdot 10^{-3}$	Figure 4.15b
PE2.3	102.1 s	$3.8 \cdot 10^{-3}$	Figure 4.15c
PE2.4	99.1 s	$3.7 \cdot 10^{-3}$	Figure 4.15d
PE2.5	98.0 s	$3.7 \cdot 10^{-3}$	Figure 4.15e
PE3.1	103.8 s	$6.3 \cdot 10^{-3}$	Figure 4.16a
PE3.2	103.1 s	$3.9 \cdot 10^{-3}$	Figure 4.16b
PE3.3	101.2 s	$3.8 \cdot 10^{-3}$	Figure 4.16c
PE3.4	91.2 s	$3.7 \cdot 10^{-3}$	Figure 4.16d

Figure 4.13 displays the Pareto front of all presented analyses, differentiated by color. In this case, even more than the previous results, it is evident that the trend of the Pareto front is as expected for this type of analysis, as explained in the section before.

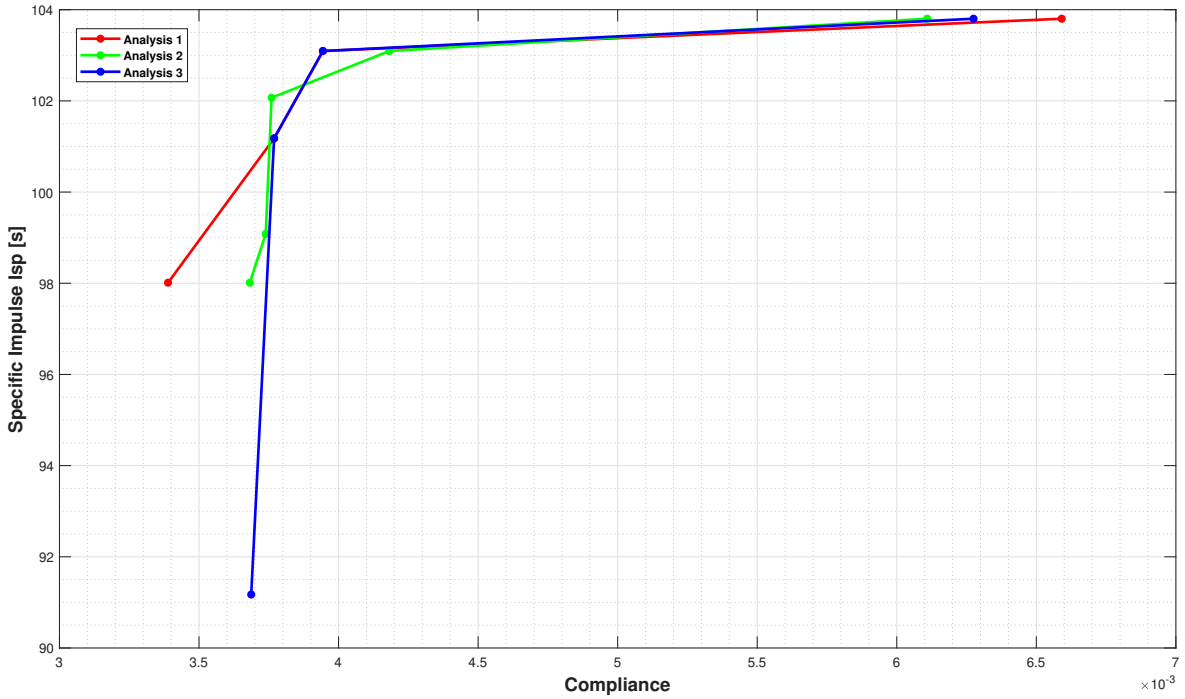

Figure 4.13: Pareto front of the double symmetry domain MDOs with PE as fuel

Observing these reported results allows for an initial comparison between the models with ABS and PE. Firstly, it can be noted that the compliance values are generally higher in the latter case analyzed. This was expected due to the inferior physical properties of PE compared to ABS. Regarding performance, it can be observed that the specific impulse values are very similar between the two models with different fuels, with differences of less than 1% in favor of PE. However, concerning the propulsion aspect, the most unexpected result concerns the performance improvement achieved through optimization. The initial solid configuration in PE yielded a specific impulse value of 94.8 s, while considering the best optimized designs resulted in improvements of around 10%. This significantly deviates from what was reported for the ABS model, which showed improvements on the order of 1%.

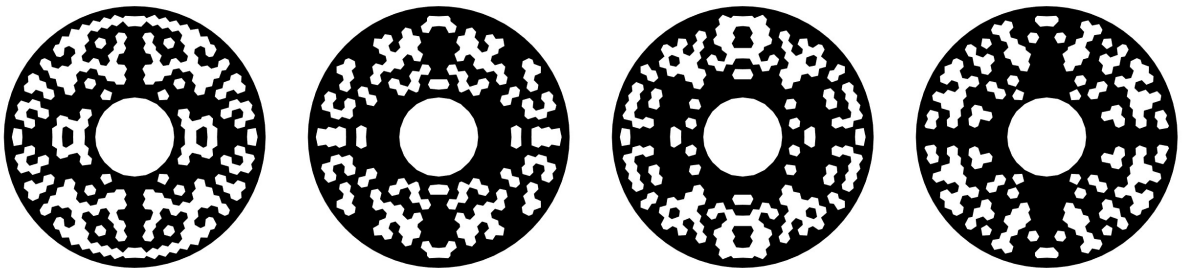

(a) Design PE1.1 (b) Design PE1.2 (c) Design PE1.3 (d) Design PE1.4

Figure 4.14: Optimized designs of Analysis 1 with PE as fuel

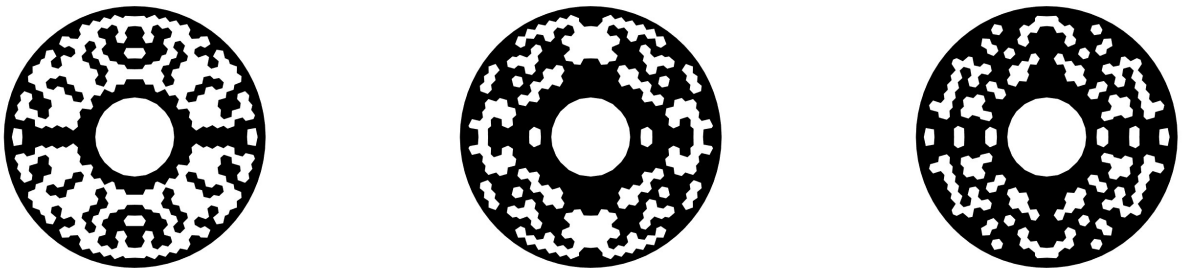

(a) Design PE2.1 (b) Design PE2.2 (c) Design PE2.3

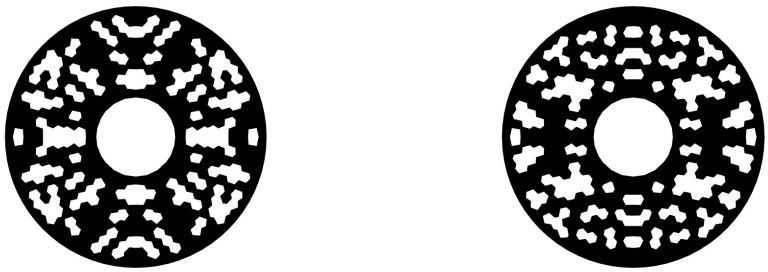

(d) Design PE2.4 (e) Design PE2.5

Figure 4.15: Optimized designs of Analysis 2 with PE as fuel

Figures 4.14, 4.15 and 4.16 displays the designs obtained from the three presented analyses. It can be observed that out of the thirteen designs reported, eight are feasible (i.e., PE1.2, PE1.4, PE2.2, PE2.3, PE2.4, PE2.5, PE3.1, and PE3.3). As with the previous results, this is due to the lack of connection between some fuel elements and the main grain structure.

Design PE3.1 exhibits the best propulsion performance with the highest value of I_{sp} at 103.8 s, while maintaining a compliance value of $6.3 \cdot 10^{-}3$. The next best designs in terms of propulsion performance are PE1.2, PE2.2, and PE3.2, with a slight decrease in specific impulse, approximately 1%, but also a more significant reduction in compliance, around 33% to 38%. As previously mentioned, these designs have shown an improvement in performance of about 10% compared to the initial full domain.

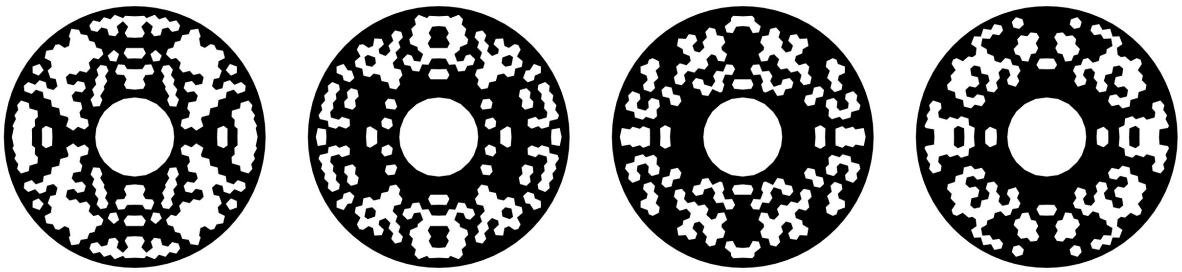

(a) Design PE3.1 (b) Design PE3.2 (c) Design PE3.3 (d) Design PE3.4

Figure 4.16: Optimized designs of Analysis 3 with PE as fuel

Finally, to assess the environmental impact of the different proposed solutions, a Life Cycle Assessment (LCA) is carried out the emissions resulting from the combustion process, namely using the Global Warming Potential (GWP) metric.

This is one of the most widely used environmental metrics and allows for the measurement of the environmental impact of a specific greenhouse gas. Specifically, it quantifies its contribution to the greenhouse effect in relation to the effect of Carbon Dioxide (CO_2), which has a reference potential of 1. Each GWP value is calculated on a timescale ranging from 20 to 500 years, with the commonly used 100-year timescale [84]. In the present work, a timescale of 100-year was also chosen.

This analysis was conducted on the best-optimized designs obtained, namely design S2.1 for ABS and design PE3.1 for PE. Using the CEA Software, it was possible to obtain data related to the mass fractions of the products resulting from the complete combustion of the two grains.

Table 4.7 presents this data along with the fuel mass value for each iteration of the combustion process. This is because the output data are provided for each iteration of the combustion process, denoted by a superscript in the first row of the table. Therefore, in this case, there are two iterations for design S2.1 in ABS and only one for PE3.1 in PE.

Table 4.7: Mass fractions of the combustion products from the best optimized designs

Products	**ABS Design S2.1$_1$**	**ABS Design S2.1$_2$**	**PE Design PE3.1**
Fuel mass [g]	116.4	25.9	103.5
CH_4	0.00003	0	0.00006
CO	0.58353	0.67549	0.87521
CO_2	0.00001	0.12453	0.00005
C_2H_2	0.00001	0	0
H	0.00001	0.00435	0
HCN	0.00041	0	0
HNC	0.00001	0	0
H_2	0.05699	0.01623	0.07184
H_2O	0.00001	0.11352	0.00005
N_2	0.07004	0.04176	0
C	0.28895	0	0.05279
NO	0	0.00084	0
O	0	0.00461	0
OH	0	0.01575	0
O_2	0	0.00292	0

Table 4.8: Global Warming Potential (GWP) emissions computation of the best optimized designs

	ABS Design S2.1	**PE Design PE3.1**
Total fuel mass [g]	142.3	103.5
CH_4 (GWP=34) **g CO_2eq**	0.11873	0.21114
CO_2 (GWP=1) **g CO_2eq**	3.22649	0.00518
C_2H_2 (GWP=0.0468) **g CO_2eq**	0.00005	0
Total g CO_2eq	3.34527	0.21632

Table 4.8 reports the calculation of emissions using GWP. To calculate emissions, expressed as the value of equivalent Carbon Dioxide (CO_2), it is necessary to multiply the mass fractions of the products by the fuel mass, both of which are reported in Table 4.7, and finally by the respective GWP value for each different molecule, as shown in Table 4.8. The calculation is carried out for each individual iteration and then summed in the case of multiple iterations. Table 4.8 exclusively presents the substances that contribute the most to the GWP calculation, along with their respective GWP values.

The GWP estimation was obtained using the SimaPro ® software [85], employing the Recipe database and a mid-point approach. SimaPro is a commercial software designed for conducting LCA [86]. The utilized data were derived from the research of Figueiras et al. [87], from which only the values with the highest impact, as per their developed model, were employed.

From the results provided, it can be observed that the environmental impact of the PE design, in terms of Carbon Dioxide Equivalent (CO_2eq), is 93.5% lower. Furthermore, the mass of design PE3.1 is also lower, with a weight saving of 27.3%. Therefore, based on both environmental and propulsion-related data, design PE3.1 outperforms design S2.1, highlighting the lower environmental impact of PE compared to ABS.

Chapter 5

Conclusions and Recommendations

This chapter serves as the conclusion to this work, summarizing the key findings and insights gained from the research, and providing recommendations for potential future implementations.

5.1 Conclusions

Considering the methodologies employed, as discussed in Chapter 3, and the results presented in Chapter 4, it is now feasible to formulate conclusions regarding the various analyses conducted and, more broadly, the entire developed work.

In this context, the main conclusions related to the entire work are initially outlined, analyzing the achievements and key limitations. Subsequently, more explanatory and detailed concluding remarks will be drawn for all the various analyses conducted.

The identified limitations at the end of this work include the absence of a clear correlation between specific impulse and grain shape, sought in the maximization of performance, and the lack of a specific target geometry to pursue in multidisciplinary design optimizations.

The accomplishments of this work undoubtedly involve the validation of the developed regression analysis code and the results obtained from multidisciplinary optimizations with double symmetry considering both different fuels. Optimizing the ABS model led to obtaining feasible geometries with performances similar to the initial configuration of the full model. On the other hand, optimizing the PE model resulted in better outcomes. Multiple feasible designs with enhanced performance compared to the initial PE configuration were obtained, showing a 10% improvement. Furthermore, comparing emissions from the two best-optimized designs in ABS and PE, respectively, with similar performances demonstrated the lower environmental impact of PE, with a 93.5% reduction in emissions compared to the ABS model. This outcome highlights the potential for sustainability improvements through the use of materials with a lower environmental impact.

Upon examining in detail all the different analyses conducted, it is possible to outline the following specific conclusions.

- **Regression Analysis**

  The regression analysis performed using the developed `PolyReg` code effectively simulated the experimental test reported in the work of Yu et al. [59], also aligning with the expected theoretical trends.

- **Structural Topology Optimization**

  The results obtained from structural topology optimization have consistently revealed wagon wheel-type designs, as anticipated. This outcome is attributed to the improved stress distribution within these designs.

- **Propulsive Topology Optimization**

  Conversely, the results of the propulsive topology optimization have led to distinct conclusions.

  The designs exhibiting the best performance were those with either completely hollow or completely solid simple geometries. Subsequent top-performing designs displayed undefined and rather random patterns, which are not feasible for practical implementation. These outcomes underscore the inability to establish a specific correlation between grain geometry and specific impulse.

- **Multidisciplinary Design Optimization**

  The results obtained from the multidisciplinary design optimizations using genetic algorithms have provided valuable insights.

  One noteworthy observation is the considerable influence of the initial population configuration on the outcomes of the optimizations conducted, as expected given the large number of design variables. By observing Table 4.3, it is evident that there are significant variations in the optimized values of compliance and I_{sp} among the different analyses. This suggests that increasing the number of populations may be necessary to obtain more robust and reliable results. However, it is important to consider the trade-off between the quality of results and the computational time, as the latter tends to exponentially increase with larger population sizes.

- **Multidisciplinary Design Optimization with Double Symmetry**

  The results obtained from the MDO with double symmetry have shown an improvement compared to the previous ones without geometric imposition.

  First and foremost, the significant reduction in the number of variables has led to a substantial decrease in the influence of the initial population on the obtained designs. This is demonstrated by the fact that, unlike the previous MDO analyses, multiple analyses with different geometric parameters, but values consistent with the previous optimizations, sometimes led to the same solutions or designs that were still similar to each other.

Furthermore, the organization of the results forming the Pareto fronts of the various analyses has proven to be in line with expectations, improving compared to the previous optimizations. All of this translates into greater effectiveness in the optimization carried out with genetic algorithms and, consequently, better results.

Feasible geometries have been obtained, with performance values very similar (1% difference) to those obtained from the full initial geometry, as presented in Table 4.4. In this case as well, a well-defined geometric pattern has not been achieved. However, these results have demonstrated greater feasibility and geometries that are not primarily random.

- **Multidisciplinary Design Optimization Green Fuel Comparison**

  The results obtained from the MDO considering double symmetry and PE as fuel have shown comparable performance to those obtained previously with ABS.

  The Pareto front obtained from the various analyses exhibited a trend that aligns perfectly with expectations, even improving the overall result compared to the previous optimization.

  The geometries obtained are mostly feasible and have demonstrated performance on par with those of the ABS model, with small variations of around 1% from the maximum value. These results endorse the use of PE as a potential substitute for ABS to reduce environmental impact through improved recycling. Furthermore, these optimizations, compared to the previous case, have yielded a significant performance improvement of up to 10% compared to the initial configuration.

  The results obtained from the GWP-based emissions calculation of the best designs in PE and ABS have led to significant considerations.

  These results, in terms of performance (specific impulse) and environmental impact (CO_2eq emissions), favor design PE3.1 in PE over all the other designs presented. Moreover, it has become evident that PE has a lower environmental impact compared to ABS.

In conclusion, regarding the performance maximization, no well-defined geometric pattern emerged, contrasting with the compliance minimization which involved topological optimization. This indicates a weak correlation between I_{sp} and the geometric shape of the grain, warranting further investigation into the underlying factors that contribute to I_{sp}.

Overall, these findings highlight the complexity and multifaceted nature of the multidisciplinary optimization process, emphasizing the need for thorough analysis and exploration to achieve optimal performance in hybrid rocket fuel design.

Finally, the use of PE has highlighted the potential for improvement in terms of sustainability and environmental impact through the use of materials that promote the recycling process and reduce emissions.

5.2 Recommendations for Future Research

The findings presented in this master thesis could be considered as an initial phase of a broader study that requires further exploration. Additional analyses should be conducted to obtain more robust results, and the implementation of further investigations or research avenues is also being considered to expand the horizons of this research.

These possibilities include:

- **Multidisciplinary Design Optimization Analyses**

  Leveraging advanced MDO strategies can further enhance the efficiency and effectiveness of the optimization process. This will lead to the discovery of optimal designs that maximize performance while considering multiple disciplines simultaneously.

- **Experimental Validation**

  Future studies should prioritize the execution of comprehensive experimental campaigns to validate the performance of hybrid rocket engines under real-world conditions, by conducting side-by-side comparisons of: different fuel combinations, propellant formulations, and combustion strategies.

- **Exploration of Novel Fuel Combinations**

  Analyzing and evaluating different fuel combinations is crucial to expanding the performance capabilities of hybrid rocket engines. Future research should focus on investigating alternative propellants, exploring high-energy additives, and considering sustainable and eco-friendly fuel options. By studying the impact of these fuel combinations on performance and optimization, it is possible to unlock new possibilities and advance the work towards greener and more efficient propulsion systems.

- **Emissions calculation and comparison**

  Emissions calculations are essential for exploring different geometries and propellant combinations that can lead to greater sustainability. By studying and comparing these alternatives with more traditional and widely used propulsion solutions, it is possible to quantify and analyze the potential improvements achieved and identify areas for further development. All of these efforts are directed toward achieving solutions with reduced environmental impact, encompassing not only material-related production processes but also chemical pollution. In this regard, it is imperative to expand the analyses to consider various manufacturing and recycling processes that contribute to the global pollution associated with each material. These endeavors are in line with a market where sustainability is gaining increasing importance and interest.

- **Advancement towards 3D Geometries**

  Transitioning from 2D to 3D geometries will provide greater freedom and flexibility for optimization, enabling the exploration of more complex designs. Future research should focus on developing advanced computational models capable of capturing the intricate flow and combustion phenomena in three-dimensional space.

- **Integration of Computational Fluid Dynamics Analyses**

  Implementing CFD analyses into the design and optimization process will significantly contribute to improved thermal and propulsion results. By studying the evolution of the flow field, heat transfer, and combustion processes, CFD simulations can provide valuable insights into the performance characteristics of hybrid rocket engines.

Bibliography

[1] L. Casalino, F. Masseni, and D. Pastrone. Hybrid rocket engine design optimization at politecnico di torino: A review. *Aerospace*, 8(8), 2021. doi:10.3390/aerospace8080226.

[2] M. Mehrpouya, A. Vosooghnia, A. Dehghanghadikolaei, and B. Fotovvati. Chapter 2 - the benefits of additive manufacturing for sustainable design and production. In K. Gupta and K. Salonitis, editors, *Sustainable Manufacturing*, Handbooks in Advanced Manufacturing, pages 29–59. Elsevier, 2021. doi:10.1016/B978-0-12-818115-7.00009-2.

[3] D. Altman. Hybrid rocket development history. *27th Joint Propulsion Conference*, 1991. doi:10.2514/6.1991-2515.

[4] P. M. Zolla, M. T. Migliorino, D. Bianchi, F. Nasuti, R. C. Pellegrini, and E. Cavallini. A computational tool for the design of hybrid rockets. *Aerotecnica Missili Spazio*, 100(253–262), 2021. doi:10.1007/s42496-021-00085-3.

[5] A. Okninski, W. Kopacz, D. Kaniewski, and K. Sobczak. Hybrid rocket propulsion technology for space transportation revisited - propellant solutions and challenges. *FirePhysChem*, 1(4):260–271, 2021. doi:10.1016/j.fpc.2021.11.015.

[6] Aerospace technology. Virgin galactic spaceship. URL `https://www.aerospace-technology.com/projects/virgin-spaceship/`. [Accessed 7 September 2023].

[7] C. Niederstrasser. Small launchers in a pandemic world - 2021 edition of the annual industry survey. *35th Annual AIAA/USU Conference on Small Satellites*, 2021. URL `https://digitalcommons.usu.edu/smallsat/2021/all2021/162/`.

[8] K. K. Kuo and M. J. Chiaverini. *Fundamentals of Hybrid Rocket Combustion and Propulsion*. American Institute of Aeronautics and Astronautics, 2007. doi:10.2514/4.866876.

[9] M. P. King. Analysis for hybrid rocket fuel regression using stereolithographic geometry. Master's thesis, Air Force Institute of Technology, 2020. URL `https://scholar.afit.edu/cgi/viewcontent.cgi?article=5544&context=etd`.

[10] W. Henry. Hybrid rocket education at the u.s. air force academy. *28th Joint Propulsion Conference and Exhibit*, 1992. doi:10.2514/6.1992-3300.

[11] T. Marquardt and J. Majdalani. Review of classical diffusion-limited regression rate models in hybrid rockets. *Aerospace*, 6(6), 2019. doi:10.3390/aerospace6060075.

[12] C. Nguyen and J. C. Thomas. Performance of additively manufactured fuels for hybrid rockets. *Aerospace*, 10(6), 2023. doi:10.3390/aerospace10060500.

[13] R. A. Braeunig. Rocket and space technology, 2012. URL `http://www.braeunig.us/space/propuls.htm#thrust`. [Accessed 7 September 2023].

[14] C. Glaser, J. Hijlkema, and J. Anthoine. Evaluation of regression rate enhancing concepts and techniques for hybrid rocket engines. *Aerotecnica Missili & Spazio*, 101(3):267–292, 2022. doi:10.1007/s42496-022-00119-4.

[15] M. Calabro. Overview on hybrid propulsion. 2:353–374, 2011. doi:10.1051/eucass/201102353.

[16] NASA. Nasa cea run. URL `https://cearun.grc.nasa.gov/`. [Accessed 7 September 2023].

[17] D. Lempert, E. Dorofeenko, S. Soglasnova, and A. Matveev. Existence of limiting values of the specific impulse of metal-free composite solid propellants at a preset highest allowable combustion temperature. *Russian Journal of Physical Chemistry B*, 10:628–631, 2016. doi:10.1134/S1990793116040072.

[18] L. DeLuca, L. Galfetti, F. Maggi, G. Colombo, A. Reina, S. Dossi, D. Consonni, and M. Brambilla. Innovative metallized formulations for solid or hybrid rocket propulsion. 20(4):465–474, 2011. doi:10.3969/j.issn.1006-9941.2012.04.018.

[19] A. Karabeyoglu. Hybrid rocket propulsion for future space launch. *Aero/Astro 50th Year Anniversary*, 2008. URL `https://repository.cs.ru.is/svn/mjolnir/research/Karabeyoglu.pdf`.

[20] S. A. Whitmore, S. D. Walker, D. P. Merkley, and M. Sobbi. High regression rate hybrid rocket fuel grains with helical port structures. *Journal of Propulsion and Power*, 31(6), 2015. doi:10.2514/1.B35615.

[21] D. J. Vonderwell, I. F. Murray, and S. D. Heister. Optimization of hybrid-rocket-booster fuel-grain design. *Journal of Spacecraft and Rockets*, 32(6):964–969, 1995. doi:10.2514/3.26716.

[22] D. Armold, J. E. Boyer, K. Kuo, J. K. Fuller, J. Desain, and T. J. Curtiss. *Test of Hybrid Rocket Fuel Grains with Swirl Patterns Fabricated Using Rapid Prototyping Technology*. 2013. doi:10.2514/6.2013-4141.

[23] P. Hill. *Mechanics and thermodynamics of propulsion*. Addison-Wesley, 1992. ISBN 9780201146592.

[24] K. Cummins. The rise of additive manufacturing. *The Engineer*, 2010. URL `https://www.theengineer.co.uk/content/in-depth/the-rise-of-additive-manufacturing/`. [Accessed 7 September 2023].

[25] C. Hull. Apparatus for production of three-dmensional objects by stereolthography, 1986. URL https://patents.google.com/patent/US4575330.

[26] All3DP. What is an stl file? – the stl format simply explained. URL https://all3dp.com/1/stl-file-format-3d-printing/. [Accessed 7 September 2023].

[27] 3DSystem. URL https://www.loc.gov/preservation/digital/formats/fdd/fdd_explanation.shtml#identification. [Accessed 7 September 2023].

[28] I. Gibson, D. Rosen, and B. Stucker. *Additive Manufacturing Technologies. 3D Printing, Rapid Prototyping, and Direct Digital Manufacturing*. Springer, 2015. doi:10.1007/978-1-4939-2113-3.

[29] custompart.net, . URL https://www.custompartnet.com/wu/stereolithography. [Accessed 7 September 2023].

[30] custompart.net, . URL https://www.custompartnet.com/wu/fused-deposition-modeling. [Accessed 7 September 2023].

[31] custompart.net, . URL https://www.custompartnet.com/wu/selective-laser-sintering. [Accessed 7 September 2023].

[32] A. Petrarolo, M. Kobald, and S. Schlechtriem. Optical analysis of the liquid layer combustion of paraffin-based hybrid rocket fuels. *Acta Astronautica*, 158, 2019. doi:10.1016/j.actaastro.2018.05.059.

[33] M. Boiocchi, P. Milova, L. Galfetti, L. Landro, and A. Golovko. A wide characterization of paraffin-based fuels mixed with styrene-based thermoplastic polymers for hybrid propulsion. 2016. doi:10.1051/eucass/201608241.

[34] C. Oztan. Utilization of additive manufacturing in hybrid rocket technology: A review. *Acta Atronautica*, 180, 2021. doi:10.1016/j.actaastro.2020.11.024.

[35] S. Whitmore, Z. Peterson, and S. Eilers. Analytical and experimental comparisons of htpb and abs as hybrid rocket fuels. In *47th AIAA/ASME/SAE/ASEE Joint Propulsion Conference*, San Diego, CA, USA, July-August 2011. doi:10.2514/6.2011-5909.

[36] S. A. Whitmore and S. D. Walker. Engineering model for hybrid fuel regression rate amplification using helical ports. *Journal of Propulsion and Power*, 33(2), 2017. doi:10.2514/1.B36208.

[37] S. A. Whitmore, Z. W. Peterson, and S. D. Eilers. Comparing hydroxyl terminated polybutadiene and acrylonitrile butadiene styrene as hybrid rocket fuels. *Journal of Propulsion and Power*, 29(3), 2013. doi:10.2514/1.B34382.

[38] M. McFarland and E. Antunes. Small-scale static fire tests of 3d printing hybrid rocket fuel grains produced from different materials. *Aerospace*, 6(7), 2019. doi:10.3390/aerospace6070081.

[39] L. Pabarcius. Development and preliminary testing of paraffin hybrid rocket fuel grains with helical port structures. *AIAA Propulsion and Energy 2019 Forum*, 2019. doi:10.2514/6.2019-4187.

[40] Z. Wang, X. Lin, F. Li, and X. Yu. Combustion performance of a novel hybrid rocket fuel grain with a nested helical structure. *Aerospace Science and Technology*, 97, 2020. doi:10.1016/j.ast.2019.105613.

[41] J. M. McCulley. Design and testing of digitally manufactured paraffin. Master's thesis, Utah State University, 2012. URL `https://digitalcommons.usu.edu/cgi/viewcontent.cgi?article=2451&context=etd`.

[42] B. R. McKnight, J. E. Boyer, P. K. Nardozzo, and A. Cortopassi. Design and testing of an additively manufactured advanced hybrid rocket motor propulsion unit for cubesats (puc). *51st AIAA/SAE/ASEE Joint Propulsion Conference*, 2015. doi:10.2514/6.2015-4036.

[43] M. P. Bendsøe. Optimal shape design as a material distribution problem. *Structural Optimization*, 1:193–202, 01 1989. doi:10.1007/BF01650949.

[44] O. Sigmund and K. Maute. Topology optimization approaches. *Structural and Multidisciplinary Optimization*, 48:1031–1055, 2013. doi:10.1007/s00158-013-0978-6.

[45] M. Bendsoe and O. Sigmund. Topology optimization: Theory, methods, and applications. 2003. doi:10.1007/978-3-662-05086-6.

[46] E. Tyflopoulos, D. Flem, M. Steinert, and A. Olsen. State of the art of generative design and topology optimization and potential research needs. 2018. ISBN 978-91-7685-185-2.

[47] Y. M. Xie and G. P. Steven. *Evolutionary Structural Optimization*. Springer London, 1997. doi:10.1007/978-1-4471-0985-3.

[48] L. Van Miegroet and P. Duysinx. Stress concentration minimization of 2d filets using x-fem and level set description. *Structural and Multidisciplinary Optimization*, 33:425–438, 2007. doi:10.1007/s00158-006-0091-1.

[49] G. I. N. Rozvany. *Structural design via optimality criteria: the Prager approach to structural optimization*. Springer, 1990. doi:10.1007/978-94-009-1161-1.

[50] C. Fleury. *CONLIN: an efficient dual optimizer based on convex approximation concepts*. Springer, 1989. doi:10.1007/BF01637664.

[51] K. Svanberg. The method of moving asymptotes—a new method for structural optimization. *International Journal for Numerical Methods in Engineering*, 24(2):359–373, 1987. doi:10.1002/nme.1620240207.

[52] N. Jorge and S. Wright. *Numerical Optimization*. Springer, 2006. doi:10.1007/978-0-387-40065-5.

[53] Y. Saadlaoui, J.-L. Milan, J.-M. Rossi, and P. Chabrand. Topology optimization and additive manufacturing: Comparison of conception methods using industrial codes. *Journal of Manufacturing Systems*, 43:178–186, 2017. doi:10.1016/j.jmsy.2017.03.006.

[54] S. Li, S. Yuan, J. Zhu, W. Zhang, H. Zhang, and J. Li. Multidisciplinary topology optimization incorporating process-structure-property-performance relationship of additive manufacturing. *Structural and Multidisciplinary Optimization*, 63:2141–2157, 2021. doi:10.1007/s00158-021-02856-9.

[55] M. Mitchell. *An introduction to genetic algorithms*. The MIT Press, 1996. ISBN 9780262631853.

[56] X.-S. Yang. Genetic algorithms. In *Nature-Inspired Optimization Algorithms*, pages 91–100. Academic Press, second edition, 2021. doi:10.1016/B978-0-12-821986-7.00013-5.

[57] S. Mirjalili. *Genetic Algorithm*. Springer International Publishing, 2019. doi:10.1007/978-3-319-93025-1_4.

[58] M. A. Albadr, S. Tiun, M. Ayob, and F. AL-Dhief. Genetic algorithm based on natural selection theory for optimization problems. *Symmetry*, 12(11), 2020. doi:10.3390/sym12111758.

[59] X. Yu, H. Yu, W. Zhang, L. T. DeLuca, and R. Shen. Effect of penetrative combustion on regression rate of 3d printed hybrid rocket fuel. *Aerospace*, 9(11), 2022. doi:10.3390/aerospace9110696.

[60] A. Mahjub, Q. Azam, M. Z. Abdullah, and N. M. Mazlan. Cad-based 3d grain burnback analysis for solid rocket motors. In *Proceedings of International Conference of Aerospace and Mechanical Engineering 2019*. Springer Singapore, 2020. doi:10.1007/978-981-15-4756-0_28.

[61] omnexus.specialchem.com. URL `https://omnexus.specialchem.com/selection-guide/acrylonitrile-butadiene-styrene-abs-plastic`. [Accessed 7 September 2023].

[62] C. Talischi, G. Paulino, A. Pereira, and I. Menezes. Polymesher: a general-purpose mesh generator for polygonal elements written in matlab. *Structural and Multidisciplinary Optimization*, 45:309–328, 2012. doi:10.1007/s00158-011-0706-z.

[63] C. Talischi, G. Paulino, A. Pereira, and I. Menezes. Polytop: a matlab implementation of a general topology optimization framework using unstructured polygonal finite element meshes. *Structural and Multidisciplinary Optimization*, 45, 2012. doi:10.1007/s00158-011-0696-x.

[64] G. Paulino. URL `http://paulino.princeton.edu/index.html`. [Accessed 7 September 2023].

[65] C. Talischi, G. Paulino, A. Pereira, and I. Menezes. Polymesher: a general-purpose mesh generator for polygonal elements written in matlab. In *11th U.S. National Congress on Computational Mechanics*, Minnesota, USA, July 2011. URL `http://paulino.princeton.edu/conferences/presentations/11periera_polymesher.pdf`.

[66] F. Aurenhammer. Voronoi diagrams—a survey of a fundamental geometric data structure. *ACM Comput. Surv.*, 23(3):345–405, 1991. doi:10.1145/116873.116880.

[67] B. J. McBride and S. Gordon. Computer Program for Calculation of Complex Chemical Equilibrium Compositions and Applications. I. Analysis. Technical report, NASA Reference Publication 1311, 1994. URL `https://ntrs.nasa.gov/citations/19950013764`.

[68] B. J. McBride and S. Gordon. Computer Program for Calculation of Complex Chemical Equilibrium Compositions and Applications. II. Users Manual and Program Description. Technical report, NASA Reference Publication 1311, 1996. URL https://ntrs.nasa.gov/citations/19960044559.

[69] G. P. Sutton and O. Biblarz. *Rocket propulsion elements*. John Wiley Sons Inc., 2017. ISBN 978-1118753651.

[70] S. Gordon and B. J. McBride. Computer program for calculation of complex chemical equilibrium compositions, rocket performance, incident and reflected shocks, and chapman-jouguet detonations. Technical report, NASA Special Publication 273, 1976. URL https://ntrs.nasa.gov/citations/19780009781.

[71] S. Gordon and B. J. McBride. Finite area combustor theoretical rocket performance. Technical report, NASA Technical Memorandum 100785, 1988. URL https://ntrs.nasa.gov/citations/19880011868.

[72] K. Deb, A. Pratap, S. Agarwal, and T. Meyarivan. A fast and elitist multiobjective genetic algorithm: Nsga-ii. *IEEE Transactions on Evolutionary Computation*, 6(2), 2002. doi:10.1109/4235.996017.

[73] H.-G. Beyer and K. Deb. On self-adaptive features in real-parameter evolutionary algorithms. *Evolutionary Computation, IEEE Transactions on*, 5:250 – 270, 07 2001. doi:10.1109/4235.930314.

[74] R. Agrawal and K. Deb. Simulated binary crossover for continuous search space. *Complex Systems*, 9, 2000. URL https://www.researchgate.net/publication/2333106_Simulated_Binary_Crossover_for_Continuous_Search_Space. [Accessed 7 September 2023].

[75] M. M. Raghuwanshi and O. Kakde. Survey on multiobjective evolutionary and real coded genetic algorithms. *Complexity*, 11, 2004. URL https://api.semanticscholar.org/CorpusID:15073668.

[76] J. R. R. A. Martins and A. Ning. *Engineering Design Optimization*. Cambridge University Press, 2022. doi:10.1017/9781108980647.

[77] MathWorks, Inc. URL https://www.mathworks.com/help/gads/ga.html. [Accessed 7 September 2023].

[78] F. Barato. Review of alternative sustainable fuels for hybrid rocket propulsion. *Aerospace*, 10(7), 2023. doi:10.3390/aerospace10070643.

[79] J. Jiang, K. Shi, X. Zhang, K. Yu, H. Zhang, J. He, Y. Ju, and J. Liu. From plastic waste to wealth using chemical recycling: A review. *Journal of Environmental Chemical Engineering*, 10(1):106867, 2022. doi:10.1016/j.jece.2021.106867.

[80] Y. Pal and R. Vijayaraghavan. Physical and ballistic characterization of aluminum-loaded paraffin hybrid rocket fuels. *Energy Fuels*, 31, 08 2017. doi:10.1021/acs.energyfuels.7b01636.

[81] S. Kim, H. Moon, J. Kim, and J. Cho. Evaluation of paraffin–polyethylene blends as novel solid fuel for hybrid rockets. *Journal of Propulsion and Power*, 31:1–11, 07 2015. doi:10.2514/1.B35565.

[82] J. L. Jordan, R. L. Rowland, J. Greenhall, E. K. Moss, R. C. Huber, E. C. Willis, R. Hrubiak, C. Kenney-Benson, B. Bartram, and B. T. Sturtevant. Elastic properties of polyethylene from high pressure sound speed measurements. *Polymer*, 212:123164, 2021. doi:10.1016/j.polymer.2020.123164.

[83] P. L. Splitstone and W. H. Johnson. The enthalpies of combustion and formation of linear polyethylene. *Journal of research of the National Bureau of Standards. Section A, Physics and chemistry*, 78A 5:611–616, 1974. doi:10.6028/jres.078A.038.

[84] P. Makhnatch and R. Khodabandeh. The role of environmental metrics (gwp, tewi, lccp) in the selection of low gwp refrigerant. *Energy Procedia*, 61:2460–2463, 2014. doi:10.1016/j.egypro.2014.12.023.

[85] PRé Sustainability. URL `https://simapro.com/`. [Accessed 9 October 2023].

[86] M. Hauschild, R. Rosenbaum, and S. Olsen. *Life Cycle Assessment: Theory and Practice*. 09 2017. doi:10.1007/978-3-319-56475-3.

[87] I. Figueiras, G. Musso, H. Goubel, A. Costa, B. Ferreira, L. Azeitona, S. Barata, A. Souza, F. Afonso, and F. Lau. On the design of next-generation launch vehicles: A multidisciplinary framework for a reusable vehicle for multipurpose missions. In *13th EASN International Conference on Innovation in Aviation Space for Opening New Horizons*, Salerno, Italy, September 2023.